ISSN Print: 2518-4245
ISSN Online: 2518-4253
Vol. 63(2), June 2026

PROCEEDINGS
OF THE PAKISTAN ACADEMY OF SCIENCES:
A. Physical and Computational Sciences

PAKISTAN ACADEMY OF SCIENCES
ISLAMABAD, PAKISTAN

Proceedings of the Pakistan Academy of Sciences: Part A Physical and Computational Sciences

Proceedings of the Pakistan Academy of Sciences A. Physical and Computational Sciences is the official flagship, the peer-reviewed quarterly journal of the Pakistan Academy of Sciences. This open-access journal publishes original research articles and reviews on current advances in the field of Computer Science (all), Materials Science (all), Physics and Astronomy (all), Engineering Sciences (all), Chemistry, Statistics, Mathematics, Geography, Geology in English. Authors are not required to be Fellows or Members of the Pakistan Academy of Sciences or citizens of Pakistan. The journal is covered by Print and Online ISSN, indexed in Scopus, and distributed to scientific organizations, institutes and universities throughout the country, by subscription and on an exchange basis.

Annual Subscription: **Pakistan:** Institutions, Rupees 8000/-; Individuals, Rupees 4000/- (Delivery Charges: Rupees 300/-)
Other Countries: US$ 200.00 (includes air-lifted overseas delivery)

HEC Recognized; Scopus Indexed

Published by **Pakistan Academy of Sciences**, 3 Constitution Avenue, G-5/2, Islamabad, Pakistan
Email: editor@paspk.org; **Tel:** 92-51-920 7140 & 921 5478; **Websites:** www.paspk.org/proceedings/; www.ppaspk.org

Printed at **Graphics Point.,** Office 3-A, Wasal Plaza, Fazal-e-Haq Road Blue Area Islamabad.
Ph: 051-2806257, **E-mail:** graphicspoint16@gmail.com

PROCEEDINGS OF THE
PAKISTAN ACADEMY OF SCIENCES: PART A
Physical and Computational Sciences

CONTENTS

Volume 63, No. 2, June 2026 **Page**

Research Articles

Submission of Manuscripts: Manuscripts may be submitted as an e-mail attachment at editor@paspk.org or submit online at http://ppaspk.org/index.php/PPASA/about/submissions. Authors must consult the ***Instructions for Authors*** at the end of this issue or at the Website: www.paspk.org/proceedings/ or www.ppaspk.org.

Proceedings of the Pakistan Academy of Sciences: A Physical and Computational Sciences 63(2): 83-97 (2026)

ISSN (Print): 2518-4245; ISSN (Online): 2518-4253
http://doi.org/10.53560/PPASA(63-2)712

Pakistan Academy of Sciences

Research Article

Improved Workability and Strength of Rubberized Mortar Using Supplementary Cementitious Materials and Polypropylene Fibers

Muhammad Huzaifa Zafar, Umer Aziz, Abdul Basit Wani, Shayyan Shaukat, and Anwar Khitab*

Department of Civil Engineering, Mirpur University of Science and Technology (MUST), Mirpur-10250, (AJ&K) Pakistan

Abstract: The recent past has shown that rubberized cementitious composites, despite their potential benefits such as improved ductility, impact resistance, and utilization of waste rubber, exhibit reduced workability and mechanical strength. This performance degradation is attributed to the lower density and higher elastic nature of rubber particles, which hinder compaction efforts and induce voids. Also, the hydrophobic nature of rubber particles repels water molecules and gives rise to pores. Present research focuses on improving the workability and strength of rubberized composites by using waste materials like silica fumes and fly ash and adding polypropylene fibers. A 1:4 cement-sand mortar was prepared as a control specimen. A systematic study was conducted in which the ingredients were added incrementally. First, 5% of the sand was replaced with crumb rubber. In the next group of samples, silica fume and fly ash were included as extra materials in the cement, replacing 2.5% of the cement's weight. Subsequently, a water reducer was introduced. Finally, in the last set of specimens, polypropylene fibers were added at a rate of 0.1% by volume of mortar. The results revealed that the incorporation of crumb rubber reduced the 28-day compressive strength from 8.5 MPa to 4.55 MPa, corresponding to a strength loss of 46%. The proposed modifications reduced this strength loss to only 7.4%, resulting in a 28-day compressive strength of 7.9 MPa. Similarly, the flow value increased from 80 mm to 100 mm after the incorporation of supplementary cementitious materials. It is concluded that the careful incorporation of supplementary cementitious materials and synthetic fibers can improve the mechanical strength and workability of rubberized mortar.

Keywords: Rubberized Mortar, Supplementary Cementitious Materials, Polypropylene Fibers, Workability, Strength.

1. INTRODUCTION

The rubberized cementitious composites are preferred in many situations, including sound insulation, impact resistance, shock absorption, repair and restoration, and where high flexibility is required. The drawbacks include lower workability and compressive strength, which hinder its applications in normal concrete construction. The rubberized particles are extracted from waste rubber tires. These tires are an important waste material because it is thought that rubber is not a biodegradable material, and its dumping requires space, which is already short due to population increase and urbanization [1, 2]. There is a need to recycle the waste tires so that they do not require dumping spaces for disposal. One safe method to dispose of the waste rubber tires is recycling them in building materials like mortar, concrete, bricks, and tiles [3]. Several researchers in the recent past have used rubber particles in cementitious composites.

Liu *et al.* [4] worked on rubberized concrete. The authors have reported that, with the addition of crumb rubber, the compressive strength of concrete decreased significantly. Other researchers, such as Qureshi *et al.* [5], Assaggaf *et al.* [6], and Youssf *et al.* [7], have also found that when sand is partially replaced with crumb rubber (between 5% and 25%), the compressive strength of concrete decreases, and this decrease becomes larger as more rubber is added. Similar studies are available

Received: December 2025; Revised: May 2026; Accepted: June 2026
* Corresponding Author: Anwar Khitab <anwar.ce@must.edu.pk>

about the reduction of tensile strength in concrete with the inclusion of rubber content [8]. There are numerous studies available that depict that the rubber content reduces the workability of concrete. It has been reported that the rubber particles have a rough surface and high water absorption. This discrepancy of rubber particles induces void spaces and reduces workability [9]. The past research shows that the workability and the mechanical strength of rubberized cementitious composites are reduced due to rough surface, more water absorption, and induced void content. Yet there are other situations where rubber content has positively impacted the cementitious composites. According to Khan *et al*. [10], when strength is not as important as toughness and deformability, rubberized concrete can be effectively used for road foundations and bridge barriers. Rubber-based concrete can be used to reduce vibrations in structural foundations since it has reversible elasticity. Eltayeb *et al*. [11] utilized crumb rubber as a partial replacement for sand in concrete mixtures, with substitution levels ranging from 0% to 50%. The findings indicated that rubberized concrete exhibited superior resistance to bullet impacts, blast loads, high-velocity impacts, and collisions compared to unreinforced concrete. Also, adding rubber greatly improved the ductility, energy absorption, and weakening of structural parts when they faced repeated and earthquake-related stresses. Kashani *et al*. [12] investigated the performance of lightweight cellular concrete (LCC) incorporating waste crumb rubber as a filler. In their study, the crumb rubber was pretreated with an NaOH solution to improve its interaction with the cement matrix. The findings indicated that the incorporation of crumb rubber improved the acoustic and thermal insulation characteristics of LCC while simultaneously decreasing its water absorption. Furthermore, the NaOH pretreatment improved the compressive strength of the LCC by promoting a stronger bond between the crumb rubber and cement paste, as evidenced by SEM analysis.

Previous studies [4, 5, 13] have found that rubberized cement mixtures usually have lower workability and strength but better performance in terms of dynamic, thermal, and sound insulation. Researchers primarily studied the enhancement of workability and strength by pretreating the rubber particles with a suitable alkaline solution. Although alkaline pretreatment has been reported to enhance the bond between rubber particles and the cementitious matrix and provide modest improvements in mechanical properties, the magnitude of improvement remains limited. Therefore, alternative approaches are still needed to further enhance the workability and strength of rubberized cement mixtures.The current research aims to improve the workability and strength of rubberized cement mixtures (mortar) by using industrial waste materials such as silica fumes, fly ash, polypropylene (PP) fibers, and a water reducer. The study used a step-by-step experimental method, trying out different combinations based on literature review to gradually improve the mix design while keeping scientific control. A systematic approach was adopted, and the parameters were examined by a stepwise addition/substitution for clearly watching the effect of each new addition or substitution. Mortar samples were tested for density, flowability, water absorption, and mechanical strength because these traits together determine the compaction behavior, durability, and structural viability of rubberized mortars.

2. MATERIALS AND METHODS

For this experimental investigation, a 1:4 cement–sand mortar was used as a reference material to ensure consistency and comparability in evaluating the effects of rubber incorporation and subsequent modifications. Grade 53 cement (OPC-Type I) and river sand were used as the ingredients. Recently, we have investigated the properties of rubberized cementitious mortar [14]; some of these results are used as reference materials in the present study. The characteristics of cement are presented in Table 1. The domination of CaO, together with sufficient

Table 1. Chemical composition of cement [14].

Compound	Percentage
CaO	63%
SiO_2	22%
Al_2O_3	5.5%
MgO	1.7%
SO_3	1.8%
Fe_2O_3	3.5%
Na_2O	0.2%
K_2O	1%
Loss of Ignition	0.6%

SiO_2 and Al_2O_3 contents, indicates the suitability of the cement for normal hydration and strength development. The Fe_2O_3 content falls within the typical range for ordinary Portland cement. The relatively low MgO (1.7%) and SO_3 (1.8%) contents suggest a low risk of unsoundness and appropriate control of setting time. The low alkali contents (Na_2O and K_2O) reduce the potential for alkali–silica reaction, while the very low loss on ignition (0.6%) indicates minimal pre-hydration or impurities. Overall, the composition reflects good chemical stability and suitability for mortar production [15].

Table 2 lists the key physical characteristics of sand. The specific gravity and fineness modulus indicate a well-graded sand suitable for mortar applications. The bulk and dry rodded bulk density values fall within typical ranges for natural sand, reflecting stable packing characteristics and enabling consistent mix proportioning. Furthermore, the moderate water absorption indicates limited moisture demand, which helps maintain adequate workability without requiring excessive water addition [16].

Waste rubber tires were collected from the local market and were converted into fine powder. The fine particles were sieved through sieve # 4 (4.75 mm). The material that passed through the sieve was further used as a partial replacement of sand. This practice was performed because the sand particles have a size range from 2.00 mm to 4.74 mm [17]. The characteristics of rubber particles are given in Table 3. The specific gravity of the crumb rubber was determined using the water-displacement method. The relatively high value obtained may be attributed to the heterogeneous nature of recycled tire rubber, which contains carbon black, fillers, and other constituents originating from end-of-life automobile tires.

Table 2. Physical properties of sand.

Parameter	Value
Specific Gravity	2.5
Fineness Modulus	2.6
Bulk Density (Kg/m^3)	1490
Dry rodded Bulk Density (Kg/m^3)	1780
Water absorption (%)	2

Table 3. Physical properties of crumb rubber [14].

Parameter	Value
Specific Gravity	1.66
Color	Dark Black
Surface	Rough
Fineness Modulus	3.9
Water absorption (%)	1.25

The crumb rubber exhibits a relatively low specific gravity than fine aggregates and a coarse particle size, as indicated by the high fineness modulus. These characteristics are expected to reduce the overall density of the mortar and affect its compaction behavior and fresh-state workability. In addition, the rough surface texture may enhance mechanical interlocking with the cementitious matrix, potentially improving the bond between rubber particles and the surrounding paste.

The characteristics of silica fume (SF) and fly ash (FA) are mentioned in Table 4. Silica fume has a high level of SiO_2, indicating a strong pozzolanic potential and the ability to react with calcium hydroxide to form additional cementitious products like calcium silicate hydrate gel (C-S-H) [18]. In contrast, fly ash exhibits a more balanced composition, with significant amounts of SiO_2 (33.5%), Al_2O_3 (13%), Fe_2O_3 (34.3%), and CaO (13%). Although the Fe_2O_3 content is relatively high, the combined content of SiO_2, Al_2O_3, and Fe_2O_3 exceeds 70%, satisfying the ASTM C618-19 requirement for Class F fly ash .This combination suggests that fly ash can contribute to both pozzolanic reactions and micro-filler effects,

Table 4. Chemical composition of silica fumes and fly ash [14].

Compound	Silica fumes (%)	Fly ash (%)
Al_2O_3	-	13
CaO	0.43	13
Fe_2O_3	-	34.3
SiO_2	95.73	33.5
K_2O	1.87	1.7
Na_2O	0.38	-
TiO_2	0.93	2.1
ZrO_2	0.11	0.41
V_2O_5	-	0.93
SrO	0.03	0.23

enhancing particle packing and long-term strength development in the mortar matrix [19].

The characteristics of PP fibers are mentioned in Table 5. The fibers have a low density and high tensile strength, making them effective for controlling microcracking and improving post-cracking behavior in mortar. Additionally, the high melting temperature indicates that the fibers remain stable under normal service conditions, ensuring reliable performance within the cementitious matrix [20].

A polycarboxylate ether (PCE)–based third-generation superplasticizer was also used along with the abovementioned materials. The plasticizer met ASTM C494 Type F/G requirements and is used to control the workability of the mortar mixtures [21]. All the ingredients except admixture are shown in Figure 1. Five types of mortars were prepared, and their compositions are mentioned in Table 6. In Table 6, all quantities are given in kg, except water and water reducer, which are in liters. It is reiterated that a systemic study (in steps) was conducted to improve the performance of the rubberized mortars.

Table 5. Characteristics of polypropylene fibers [14].

Parameter	Description
Density (g/cm^3)	0.9
Melting (ºC)	160
Tensile strength (MPa)	350
Color	White and translucent

As a first step, the rubber content was fixed at 5% by mass of sand. This lower amount of rubber was chosen on purpose to see how the material behaves with a small amount of rubber, giving a clear starting point to understand its effects before trying larger amounts for further studies. In all cases, the total binder content and the total filler content remained at 383 kg and 1755 kg, respectively. The water-to-binder ratio was kept constant at 0.6 in all cases, except M3 and M4, where the water content was reduced by 15% owing to the use of the superplasticizer (manufacturer recommendation). Silica fumes and fly ash were each used at 2.5% by mass of cement. The content was selected to maintain a moderate total cement replacement level of 5% while benefiting from their combined pozzolanic effects. A polypropylene fiber content of 1.2 kg/m^3, corresponding to approximately 0.13% by volume, falls well within the commonly reported range for fiber-reinforced mortars and concretes [22]. In practice, PP fibers are usually added at 0.1–0.3% by volume to help control cracks, reduce shrinkage, and improve the material's response after cracking. Higher PP fiber content decreases workability and may lead to fiber agglomeration.

The mortar specimens were mixed and prepared according to ASTM standard ASTM C305-20 [23]. All the specimens were prepared in a Hobart mixer. After mixing, the specimens were molded in three-gang molds and prisms. After casting, the specimens were covered with a plastic sheet for 24 h to minimize moisture loss. The specimens were then demolded and submerged

Fig. 1. Raw materials used for producing control and rubberized cementitious mortars.

Table 6. Composition of one cubic meter of mortar.

ID	C	S	W	R	SF	FA	SP	PP
M0	383	1755	230	0	0	0	0	0
M1	383	1667	230	88	0	0	0	0
M2	364	1667	230	88	9.5	9.5	0	0
M3	364	1667	195	88	9.5	9.5	5.7	0
M4	364	1667	195	88	9.5	9.5	5.7	1.2

ID: Specimen identity, C: Cement, S: Sand, W: Water, R: Crumb Rubber, SF: Silica Fumes, FA: Fly Ash, SP: Superplasticizer, PP: Polypropylene Fibers.

in tap water until the specified testing ages (7 and 28 days). The fresh and hardened densities were determined in accordance with the ASTM C138-17 [24] and ASTM C642 [25] standard methods, respectively. The flowability was examined according to the ASTM C1437-20 standard method [26]. The standard ASTM C109/C109M-20 method was used to measure the compressive strength [27].

3. RESULTS AND DISCUSSION

Figure 2 illustrates the hardened specimens in the gang mold after one day of curing. M0 represents the control mortar containing only cement (C), sand (S), and water (W). In M1, 5% of the sand (by mass) was replaced with crumb rubber. This modification changed the aggregate grading and was expected to affect workability and packing density. M2 is a modification of M1; it includes silica fume and fly ash as supplementary cementitious materials. These materials partially replace cement to improve packing, pozzolanic activity, long-term strength, and permeability.

M3 is a modification of M2. A superplasticizer was added, and the mixing water was reduced while maintaining workability. This modification is expected to enhance strength and durability by reducing the water-to-binder ratio and improving the dispersion of fine particles. M4 is a further modification that incorporates polypropylene fibers in addition to all previous constituents. The fibers enhance crack resistance, toughness, and post-cracking behavior but may slightly reduce flowability due to mechanical interlocking.

Overall, moving from M0 to M4 shows a clear change in the mortar from a regular mix to a high-quality composite that includes mineral additives, chemical additives, and fibers. The

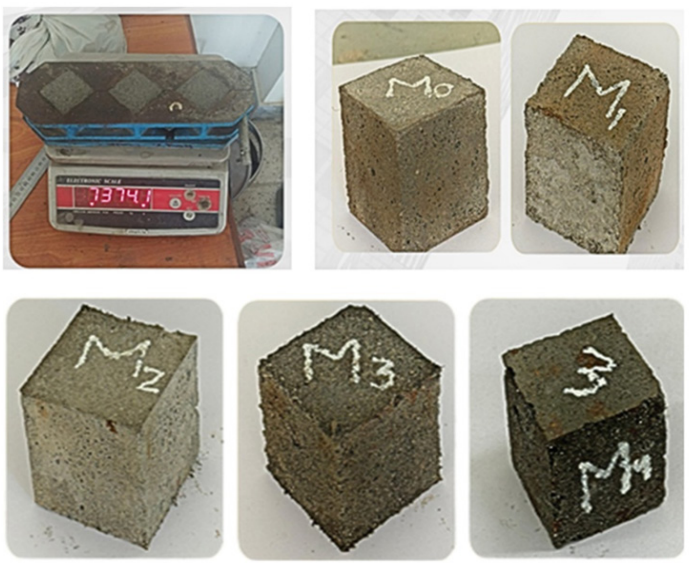

Fig. 2. Mortar casting process from three-gang mold to hardened cube specimens.

observable differences in fresh-state appearance and consistency during molding reflect the combined effects of particle size distribution, water content, and the action of the incorporated admixtures.

3.1. Density

Figure 3 shows the variations of density in the fresh state and at one day of age. For the density determination, six samples were tested for each mix type, and the reported values represent the average of six measurements. The results revealed that the mean fresh density of the reference mortar (M0) was 2.1 g/cm^3. As the sand was partially replaced by crumb rubber, the density was reduced by 20%. The incorporation of rubber particles reduced the density of cementitious composites, primarily because rubber is significantly lighter than natural sand. The sand particles have a specific gravity of 2.5 (Table 2), while the crumb rubber particles possess a specific gravity of 1.66 (Table 3). Also, because rubber doesn't mix well with water and fresh cement paste, it creates trapped air pockets, which makes the composite more porous [28]. Thus, the inclusion of pores due to rubber further reduced the density of the mortar specimens. Next, when silica fumes and fly ash were added, the loss of density caused by rubber particles was reduced from 20% to 17%. The addition of a water reducer further decreased the loss, from 17% to 13%. And lastly, when PP fibers were added, the loss was further reduced to 5%.

Fly ash and silica fume are very fine materials that help fill in the gaps in the cement matrix, making the mix denser [29]. At early ages, the improvement in density is primarily due to physical effects, including filler action and enhanced particle packing, rather than pozzolanic reactions. The fine particles occupy spaces between cement grains, reduce initial porosity, and refine the microstructure. This leads to a denser matrix and may improve early-age strength and reduce bleeding and permeability. A water reducer, also known as a plasticizer or superplasticizer, enhances the density of cementitious composites by reducing the water required to achieve the desired workability [30]. By lowering the water content while maintaining or improving flowability, it produces a more compact mixture with fewer voids. It was also observed that the inclusion of fibers reduced the loss in density from 13% to 5%. Polypropylene (PP) fibers are generally expected to decrease density because of their low specific gravity [31]. However, they can also improve density by increasing mixture cohesiveness and helping to hold the constituents together [32]. This improved cohesion reduces air entrapment and void formation within the composite, thereby decreasing the overall volume. Because density is inversely related to volume, a reduction in volume results in an increase in overall density [33]. Higher density leads to higher strength and vice versa. Previous studies on conventional cementitious systems have shown that mineral additives, plasticizers, and fibers can enhance

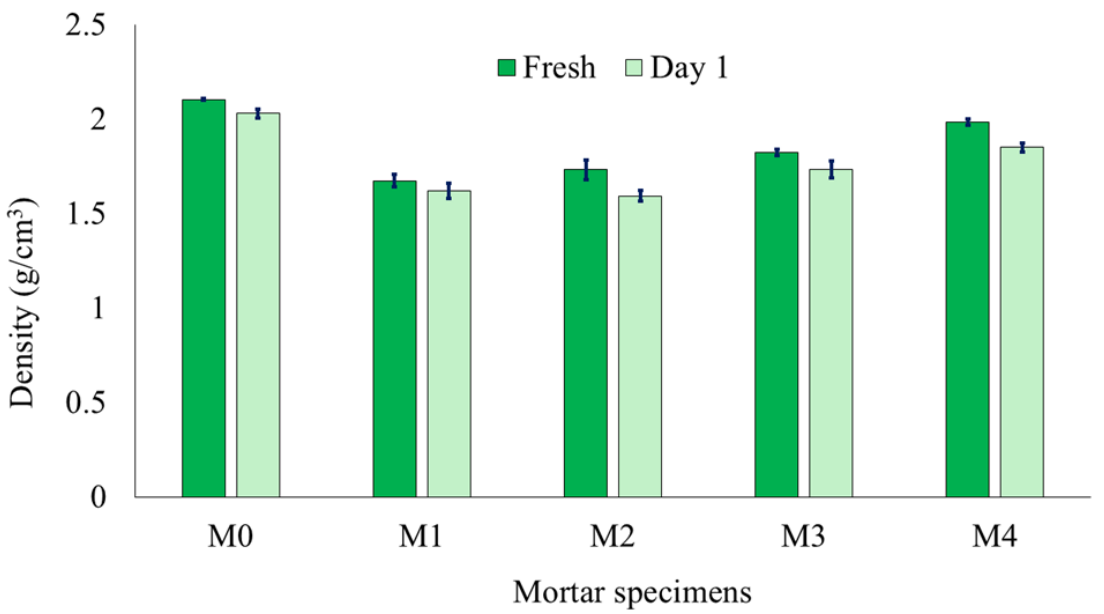

Fig. 3. Density of mortar specimens in the fresh state and after one day of curing.

material performance through improved packing, reduced water demand, and crack control [34-36].

3.2. Workability

The workability was examined by a flow table test. For each mix type, four specimens were tested and the mean flow was calculated from the recorded measurements. Figure 4 illustrates the experimental setup for assessing the flow value of mortar. The flow table test is a standard method for evaluating the workability and consistency of fresh mortars by measuring their ability to deform under controlled dynamic loading. The resulting flow value reflects the combined influence of water content, particle grading, and admixtures on the rheological behavior of the mix, thereby indicating ease of placement and compaction. It is especially useful for mortars containing SCMs or fibers, which can markedly alter cohesion and viscosity [26, 37].

Figure 5 presents the effect of the additives on workability. The workability, as presented by the flow value, varies across the specimens. It seems to be a function of the additive's content and the volume of fibers and plasticizer. The incorporation of fine mineral additives can modify the water demand and particle packing of the mortar, thereby influencing its flow characteristics. Fibers generally reduce workability due to mechanical interlocking and increased internal friction, which restricts the free movement of the mix. In contrast, the presence of a superplasticizer improves dispersion of cement particles and reduces yield stress, resulting in enhanced flow despite low water content. Therefore, the observed variations in flow values reflect the competing effects of filler action, fiber reinforcement, and chemical admixture on the rheological behavior of the fresh mortar [26, 37]. The flow value of the control specimens was 100 mm. The value decreased to 80 mm when rubber

Fig. 4. Setup for measuring mortar flow using a flow table.

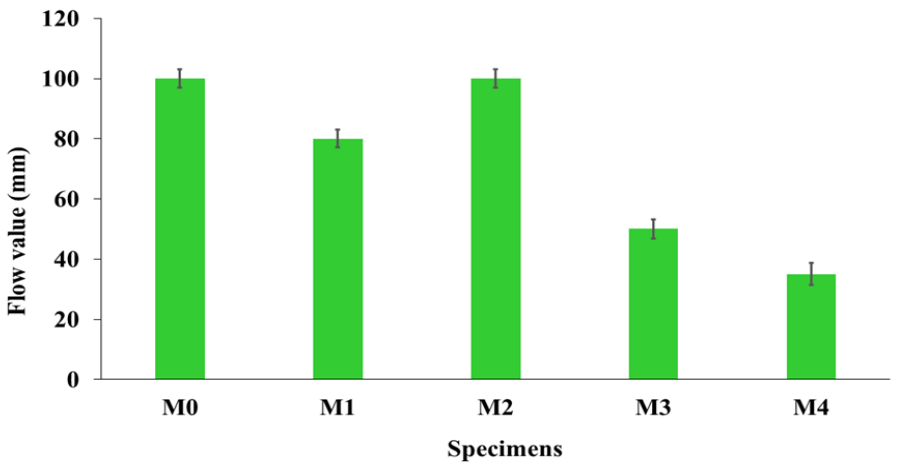

Fig. 5. Variation of flow value with additives.

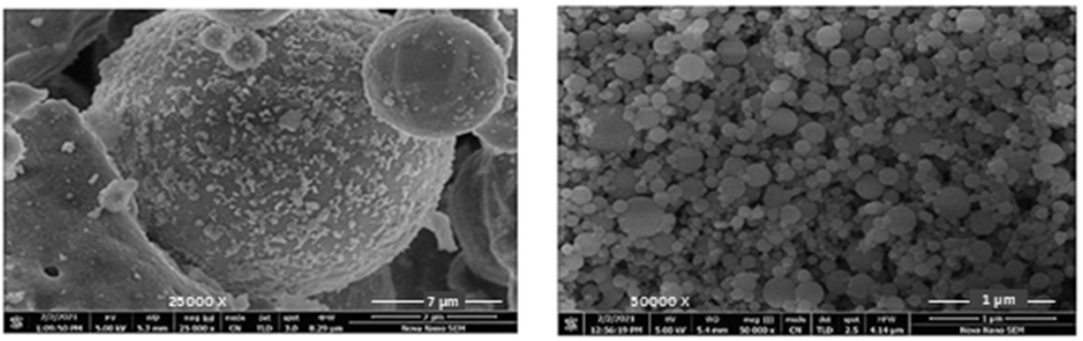

Fig. 6. SEM images of fly ash particles (on left) and silica fume particles (on right).

was incorporated. This reduction is attributed to several factors, including the rough surface texture of rubber particles, which impedes flow. In addition, rubber particles have a lower density, which causes them to float and segregate from the rest of the mix. Rubber particles also tend to entrap air, which resists movement of the mix. The entrapped air induces pores, leading to a reduction in overall density. Thus, the flowability is also linked to the density [38]. As silica fumes and fly ash were added, the loss in flow was substantially recovered. Figure 6 displays the silica fumes and fly ash particles used in this research work.

Fly ash particles are smooth and round, which makes them easier to flow and pack within the matrix. Silica fume particles, on the other hand, are very fine and uneven, which helps fill in gaps and make the mixture denser. Their contrasting morphologies highlight their complementary roles in modifying fresh and hardened properties of cementitious composites [29].

Fly ash is added at a rate of 15-35% by mass of cement, whereas silica fumes are added at a rate of 5-10% by mass of cement [39]. Silica fume is used in smaller amounts than fly ash because its extremely fine particles and high reactivity can produce significant effects even at low dosages. However, excessive use may adversely affect workability and increase shrinkage [40]. For the current study, lower levels were decided, i.e., 2.5% each. The literature survey shows that a lower level of fly ash particles significantly improves workability, whereas a lower level of silica fumes provides a good balance between strength and workability [41]. Thus, for improving the workability of rubberized cementitious composites, lower levels of silica fumes and fly ash are recommended.

Subsequently, a water-reducing admixture was incorporated into the mix, and the water content was decreased by 15% (Table 6) in accordance with the manufacturer's recommendations. Despite this adjustment, the expected improvement in workability was not achieved; instead, the flow value dropped from 100 mm to 50 mm. This indicates that the prescribed water reduction was not suitable for the specific composition of the mortar used in this study. The reduced flow may be attributed to the combined effects of a lower effective water content and the prevailing hot weather during casting, which likely accelerated moisture loss and early hydration, thereby increasing the stiffness of the mix. The specimens were cast during the month of July 2024. The average heat index was calculated to be 44 ºC, and the average humidity was 40% [42]. To ensure the consistency and comparability of the experimental results, all the mortar combinations were prepared and tested under identical environmental conditions.The dosage of the water reducer typically lies between 0.1 to 1.5% (by mass of cementitious binder) [43]. Thus, for this work, an average dosage was used. The lower humidity and high temperature enhance water demand. The substantial reduction in flow is primarily attributed to the 15% reduction in mixing water associated with the use of the water-reducing admixture. The high ambient temperature during casting may also have contributed to a greater water demand and accelerated moisture loss; however, this effect was not directly quantified in the present study. Thus, there is a need for an optimum water reducer content for maintaining the workability of the mix in hot weather conditions. Lastly, when PP fibers were added, the flow value further declined. PP fibers tend to hold the mix together, forming a cohesive network that restricts particle movement. In addition, these synthetic fibers can

absorb or retain water on their surfaces, reducing the amount of free water available for lubrication [44]. Consequently, the flow value decreases. The overall study suggests that a careful selection of SCMs can enhance workability alone. The addition of fibers might enhance the strength but is not useful for the workability of the rubberized composites.

3.3. Compressive Strength

The compressive strength was determined at two ages: 7 and 28 days. The respective results are shown in Figure 7. All values represent an average of three measurments for each mix.The 7-day strength indicates early hydration and initial load-bearing capacity of the mortar. It reflects cement reactivity and the early effects of additives. The 28-day strength is the standard reference for structural performance and quality evaluation. It represents more complete hydration and microstructural development. Comparing these two ages helps assess both early performance and long-term strength gain [45, 46].

The 28-day compressive strength of control specimens is 8.5 MPa, which was reduced to 4.55 MPa when sand was partially replaced by rubber particles. The 28-day compressive strength of control specimens may appear modest compared with standard laboratory mortars, it falls within the range commonly reported for 1:4 cement–sand mortars with similar water-to-binder ratios. The mortar was prepared using locally available Mangla river sand, and comparable strength levels have been reported in studies employing similar materials and mix proportions [47]. Furthermore, the control mix serves as a reference mixture for comparative evaluation of the effects of crumb rubber, supplementary cementitious materials, water-reducing admixture, and polypropylene fibers. Therefore, the relative changes in strength are of primary significance in the present investigation. This decrease from 8.5 MPa to 4.555 MPa is attributed to void formation, weak interfacial bonding with the cement paste, and the low stiffness of rubber particles, which act as soft inclusions [48, 49]. These factors create stress concentration points and initiate microcracks, leading to reduced strength. When mineral additives were added, the strength further decreased from 3.18 MPa to 3.01 MPa at 7 days and from 4.55 MPa to 4.3 MPa at 28 days, corresponding to a reduction of about 5% at both ages. Supplementary cementitious materials such as silica fume and fly ash often show limited early-age benefits in rubberized systems because their pozzolanic reactions are time dependent. Higher strength gains are typically observed at later ages, such as 56 days and beyond [50].

The incorporation of a water-reducing admixture resulted in a 43% increase in compressive strength at both 7 and 28 days. This improvement can be attributed to the 15% reduction in the water-to-cement ratio, which produced a denser microstructure with improved particle packing and stronger interfacial bonding within the matrix. Water-reducing admixtures or plasticizers enhance strength by reducing water-to-cement ratio, resulting in a denser and less porous cementitious matrix. This reduction in excess water decreases

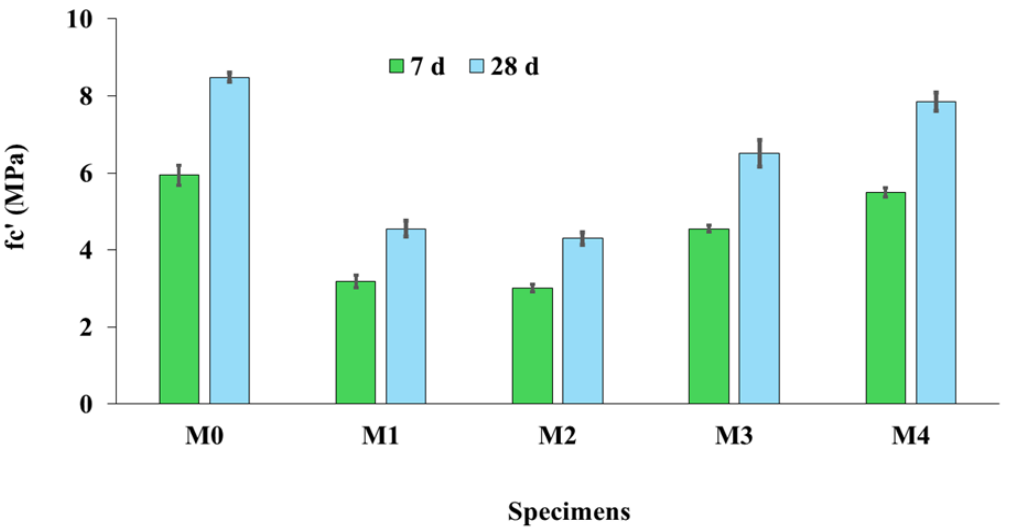

Fig. 7. Compressive strength of control and rubberized mortars after 7 and 28 days of curing.

the formation of capillary voids within the hardened matrix. It also improves particle packing, allowing the solid constituents to occupy the available space more efficiently. In addition, the lower water content promotes more effective cement hydration. Furthermore, it strengthens the bond between the cement paste and aggregates. Collectively, these effects lead to higher compressive strength [51, 52]. The addition of polypropylene fibers resulted in a 73% strength increase compared with M1 (rubberized specimens without mineral additives, fibers and plasticizer). Fibers help bridge microcracks and improve stress transfer, partially compensating for the weakness introduced by rubber particles [53]. At 28 days, rubberized specimens (M1) showed a 46% reduction in strength compared with control specimens (M0), but this reduction decreased to 7.4% after incorporating silica fume, fly ash, water reducer, and PP fibers. Similar synergistic improvements from combined mineral and fiber modifications have been reported in recent studies [54, 55]. The next section further elaborates on the effects of additives, fibers, and plasticizers.

3.4. Relation between Density and Compressive Strength

Figure 8 illustrates the relationship between density and compressive strength. This relationship is important because density strongly influences load-bearing performance, structural weight, and material efficiency. Higher density usually means fewer pores, voids, and defects. In materials like concrete, this generally leads to higher strength because the load is carried through a more continuous solid matrix [33]. The results indicate a strong positive correlation, with higher-density mixes exhibiting greater compressive strength. The reduction in density and strength in rubberized mortars is attributed to the low stiffness and lightweight nature of crumb rubber particles. On the other hand, adding silica fume, fly ash, and PP fibers helped to better arrange the particles and make the mixture denser, which improved its strength. A strong positive trend was observed between density and compressive strength (R^2 = 0.92). However, the relationship was derived from a limited dataset comprising five mix types and should therefore be interpreted as indicative rather than conclusive. Many studies have reported a positive relationship between density and compressive strength because denser materials contain fewer voids and can distribute applied loads more effectively [56, 57]. This benefit is attributed to the addition of finer particles of silica fumes and fly ash as well as a reduced water content. Extra water is a source of voids formation. The addition of fibers results in stronger bonds between particles, enhancing the material's ability to withstand compressive forces. Thus, using lower dosages of SCMs, a water reducer, and PP fibers can enhance the density and strength of a rubberized cementitious composite.

3.5. Effect of Fibers on Crack Formation

The crack formation was carefully observed during the compressive strength test. The difference of crack formation in the specimens M1 and M4 can be seen in Figure 9. Visual assessment of crack patterns provides valuable insight into the failure mode and internal integrity of cementitious materials. The width, orientation, and distribution of cracks indicate the brittleness or ductility of the specimen. Localized and wide cracks typically suggest weak bonding and sudden failure, whereas multiple fine cracks reflect improved stress redistribution and energy absorption. Such observations complement compressive strength results by revealing the influence of additives and fibers on crack resistance and post-peak behavior [45, 46]. The control mortar (M0) showed brittle failure with sudden rupture and a large crack. This indicates low energy absorption capacity. In contrast, M4, which contained fibers and mineral additives, developed only fine hairline cracks. Another notable observation was the reduction in delamination due to the additives and fibers. Severe delamination was observed in M1 (rubberized mortar). However, M4 maintained strong internal cohesion. Overall, the additives and

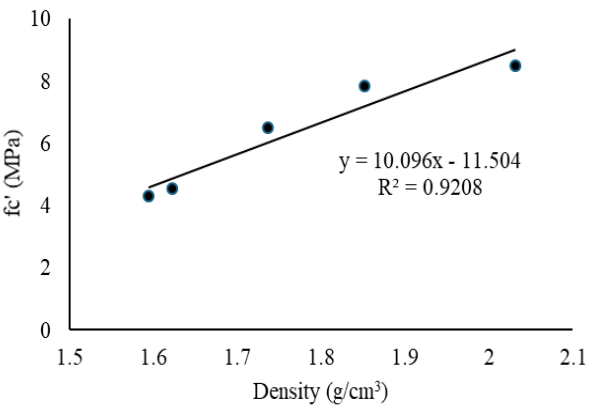

Fig. 8. Variation of compressive strength with density.

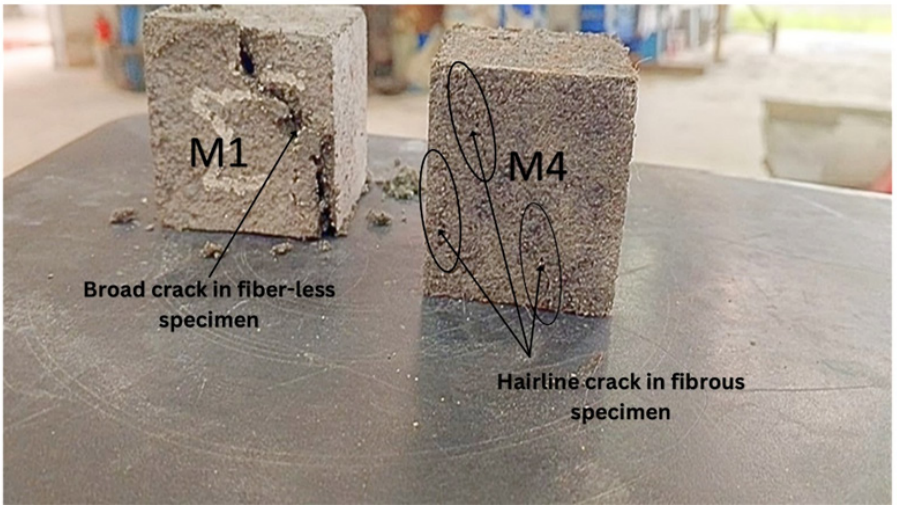

Fig. 9. Comparison of crack patterns in specimens M1 (left) and M4 (right).

fibers effectively controlled crack propagation and improved structural integrity. Fibers acted as crack bridges and restricted crack widening [58]. This prevented sudden fracture and helped maintain the integrity of the specimen. Mineral additives densified the matrix and reduced internal voids. The improved microstructure enhanced the bond among the constituents [59]. Consequently, the material was able to sustain higher deformation before failure. In contrast, the rubberized mortar exhibited weak interfacial bonding, which led to layer separation. The modified mortar therefore showed a more stable and damage-tolerant failure mode.

4. CONCLUSIONS

This study was conducted to improve the performance of rubberized cementitious mortar for subsequent application to concrete specimens. The addition of 5% silica fume and fly ash (combined), along with 0.1% polypropylene (PP) fibers, significantly increased the density of the rubberized mortar. The one-day hardened density increased from 1.60 to 1.90 g/cm³ following the incorporation of SCMs and PP fibers. This value approaches the one-day hardened density of the control 1:4 cement–sand mortar (2.03 g/cm³). The same 5% SCM combination also improved the flow value from 80 mm to 100 mm, which is comparable to the workability of the control mix. In contrast, the inclusion of PP fibers alone markedly reduced the flow value from 80 mm to 35 mm. This reduction is attributed to fiber-induced interlocking and volumetric restriction within the matrix. The incorporation of rubber particles reduced the compressive strength from 8.5 MPa to 4.5 MPa, representing a loss of 46%. However, this reduction was substantially mitigated when silica fume, fly ash, a water-reducing admixture, and PP fibers were used together. Under these conditions, the strength loss was limited to only 7%. Rubberized cementitious composites generally exhibit reduced workability and mechanical strength but improved dynamic properties. These characteristics limit their use in structural applications. Nevertheless, workability can be effectively enhanced using SCMs with ball-bearing effects, such as fly ash and silica fume. The observed increase in flow from 80 mm to 100 mm was achieved through the incorporation of SCMs alone. In contrast, the addition of a water-reducing admixture with reduced mixing water and polypropylene fibers resulted in lower flow values but contributed to strength recovery. Mechanical performance can therefore be partially restored through the combined use of SCMs, water-reducing admixture, and fiber reinforcement.

5. ETHICAL STATEMENT

All experimental work was conducted on laboratory-prepared cementitious materials. No experiments involving human participants or animals were performed; hence, ethical approval was not applicable.

6. ACKNOWLEDGEMENT

The authors are grateful to their colleagues in the civil engineering department MUST for the assistance, which enabled them to complete this work in time.

7. CONFLICT OF INTEREST

The authors declare that they have no conflict of interest.

8. DECLARATION

The authors declare that the results presented in this manuscript are original and have not been published previously, nor are they under consideration for publication elsewhere. All authors have reviewed and approved the final version of the manuscript and agree to its submission. All data and figures presented in this work are original and generated by the authors; therefore, no copyright permission from other sources was required. In the event that the article is accepted for publication, the authors agree to assign the copyright of the manuscript to the Pakistan Academy of Sciences.

9. AI Statement

No AI tools were used for data generation, analysis, or figure preparation. All scientific interpretations remain the sole responsibility of the authors. Artificial intelligence–based tools were used only to assist with language editing and formatting.

10. FUNDING

No funding was received to conduct this research.

11. REFERENCES

1. K. Formela. Sustainable development of waste tires recycling technologies – recent advances, challenges and future trends. *Advanced Industrial and Engineering Polymer Research* 4(3): 209-222 (2021). https://doi.org/10.1016/j.aiepr.2021.06.004
2. M. Naddeo, G. Viscusi, G. Gorrasi, and D. Pappalardo. Degradable Elastomers: Is There a Future in Tyre Compound Formulation? *Molecules* 26(15): 4454 (2021). https://doi.org/10.3390/molecules26154454
3. A.Q. Bhatti and A. Khitab. A clean approach through recycling of brick kiln dust and crumb waste rubber tires in the manufacturing of clayey bricks and cementitious composites. In: Advance Upcycling of By-Products in Binder and Binder-Based Materials. M.S. Kırgız (Ed.). *Elsevier, USA* pp. 291-307 (2024). https://doi.org/10.1016/B978-0-323-90791-0.00015-9
4. L. Liu, Q. Guan, L. Zhang, C. Liu, X. Chen, and X. Cai. Evaluation of the compressive-strength reducing behavior of concrete containing rubber aggregate. *Cleaner Materials* 4: 100057 (2022). https://doi.org/10.1016/j.clema.2022.100057
5. M. Qureshi, J. Li, C. Wu, and D. Sheng. Mechanical strength of rubberized concrete: Effects of rubber particle size, content, and waste fibre reinforcement. *Construction and Building Materials* 444: 137868 (2024). https://doi.org/10.1016/j.conbuildmat.2024.137868
6. R.A. Assaggaf, S.U. Al-Dulaijan, M. Maslehuddin, O.S.B. Al-Amoudi, S. Ahmad, and M. Ibrahim. Effect of different treatments of crumb rubber on the durability characteristics of rubberized concrete. *Construction and Building Materials* 318: 126030 (2022). https://doi.org/10.1016/j.conbuildmat.2021.126030
7. O. Youssf, M.A. Elgawady, J.E. Mills, and X. Ma. An experimental investigation of crumb rubber concrete confined by fibre reinforced polymer tubes. *Construction and Building Materials* 53: 522-532 (2014). https://doi.org/10.1016/j.conbuildmat.2013.12.007
8. Z. Jiang, X. Zhang, Y. Zhang, L. Yu, X. Hu, X. Zhou, and Y. Zhang. Surface Treatment of Rubberized Waste Reinforced Concrete. *Frontiers in Built Environment* 7: 685067 (2021). https://doi.org/10.3389/fbuil.2021.685067
9. U. Jonathan and M. Khaled. Effect of waste crumb rubber tyre as partial replacement of fine aggregates on fresh and hardened properties of concrete. *International Journal of Physical Sciences* 19(2): 96-111 (2024). http://doi.org/10.5897/IJPS2024.5068
10. R.B.N. Khan and A. Khitab. Enhancing Physical, Mechanical and Thermal Properties of Rubberized Concrete. Engineering and Technology Quarterly Reviews 3(1): 33-45 (2020). https://doi.org/10.5281/zenodo.3852541
11. E. Eltayeb, X. Ma, Y. Zhuge, J. Xiao, and O. Youssf. Dynamic performance of rubberised concrete and its structural applications – An overview. Engineering Structures 234: 111990 (2021). https://doi.org/10.1016/j.engstruct.2021.111990
12. A. Kashani, T.D. Ngo, P. Mendis, J.R. Black, and A. Hajimohammadi. A sustainable application of recycled tyre crumbs as insulator in lightweight cellular concrete. *Journal of Cleaner Production* 149: 925-935 (2017). https://doi.org/10.1016/j.jclepro.2017.02.154
13. O. Youssf and M. ElGawady. An overview of sustainable concrete made with scrap rubber. In: From Materials to Structures: Advancement Through Innovation - Proceedings of the 22nd Australasian

Conference on the Mechanics of Structures and Materials, ACMSM 2012, Sydney Australia, 11-14 December 2012. *CRC Press*, *London, UK* pp. 1039-1044 (2012). https://doi.org/10.1201/b15320-185

14. S.Z. Ejaz, C.T. Shafqat, U. Jameel, H. Choudary, and A. Khitab. Challenges in Translating Rubberized Mortar Properties to Concrete: Segregation and Shear Slump. *Construction Technologies and Architecture* 17: 43-50 (2025). https://doi.org/10.4028/p-1m7IXC
15. ASTM C150/C150M-22. Standard Specification for Portland Cement. *ASTM International, West Conshohocken, Pennsylvania United States* (2022). https://doi.org/10.1520/C0150_C0150M-22
16. ASTM C33-07. Standard Specification for Concrete Aggregates. *ASTM International, West Conshohocken, Pennsylvania United States* (2012). https://doi.org/10.1520/C0033-07
17. Y. Li, J. Mu, J. Hao, Y. Liu, X. Jiang, and X. Luo. Research on the particle characteristics of manufactured sands affecting the flow ability of fresh mortar. *Construction and Building Materials* 382: 131287 (2023). https://doi.org/10.1016/j.conbuildmat.2023.131287
18. ASTM C1240-20. Specification for Silica Fume Used in Cementitious Mixtures. *ASTM International, West Conshohocken, Pennsylvania United States* (2020). https://doi.org/10.1520/C1240-20
19. ASTM C618-19. Standard Specification for Coal Fly Ash and Raw or Calcined Natural Pozzolan for Use in Concrete. *ASTM International, West Conshohocken, Pennsylvania, United States* (2019). https://doi.org/10.1520/C0618-19
20. ASTM C1116/C1116M-10a. Specification for Fiber-Reinforced Concrete. *ASTM International, West Conshohocken, Pennsylvania United States* (2015). https://doi.org/10.1520/C1116_C1116M-10AR15
21. ASTM C494/C494M-19e1. Specification for Chemical Admixtures for Concrete. *ASTM International, West Conshohocken, Pennsylvania United States* (2019). https://doi.org/10.1520/C0494_C0494M-19E01
22. A. Khitab, M.T. Arshad, N. Hussain, K. Tariq, S.A. Ali, S.M.S. Kazmi, and M.J. Munir. Concrete reinforced with 0.1 vol% of different synthetic fibers. *Life Science Journal* 10(12s): 934-939 (2013). https://www.lifesciencesite.com/lsj/life1012s/152_22376life1012s_934_939.pdf
23. ASTM C305-20. Standard Practice for Mechanical Mixing of Hydraulic Cement Pastes and Mortars of Plastic Consistency. *ASTM International, West Conshohocken, Pennsylvania United States* (2022). https://doi.org/10.1520/C0305-20
24. ASTM C138/C138M-17a. Standard Test Method for Density (Unit Weight), Yield, and Air Content (Gravimetric) of Concrete. *ASTM International, West Conshohocken, Pennsylvania United States* (2023). https://doi.org/10.1520/C0138_C0138M-17A
25. ASTM C642-21. Test Method for Density, Absorption, and Voids in Hardened Concrete. *ASTM International, West Conshohocken, Pennsylvania United States* (2021). https://doi.org/10.1520/C0642-21
26. ASTM C1437-20. Test Method for Flow of Hydraulic Cement Mortar. *ASTM International, West Conshohocken, Pennsylvania United States* (2020). https://doi.org/10.1520/C1437-20
27. ASTM C109/C109M-20. Test Method for Compressive Strength of Hydraulic Cement Mortars. *ASTM International, West Conshohocken, Pennsylvania United States* (2020). https://doi.org/10.1520/C0109_C0109M-20
28. A. Benazzouk, O. Douzane, K. Mezreb, B. Laidoudi, and M. Quéneudec. Thermal conductivity of cement composites containing rubber waste particles: Experimental study and modelling. *Construction and Building Materials* 22: 573-579 (2008). https://doi.org/10.1016/j.conbuildmat.2006.11.011
29. A.J. Shaukat, H. Feng, A. Khitab, and A. Jan. Effect of Admixtures on Mechanical Properties of Cementitious Mortar. *Civil Engineering Journal* 6: 2175-2187(2020). https://doi.org/10.28991/cej-2020-03091610
30. M. Khan and M. Ali. Effect of super plasticizer on the properties of medium strength concrete prepared with coconut fiber. *Construction and Building Materials* 182: 703-715 (2018). https://doi.org/10.1016/j.conbuildmat.2018.06.150
31. H. Hosseinzadeh, A. M. Salehi, M. Mehraein, and G. Asadollahfardi. The effects of steel, polypropylene, and high-performance macro polypropylene fibers on mechanical properties and durability of high-strength concrete. *Construction and Building Materials* 386: 131589 (2023). https://doi.org/10.1016/j.conbuildmat.2023.131589
32. H.R. Pakravan and T. Ozbakkaloglu. Synthetic fibers for cementitious composites: A critical and in-depth review of recent advances. *Construction and Building Materials* 207: 491-518 (2019). https://doi.org/10.1016/j.conbuildmat.2019.02.078
33. U. Safeer, R.B.N. Khan, and A. Khitab. Enhancement of concrete performance by using compound mixture of waste pottery and red brick powders.

International Journal of Masonry Research and Innovation 10(2): 206-228 (2025). https://doi.org/10.1504/IJMRI.2025.144878

34. O.M. Olofinnade, A.N. Ede, J.M. Ndambuki, and G.O. Bamigboye. Structural properties of concrete containing ground waste clay brick powder as partial substitute for cement. *Materials Science Forum* 866: 63-67 (2016). https://doi.org/10.4028/www.scientific.net/MSF.866.63
35. H. Zhang, L. Zou, J. Ni, and Y. Wang. Study on the Polypropylene(PP) Fiber/Cement Mortar Workability. In: Composite Technologies for 2020. *Elsevier, USA* pp. 539-544 (2004). https://doi.org/10.1016/B978-1-85573-831-7.50093-6
36. M. Adjoudj, K. Ezziane, E.H. Kadri, T.T. Ngo, and A.Kaci. Evaluation of rheological parameters of mortar containing various amounts of mineral addition with polycarboxylate superplasticizer. *Construction and Building Materials* 70: 549-559 (2014). https://doi.org/10.1016/j.conbuildmat.2014.07.111
37. P.F.G. Banfill (Ed.). Rheology of Fresh Cement and Concrete. *Proceedings of the International Conference organized by the British Society of Rheology, University of Liverpool, UK, (March 16-29 1990), Taylor & Francis, Abingdon, UK* (1991). https://doi.org/10.1201/9781482288889
38. N.N. Gerges, C.A. Issa, and S.A. Fawaz. Rubber concrete: Mechanical and dynamical properties. *Case Studies in Construction Materials* 9: e00184 (2018). https://doi.org/10.1016/j.cscm.2018.e00184
39. L. Wang, Z. Yu, B. Liu, F. Zhao, S. Tang, and M. Jin. Effects of Fly Ash Dosage on Shrinkage, Crack Resistance and Fractal Characteristics of Face Slab Concrete. *Fractal And Fractional* 6(6): 335 (2022). https://doi.org/10.3390/fractalfract6060335
40. P. Vellaichany, S. Priyadharshini, R. Sarguna, and S. Selvan. Studies on Effect of Silica Fume on Workability and Strength of Concrete. *International Research Journal of Multidisciplinary Technovation* 1(6): 165-171 (2019). https://doi.org/10.34256/irjmtcon21
41. A. Karaşin and M. Doğruyol. An Experimental Study on Strength and Durability for Utilization of Fly Ash in Concrete Mix. *Advances In Materials Science and Engineering* 2014: 417514 (2014). https://doi.org/10.1155/2014/417514
42. Weather-Atlas.com. Climate and monthly weather forecast, Mirpur, Pakistan. *Weather-Atlas. Published online at*: https://www.weather-atlas.com/en/pakistan/mirpur-climate (Accessed: Feb 04, 2026).
43. D. Sathyan, K.B. Anand, K.M. Mini, and S. Aparna. Optimization of superplasticizer in portland pozzolana cement mortar and concrete. *IOP Conference Series: Materials Science and Engineering* 310: 012036 (2018). https://doi.org/10.1088/1757-899X/310/1/012036
44. A.M. Al-Ghaban, H.A. Jaber, and A.A. Shaher. Investigation of Addition Different Fibers on the Performance of Cement Mortar. *Engineering and Technology Journal* 36(A9): 957-965 (2018). https://www.uotechnology.edu.iq/tec_magaz/2018/Volume36/Engineering/No92018/Text/[3]Text.pdf
45. A.M. Neville (Ed.). Properties of Concrete. *Perason, Prentice Hall, India* (2012).
46. P.K. Mehta and P.J.M. Monteiro (Eds.). Concrete Microstructure, Properties and Materials. *McGraw Hill, New York, USA* (2017).
47. V.S. Jebadurai and D. Tensing. Mechanical Properties of Latex Mortar for Brick Masonry. *International Journal of Civil Engineering and Technology* 7(6): 400-407 (2016). https://iaeme.com/MasterAdmin/Journal_uploads/IJCIET/VOLUME_7_ISSUE_6/IJCIET_07_06_044.pdf
48. R. Siddique and T.R. Naik. Properties of concrete containing scrap-tire rubber – an overview. *Waste Management* 24(6): 563-569 (2004). https://doi.org/10.1016/j.wasman.2004.01.006
49. B.S. Thomas, R.C. Gupta, and V.J. Panicker. Recycling of waste tire rubber as aggregate in concrete: durability-related performance. *Journal of Cleaner Production* 112(1): 504-513 (2016). https://doi.org/10.1016/j.jclepro.2015.08.046
50. A. Asad, S. Iftikhar, and A. Khitab. Waste brick and marble powders as sustainable additives for improving slag-based concrete. *Journal of Building Engineering* 111: 113625 (2025). https://doi.org/10.1016/j.jobe.2025.113625
51. S.M.A. El-Gamal, F.M. Al-Nowaiser, and A.O. Al-Baity. Effect of superplasticizers on the hydration kinetic and mechanical properties of Portland cement pastes. *Journal of Advanced Research* 3(2): 119-124 (2012). https://doi.org/10.1016/j.jare.2011.05.008
52. F.R.C. Ribeiro, A.S. Ruviaro, P.R. de Matos, and A.P. Kirchheim. Impact of different superplasticizers on hydration, rheology, mechanical strength, and environmental evaluation of LC3 cements. *Case Studies in Construction Materials* 23: e05347 (2025). https://doi.org/10.1016/j.cscm.2025.e05347
53. S. Mohamed, H. Elemam, M.H. Seleem, and H.E.M. Sallam. Effect of fiber addition on strength and toughness of rubberized concretes. *Scientific Reports* 14: 4346 (2024). https://doi.org/10.1038/

s41598-024-54763-w

54. J. Wang, C. Zhao, Q. Li, G. Song, and Y. Hu. The synergistic effect of recycled steel fibers and rubber aggregates from waste tires on the basic properties, drying shrinkage, and pore structures of cement concrete. *Construction and Building Materials* 470: 140574 (2025). https://doi.org/10.1016/j.conbuildmat.2025.140574
55. X. Chen, G. Ge, Y. Zhou, S. Pan, and A. Ren. The effects of high-content rubber and steel fibers on the workability and mechanical properties of concrete. *Composites and Advanced Materials* 34: (2025). https://doi.org/10.1177/26349833251343228
56. T. Alexandru, B. Marinela, D. Laura, and B. Irina. Mechanical and Environmental Performances of Concrete Using Recycled Materials. *Procedia Manufacturing* 32: 253-258 (2019). https://doi.org/10.1016/j.promfg.2019.02.211
57. M. Haroon, R.B.N. Khan, and A. Khitab. Performance of concrete containing waste demolished concrete powder as a partial substitute for cement. *International Journal of Building Pathology and Adaptation* 43(4): 573-590 (2024). https://doi.org/10.1108/IJBPA-01-2024-0002
58. L.A. Le, G.D. Nguyen, H.H. Bui, A.H. Sheikh, and A. Kotousov. Incorporation of micro-cracking and fibre bridging mechanisms in constitutive modelling of fibre reinforced concrete. *Journal of the Mechanics and Physics of Solids* 133: 103732 (2019). https://doi.org/10.1016/j.jmps.2019.103732
59. A. Khitab, S. Ahmad, R.A. Khan, M.T. Arshad, W. Anwar, J. Tariq, A.S.R. Khan, R.B.N. Khan, A. Jalil, and Z. Tariq. Production of Biochar and Its Potential Application in Cementitious Composites. *Crystals* 11(5): 527 (2021). https://doi.org/10.3390/cryst11050527

Proceedings of the Pakistan Academy of Sciences: A Physical and Computational Sciences 63(2): 99-113 (2026)

ISSN (Print): 2518-4245; ISSN (Online): 2518-4253
http://doi.org/10.53560/PPASA(63-2)713

Pakistan Academy of Sciences

Research Article

Integrated in Silico Analyses Reveal Diterpenoids from *Erythrophleum fordii* as Potential Inhibitors of Anti-Apoptotic Targets in Ovarian Cancer

Hung Duc Nguyen*

Faculty of Biology, Thai Nguyen University of Education, Thai Nguyen, Vietnam

Abstract: Ovarian cancer remains a major clinical challenge, particularly in advanced-stage disease, where relapse and resistance to platinum-taxane chemotherapy continue to limit therapeutic efficacy. Because anti-apoptotic Bcl-2 family proteins contribute to chemoresistance, myeloid cell leukemia 1 (Mcl-1) represents a relevant molecular target. This study evaluated five cassane-type diterpenoids from *Erythrophleum fordii* (CPD1-CPD5), previously reported to inhibit A2780 ovarian cancer cell growth, against Mcl-1 (PDB: 6UD2) using molecular docking, molecular dynamics simulation, Molecular Mechanics Generalised Born Surface Area (MM/GBSA), and Density Functional Theory (DFT) analysis, with paclitaxel as a reference. Docking placed all compounds within the BH3-binding groove and identified CPD2 (erythrophlesin F) as the top-ranked diterpenoid, with a docking score of -9.63 kcal/mol and favorable interactions with Asn223, Arg263, and Thr266. Molecular dynamics analysis indicated stable pocket occupancy for CPD2 and paclitaxel, while hydrogen-bond monitoring suggested greater persistence of polar contacts for CPD2. MM/GBSA supported favorable binding for both ligands, although paclitaxel displayed a more favorable mean binding free energy under the applied protocol. DFT descriptors further differentiated both compounds, with CPD2 showing a larger HOMO-LUMO gap and lower electrophilicity. These findings support CPD2 as a promising Mcl-1-binding candidate that warrants experimental validation.

Keywords: Apoptosis, DFT, Diterpenoid, *Erythrophleum fordii*, Mcl-1, Molecular Modeling.

1. INTRODUCTION

Ovarian cancer remains among the most fatal malignancies of the female reproductive tract. Survival outcomes are especially poor in advanced disease, where the five-year survival rate often does not exceed 30%. Much of this clinical burden arises from delayed diagnosis. In nearly 70-80% of cases, detection occurs only after substantial progression has already taken place. Recurrence further aggravates prognosis, with relapse reported in approximately 70-90% of patients even after first-line treatment [1]. Standard therapy for epithelial ovarian cancer relies on cytoreductive surgery followed by platinum-taxane chemotherapy [2]. Even so, long-term disease control is frequently undermined by tumor recurrence and the emergence of acquired drug resistance. Reduced sensitivity to paclitaxel-based treatment, for example, has been associated with adaptive cellular changes that weaken apoptotic signaling during mitotic stress and thereby permit continued tumor cell survival under sustained therapeutic exposure [3].

Resistance to therapy is closely linked to failure of apoptotic activation. The Bcl-2 protein family occupies a central position in this process by regulating mitochondrial outer membrane permeabilization and the downstream caspase cascade, both of which are essential for intrinsic apoptosis. Anti-apoptotic members of this family sequester BH3-only pro-apoptotic factors, suppress BAX/BAK activation, and in doing so elevate the threshold required for mitochondria-dependent cell death [4, 5]. Among these regulators, myeloid cell leukemia 1 (Mcl-1) has emerged as a particularly important determinant of cancer cell survival [6]. Elevated Mcl-1 activity has been implicated

Received: March 2026; Revised: May 2026; Accepted: June 2026
* Corresponding Author: Hung Duc Nguyen <hungnd@tnue.edu.vn>

in the suppression of multiple death-promoting signals and in the maintenance of drug-tolerant phenotypes across a range of malignancies, including chemotherapy-resistant tumors. As a result, Mcl-1 inhibition has gained recognition as a promising strategy for restoring antitumor sensitivity, a view reinforced by continued advances in the development and clinical assessment of BH3-mimetic compounds [7].

Natural products continue to occupy a central role in anticancer drug discovery because of their chemical diversity and long-standing pharmacological relevance. More than 60% of approved anticancer agents originate directly or indirectly from natural sources [8]. Major groups such as alkaloids, terpenoids, polyphenols, and quinones arise from biosynthetic pathways refined through evolution, often yielding molecular architectures well suited for interaction with biological macromolecules [9]. Compared with many fully synthetic collections, such compounds frequently offer greater structural complexity and broader target-recognition potential. Diterpenoids are particularly noteworthy within this landscape. This class has repeatedly been reported to possess marked antitumor activity, often accompanied by relatively low toxicity, and includes compounds capable of exerting both cytotoxic and chemosensitizing effects in diverse experimental models. Interest in diterpenoids has also increased because of documented influences on signaling pathways and drug-transport mechanisms associated with multidrug resistance [10, 11].

Species of the genus *Erythrophleum* are recognized sources of cassane-type diterpenoids. Several constituents isolated from *Erythrophleum fordii* have shown promising anticancer activity in ovarian cancer models, including inhibition of A2780 cell proliferation [12]. These observations raise the possibility that *E. fordii* diterpenoids may contain chemotypes able to interact with proteins governing apoptosis. That possibility remains insufficiently explored at the molecular level. In particular, protein-pocket recognition and ligand-specific binding determinants have not yet been defined in detail through systematic structure-based computational analysis.

Recent progress in structure-guided in silico methods has provided an efficient framework for compound prioritization, especially in natural-product research. Molecular docking, molecular dynamics (MD) simulation, and end-point binding free-energy estimation such as MM/GBSA now form a widely used workflow for evaluating ligand-protein interactions. Docking offers an initial view of binding geometry, whereas MD simulation captures the temporal behavior of complexes under solvated conditions that better approximate physiological environments [13]. Existing structural data on Mcl-1 enables precise assessment of ligand accommodation within its binding site. This assessment involves confirmation of docking configurations through redocking procedures and examination of ligand-protein interaction durability in aqueous settings. Concurrently, density functional theory (DFT) yields perspectives on ligand electronic attributes. Through evaluation of frontier molecular orbitals alongside additional DFT-derived metrics, comparisons of reactivity features that affect binding dynamics become feasible [14].

This investigation employed a unified computational methodology to analyze five diterpenoids extracted from *Erythrophleum fordii* (CPD1-CPD5), previously demonstrated to inhibit A2780 cell growth, as prospective binders to the anti-apoptotic protein Mcl-1. The crystallographic model 6UD2 served as the protein representation, with paclitaxel incorporated as a benchmark for contrasting binding patterns in the identical site. Molecular dynamics computations occurred in GROMACS via the CHARMM36 force field, while free energy estimations for binding utilized gmx_MMPBSA. DFT analyses in ORCA determined energies of frontier orbitals and associated theoretical descriptors. This approach appraised the diterpenoids' capacity to interact with the Mcl-1 site and sustain complex integrity, integrating docking alignments, simulation-derived energy evaluations, and quantum mechanical property descriptions into one cohesive protocol.

2. MATERIALS AND METHODS

2.1. Data Collection

The list of diterpenoids possessing anti-cancer activity against the A2780 ovarian cancer cell line was collected in the previous study [12]. Because A2780 is an established ovarian cancer cell model,

these compounds were selected to maintain a disease-relevant link between the previously reported cytotoxic activity and the present Mcl-1-targeted computational analysis. For detail, the selected ligands, including erythrophlesin E (CPD1), erythrophlesin F (CPD2), erythrophlesin C (CPD3), erythrophlesin G (CPD4) and 6α-hydroxydinorerythrophlamide (CPD5), have molecular formulas of $C_{46}H_{63}NO_{12}$, $C_{42}H_{61}NO_{10}$, $C_{43}H_{63}NO_{10}$, $C_{44}H_{63}NO_{12}$, $C_{23}H_{35}NO_7$, respectively, with molecular weights of 797.4350, 739.4295, 753.4452, 797.4350, and 437.2414 g/mol. The Paclitaxel, possessing a molecular formula of $C_{47}H_{51}NO_{14}$ and a molecular weight of 853.3310 g/mol, was chosen as the positive control (Figure 1).

2.2. Molecular Docking Analysis

Three-dimensional structures of the selected ligands were prepared in PDB format with BIOVIA Discovery Studio Visualizer, including addition of polar hydrogen atoms, assignment of Gasteiger partial charges, and allowance for full torsional flexibility. The Mcl-1 receptor structure (PDB ID: 6UD2) was obtained from the RCSB Protein Data Bank [15]. Receptor preprocessing in BIOVIA Discovery Studio involved removing crystallographic water molecules to align with an AutoDock-based approach that does not explicitly represent interfacial waters. Molecular docking was performed in AutoDock Tools using a grid box of 60 points along the x, y, and z axes with a grid spacing of 0.375 Å, centered on the binding site at x = 7.033 Å, y = 8.581 Å, and z = 98.593 Å. The grid center coordinates were defined based on the position of the co-crystallized ligand in the PDB 6UD2 structure. Conformational sampling and pose optimization were conducted using the Lamarckian genetic algorithm to prioritize low-energy binding orientations with favorable intermolecular contacts. Following docking, the top-ranked pose by predicted binding strength was examined in Discovery Studio Client 2024 and compared with docking results for Paclitaxel on the same receptor to contextualize relative binding features.

2.3. Molecular Dynamics Simulations

Molecular dynamics simulations were performed for the optimal docked complex with the 6UD2 protein over 100 ns using GROMACS 2024.4 with the CHARMM36 force field [16]. The receptor structure was curated in Swiss-PdbViewer to restore missing atoms and residues before simulation setup [17]. Ligand parameters and topology files were generated with SwissParam [18]. The protein-ligand assemblies were immersed in a triclinic periodic cell containing SPC water molecules, and NaCl was introduced to a final concentration of 0.15 M in order to approximate physiological ionic conditions. Adoption of an explicit-solvent environment permitted dynamic reorganization of interfacial water molecules during the simulation. Prior to trajectory generation, each system underwent 50,000 steps of energy minimization to remove unfavorable contacts and achieve an electrostatically balanced state. Equilibration was subsequently carried out in two stages: a

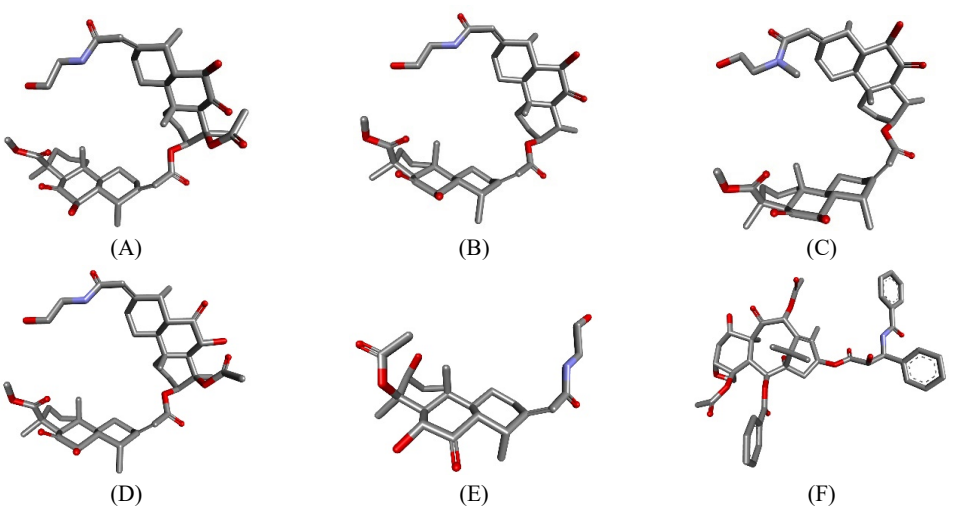

Fig. 1. 3D Structures of selected ligands. (A) CPD1, (B) CPD2, (C) CPD3, (D) CPD4, (E) CPD5, and (F) Paclitaxel.

200 ps NVT ensemble, followed by a 200 ps NPT ensemble, both maintained at 300 K and 1.0 bar. For each system, a single 100 ns production simulation was performed with a 2 fs integration step, and coordinates were saved at 10 ns intervals. Trajectory-derived parameters were analyzed in Grace, including root mean square deviation (RMSD), residue-wise root mean square fluctuation (RMSF), radius of gyration (Rg), number of hydrogen bonds (H-bonds), and solvent-accessible surface area (SASA). Conformational inspection and structural superposition were conducted in UCSF Chimera 1.13.3 to examine retention of the bound conformational state. Ligand poses extracted at 0 and 100 ns were overlaid within the binding site to evaluate the continuity of principal interaction patterns across the simulation period, with particular attention to hydrogen bonding, van der Waals contacts, and hydrophobic complementarity. Paclitaxel was used throughout as the reference ligand, with nomenclature retained consistently across all analyses.

2.4. Molecular Mechanics Generalised Born Surface Area (MM/GBSA) Analysis

Binding free energies for the CPD2-6UD2 and paclitaxel-6UD2 complexes were calculated with the gmx_MMPBSA protocol under the CHARMM36 force field [19]. Within this MM/GBSA framework, electrostatic solvation was represented by the generalized Born formalism under an implicit-solvent approximation, whereas the nonpolar contribution was obtained from solvent-accessible surface area-dependent terms. Energetic decomposition was performed from molecular dynamics trajectories using 125 evenly spaced snapshots collected every 80 ps across the 20-100 ns interval. Frame-averaged values were subsequently used to capture time-dependent variation in complex behavior and to compare relative binding favorability and stability under the applied simulation conditions [20].

2.5. Quantum Chemistry Computation Using the Density Functional Theory (DFT) Method

Geometry optimization of CPD2 and Paclitaxel was performed with the ORCA 6.1.0 quantum-chemistry suite. Starting conformations were built in Avogadro, and subsequent visualization together with molecular orbital inspection was carried out in IboView (v20211019) [21-24]. Density functional theory calculations were executed at the B3LYP/6-31G(d,p) level to obtain energetically minimized structures and an electronic-structure description suitable for reactivity assessment. This gas-phase B3LYP/6-31G(d,p) protocol was selected because it is commonly applied for geometry optimization and frontier molecular orbital analysis of natural-product-like compounds, enabling consistent comparison of electronic descriptors between CPD2 and paclitaxel. Based on the optimized geometries, frontier orbital energies (HOMO and LUMO) were obtained and used to derive the energy gap (ΔE) and related conceptual DFT descriptors, including chemical potential (μ), electronegativity (χ), global hardness (η), global softness (σ), and electrophilicity index (ω). These quantities were estimated under the Koopmans' theorem approximation to support the comparative interpretation of electronic characteristics and potential reactivity patterns of the investigated compounds [25, 26].

3. RESULTS AND DISCUSSION

3.1. Molecular Docking Analysis

Molecular docking constitutes a structure-guided approach for predicting ligand accommodation within a protein binding site and for prioritizing candidate complexes through scoring functions intended to approximate binding favorability [27]. Such scores, however, provide only a limited estimate because solvent effects, conformational adaptability of the receptor, and entropic contributions are represented in a simplified manner. For this reason, docking results are generally interpreted in conjunction with residue-level interaction patterns and, where possible, complemented by molecular dynamics simulation or binding free-energy refinement. In the present work, docking analysis was directed toward the anti-apoptotic protein Mcl-1 (PDB ID: 6UD2), a member of the BCL-2 family widely associated with apoptotic suppression and treatment resistance, and therefore regarded as a relevant target in contemporary anticancer research [28]. This target choice is relevant to ovarian cancer because impaired apoptotic signaling and resistance to platinum-taxane chemotherapy remain major barriers in ovarian cancer treatment, while the selected *E. fordii* diterpenoids were originally reported to inhibit A2780 ovarian cancer cell

growth [2, 3, 12]. The crystallographic entry 6UD2 provides an experimentally resolved Mcl-1 binding groove suitable for mapping ligand recognition features against a reference co-crystal environment. Before production docking, protocol validation is typically conducted by redocking the co-crystallized ligand and comparing the regenerated pose with the experimental conformation. This procedure yielded an RMSD of 0.5138 Å (Figure 2), indicating close reproduction of the pose. An RMSD cutoff of around 2 Å is widely used as a practical acceptance criterion for pose reproduction in benchmarking studies [29].

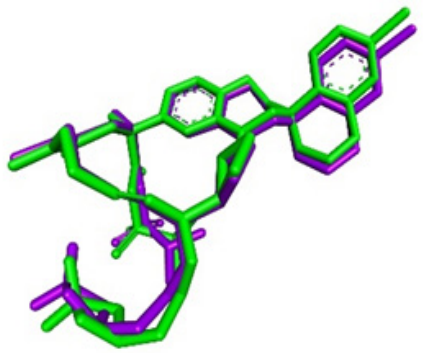

Fig. 2. Superimposition of the docked and native ligands for validation of the molecular docking protocol on protein 6UD2 (violet = native, green = docked).

After validation, candidate poses are ranked by docking energy and prioritized for interaction analysis within the Mcl-1 groove, focusing on non-covalent contacts such as hydrogen bonding, van der Waals complementarity, and hydrophobic packing, which collectively contribute to complex stabilization in BH3-like binding sites. Details of how the screened ligands interact with the 6UD2 binding cavity are summarized in Table 1, highlighting residues within the interaction zone and the dominant non-covalent interactions (hydrogen bonds, van der Waals, and hydrophobic interactions). Such interaction profiling is commonly used to rationalize docking poses and to prioritize candidates for downstream simulation or experimental evaluation.

Across the series, docking scores ranged from -7.39 to -9.63 kcal/mol, with CPD2 exhibiting the most favorable predicted affinity (-9.63 kcal/mol), followed by CPD3 (-9.28 kcal/mol) and CPD4 (-9.19 kcal/mol). CPD1 yielded a moderate affinity estimate (-8.80 kcal/mol), while CPD5 exhibited the poorest binding prediction among evaluated compounds (-8.17 kcal/mol). The comparator paclitaxel showed a less advantageous docking value (-7.39 kcal/mol) compared to chosen ligands,

Table 1. The interactions between the docked ligands and the protein 6UD2.

Docked ligands	Binding energy (kcal/mol)	Hydrogen bond interaction	Van der Waals interaction	Hydrophobic interaction
CPD1	-8.80	Gly262, Arg263, Leu267	Val220, Phe228, Leu235, Phe254, Asn260, Val265, Thr266, Gly271, Ile294	His224, Met231, Val249, Met250, Val253, Arg263, Phe270
CPD2	-9.63	Asn223, Arg263, Thr266	Val216, Val220, His224, Met231, Leu235, Phe254, Asn260, Val265, Gly271, Val274	Val249, Met250, Val253, Leu267, Phe270
CPD3	-9.28	His224, Val249, Arg263, Thr266	Val220, Asn223, Leu235, Leu246, Phe254, Val258, Asn260, Gly262, Val265, Gly271, Val274	Met231, Met250, Val253, Leu267, Phe270
CPD4	-9.19	His224, Arg263	Phe228, Met231, Leu235, Leu246, Val249, Met250, Thr266, Gly271, Val274, Leu290, Ile294	Ala227, Val253, Phe254, Leu267, Phe270
CPD5	-8.17	Arg263, Thr266	Val220, His224, Leu235, Leu246, Val249, Met250, Leu267, Val274	Met231, Val253, Phe254, Arg263, Phe270
Paclitaxel	-7.39	Arg263	Ala227, Phe228, Met231, Phe254, Gly262, Thr266, Phe270, Gly271, Leu290	His224, Leu246, Met250, Val253, Arg263, Leu267, Ile294

suggesting diminished anticipated stability in the identical site according to the employed metric. Docking evaluations usually involve relative assessments rather than definitive measures, where greater negativity correlates with enhanced conformational security based on observational scoring principles [30].

CPD2 achieved the strongest docking score and maintained active-site engagement with His224, Met231, Val249, Met250, Val253, Arg263, Leu267, and Phe270. Hydrogen-bonding interactions were identified with Asn223, Arg263, and Thr266, establishing a set of directional polar contacts across the entrance and central segment of the binding groove. Van der Waals complementarity extended beyond these residues to include Val216, Val220, His224, Met231, Leu235, Phe254, Asn260, Val265, Gly271, and Val274, indicating broad steric accommodation within the cavity (Figure 3(A)) [31]. Nonpolar contacts were distributed mainly around Val249, Met250, Val253, Leu267, and Phe270, a pattern consistent with stabilization through burial of hydrophobic surface area in the ligand-bound state. Taken together, the coexistence of defined polar anchoring at Asn223, Arg263 and Thr266 and compact hydrophobic packing across the Val249-Phe270 region provides a plausible structural basis for the superior docking score observed for this ligand relative to the remaining compounds [32]. The binding region in 6UD2 corresponds to the canonical BH3-recognition groove of Mcl-1, which is formed by a predominantly hydrophobic cleft responsible for accommodating the nonpolar face of BH3 helices and BH3-mimetic ligands. In the predicted binding mode, CPD2 extends along this groove and engages an extended hydrophobic surface defined by Val249, Met250, Val253, Leu267, and Phe270, consistent with occupation of the subpockets that govern BH3 recognition. Polar interactions involving Asn223, Arg263, and Thr266 appear to further constrain ligand orientation and support positional registration within the groove [33].

CPD1, CPD3, CPD4, and CPD5 occupied a broadly similar region of the Mcl-1 binding groove, with recurring contacts involving His224, Met231, Val249, Met250, Val253, Arg263, Leu267, and Phe270. These compounds shared a mixed polar-hydrophobic interaction pattern, although their docking scores and contact geometries varied. CPD3 and CPD4 showed relatively favorable docking scores and broad contact coverage, whereas CPD1 and CPD5 displayed less favorable predicted binding, possibly reflecting less optimal cavity filling or weaker polar anchoring. These observations suggest that the diterpenoid series generally fits within the same recognition region, but with ligand-specific differences in contact balance and shape complementarity.

Paclitaxel, used as a control ligand, engaged an expanded active-site set (His224, Ala227, Phe228, Met231, Met250, Val253, Arg263, Leu267, Phe270, Leu290). Hydrogen bonding was assigned to Arg263, while van der Waals interactions involved Ala227, Phe228, Met231, Phe254, Gly262, Thr266, Phe270, Gly271, and Leu290. Hydrophobic contacts were attributed to His224, Leu246, Met250, Val253, Arg263, Leu267, and Ile294 (Figure 3(B)). Despite the established clinical role of paclitaxel as a microtubule-directed chemotherapeutic agent, the lower docking score observed in this binding site suggests less favorable predicted accommodation within the present structural model. This difference in score supports preferential consideration of the CPD series for subsequent analysis in the 6UD2 pocket [34].

From a physicochemical standpoint, the interaction profile follows established determinants of protein-ligand recognition. Hydrogen bonds contribute spatial directionality and may constrain ligand orientation when donor-acceptor geometry is favorable, as reflected by contacts involving Asn223, Thr266, His224, and Arg263. By contrast, van der Waals interactions primarily reflect steric complementarity across the contour of the cavity. The hydrophobic cluster formed around Val249, Met250, Val253, Leu267, and Phe270 is likewise consistent with stabilization driven by nonpolar surface burial and interfacial water reorganization, particularly within grooves enriched in aliphatic and aromatic side chains. In combination, these non-covalent contributions provide a reasonable structural explanation for the docking hierarchy obtained in the present analysis [35, 36].

When docking score and interaction breadth are considered together, CPD2 emerges as the most compelling candidate for subsequent molecular dynamics evaluation. This prioritization is supported by the most favorable predicted binding

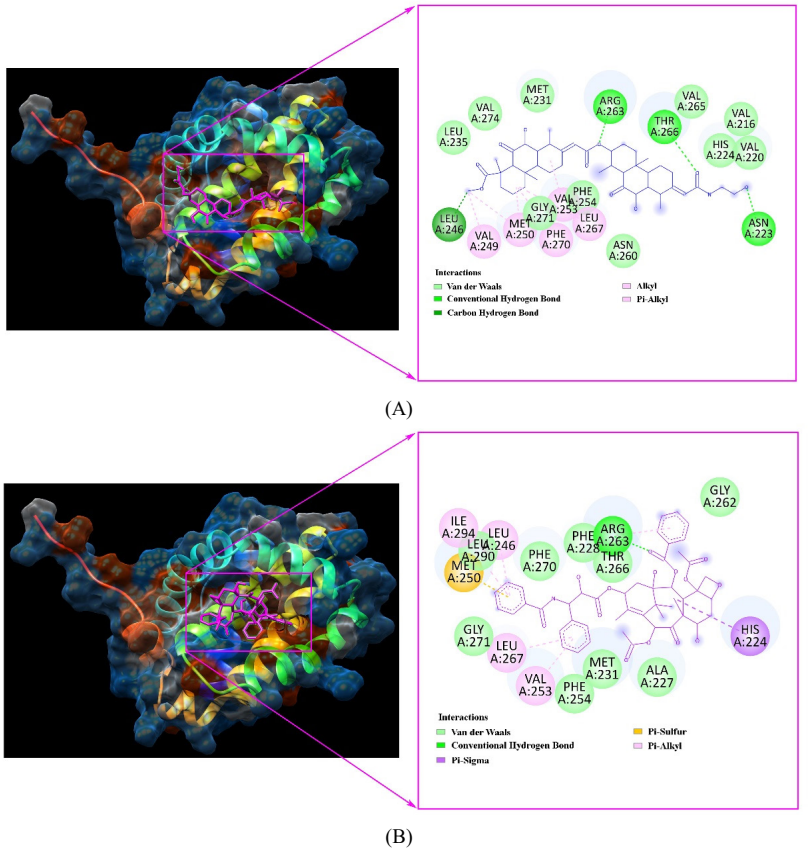

Fig. 3. Molecular docking model and 2D interaction diagram of CPD2 (A) and Paclitaxel (B) with 6UD2 protein.

energy (-9.63 kcal/mol), directional polar contacts with Asn223, Arg263, and Thr266, and extensive packing interactions spanning residues from Val216 to Val274, together with dense hydrophobic complementarity across the Val249-Phe270 region. CPD3 and CPD4 also exhibited favorable predicted recognition and broad residue engagement, indicating potential value as comparative systems in simulation studies or future structure-activity analysis. The 6UD2 structure represents human Mcl-1 in complex with an inhibitor, reinforcing the biological relevance of this pocket in apoptosis regulation and anticancer-target discovery.

3.2. Molecular Dynamics Simulations

Molecular dynamics (MD) simulations in drug design model the physical, time-dependent movements of atoms in biological systems to simulate interactions between drugs and targets. By accounting for molecular flexibility, MD enhances drug discovery by predicting binding affinities, optimizing lead compounds, identifying druggable sites, and revealing conformational changes, often refining results from docking studies [37]. In the present trajectories (100 ns), structural deviation, local flexibility, compactness, hydrogen-bond persistence, and solvent exposure were assessed for the CPD2-6UD2 and Paclitaxel-6UD2 complexes using root mean square deviation (RMSD), root mean square fluctuation (RMSF), radius of gyration (Rg), number of hydrogen bonds (H-bonds), and solvent-accessible surface area (SASA). Such descriptors are commonly used as complementary indicators of equilibration, residue-level mobility, global packing, and ligand-receptor interaction support in molecular dynamics-based screening approaches. The receptor model 6UD2 corresponds to an anti-apoptotic Mcl-1 co-crystal structure, aligning the simulations with an established apoptosis-evasion target relevant to therapeutic resistance in cancer biology. Accordingly, descriptors such as RMSD, RMSF, Rg, H-bonds, and SASA are routinely interpreted as complementary indicators of equilibration, local mobility, global compactness, and interaction continuity in protein-ligand systems. Consequently, the total energy and potential energy values for the

CPD2-6UD2 complex were found to be -362,971 kJ/mol and -449,240 kJ/mol, respectively. For the Paclitaxel-6UD2 complex, the total and potential energy values were -361,680 kJ/mol and -447,919 kJ/mol, respectively. The simulation system maintained equilibrium at 300 K.

The RMSD measures the average structural displacement relative to a reference conformation and is routinely used to assess trajectory convergence and global stability in biomolecular simulations. In the CPD2-6UD2 complex, RMSD values remained within 0.093-0.340 nm across 100 ns. The Paclitaxel-6UD2 complex showed a narrower distribution of 0.096-0.329 nm (Figure 4(A)). Both trajectories, therefore, occupied a low-RMSD regime (<0.35 nm), consistent with preserved overall fold during the simulation window. Transient excursions were visible but did not dominate the trajectories [37].

The RMSF was evaluated for Asp172-Gly326, covering the docking-defined recognition corridor and key residues such as His224, Ala227, Phe228, Met231, Val249-Val253, Arg263, Thr266, Leu267, Phe270, and Val274. In this region, both complexes show generally low fluctuations, with RMSF values mostly below 0.10 nm, consistent with a relatively stable local structure. Compared with Paclitaxel-6UD2, the CPD2-6UD2 complex displays slightly higher mobility across several subregions, particularly around Gly192-Met199, Arg201, and parts of the 230-250 segment, including the vicinity of Met231 and Val249-Val253 (Figure 4(B)). By contrast, residues forming the main recognition corridor remain comparatively restrained in both systems. The strongest increase in flexibility is confined to the C-terminal end, especially Glu322-Gly326, where both profiles rise sharply. Overall, the RMSF pattern indicates a stable binding region in both complexes, with Paclitaxel associated with marginally lower residue-level motion than CPD2.

The Rg reports mass-weighted spatial dispersion around the center of mass and is frequently interpreted as a compactness proxy during conformational sampling. Rg values for CPD2-6UD2 ranged from 1.455 to 1.543 nm. Paclitaxel-6UD2 ranged from 1.469-1.540 nm (Figure 4(C)). The overlapping Rg envelopes indicate comparable global compactness for both complexes, with no evidence of sustained expansion during 100 ns.

Hydrogen bonding contributes directionality and specificity in intermolecular recognition; in trajectories, hydrogen-bond counts are commonly monitored as a persistence descriptor rather than a sole affinity surrogate. In the CPD2-6UD2 system, the H-bond count fluctuated between 0 and 3, with frequent occupancy of 1-2 bonds and intermittent appearances of 3 bonds, particularly near the late portion of the trajectory. Digitized counts from the plot corresponded to proportions of approximately 33.7% (0 bonds), 33.2% (1 bond), 26.2% (2 bonds), and 6.9% (3 bonds) across the sampled frames. Paclitaxel-6UD2 fluctuated between 0 and 2 H-bonds; digitized proportions were approximately 81.2% (0 bonds), 14.3% (1 bond), and 4.5% (2 bonds) (Figure 4(D)). Based on these distributions, the estimated average H-bond number was approximately 1.06 bonds per frame for CPD2-6UD2, compared with 0.23 bonds per frame for paclitaxel-6UD2. This pattern supports higher hydrogen-bond persistence for CPD2 relative to Paclitaxel during the 100 ns window, consistent with docking assignments that placed Asn223/Arg263/Thr266 as principal polar anchors for CPD2 [15]. The higher average H-bond occupancy indicates more persistent polar stabilization of CPD2 within the Mcl-1 binding groove, thereby supporting its trajectory-level binding stability.

SASA tracks solvent exposure and can reflect breathing motions, ligand-induced burial, or changes in surface hydration; in practice, SASA complements RMSD and Rg by describing solvent-protein coupling. Over 100 ns, SASA values for CPD2-6UD2 spanned 88.30-101.03 nm^2. Paclitaxel-6UD2 spanned 91.70-98.69 nm^2 (Figure 4(E)). The CPD2 complex, therefore, showed a broader SASA dispersion, whereas Paclitaxel displayed a tighter envelope; however, both systems remained within a limited SASA band, consistent with the absence of major solvent-exposure transitions [38].

Across RMSD, RMSF (Asp172-Gly326), and Rg, both complexes preserved low-amplitude structural variability, indicating stable accommodation of each ligand in the crystallographic 6UD2 pocket. Hydrogen-bond monitoring differentiated the systems: CPD2 showed higher bond persistence and higher maximal occupancy (0-3) than Paclitaxel (0-2), aligning with docking-inferred polar contacts near Asn223, Arg263, and Thr266, and extensive hydrophobic packing around

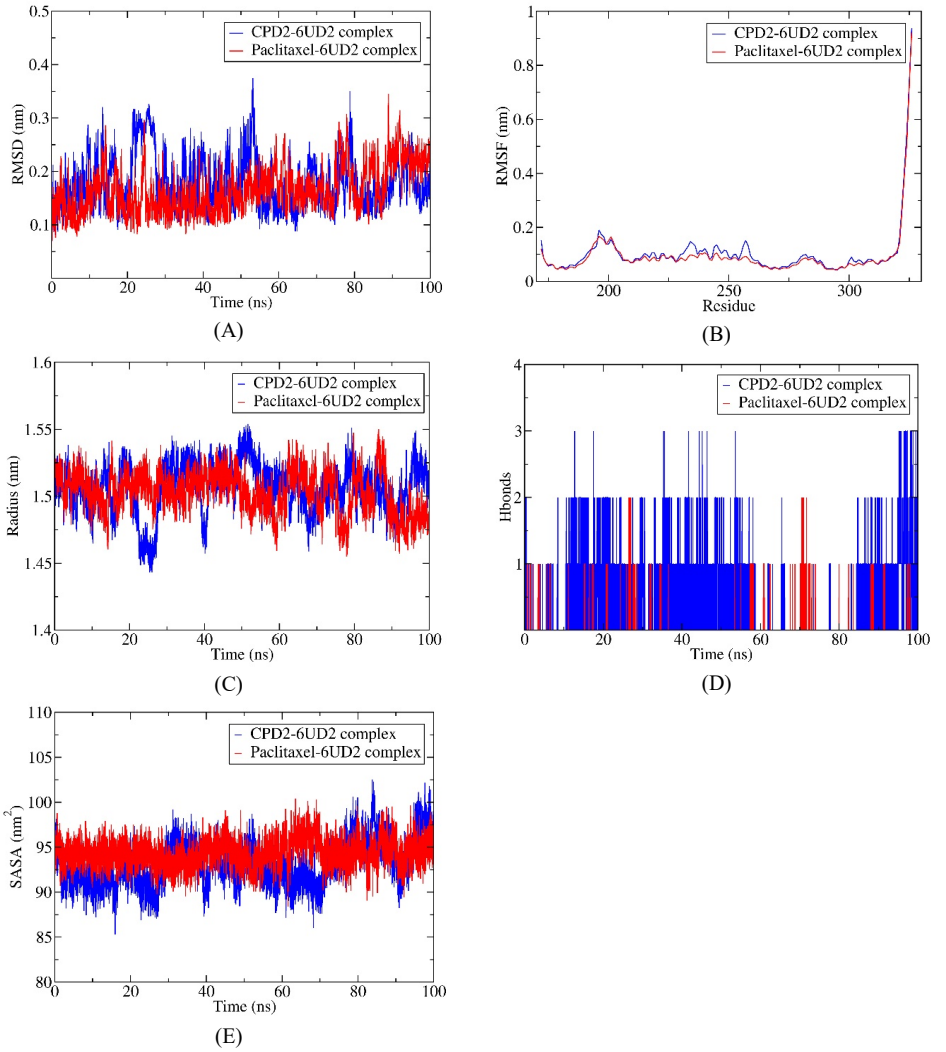

Fig. 4. Results of MD simulations for the bindings of CPD2 (blue) and Paclitaxel (red) with 6UD2 protein. (A) RMSD, (B) RMSF, (C) Rg, (D) Hbonds, and (E) SASA.

Val249, Met250, Val253, Leu267, and Phe270. SASA remained bound for both complexes, with CPD2 showing lower mean SASA but larger fluctuations than Paclitaxel, suggesting modest differences in solvent-exposure dynamics rather than large-scale conformational rearrangement.

3.3. Free Binding Energy (MM/GBSA) Analysis

Molecular Mechanics-Generalized Born Surface Area (MM/GBSA) has emerged as a crucial computational technique in modern drug discovery and natural product research, providing an efficient, accurate way to estimate binding free energies between macromolecules and small-molecule ligands. It bridges the gap between fast, less-accurate molecular docking scoring functions and slower, high-accuracy alchemical free energy methods [39]. Table 2 presents the MM/GBSA binding free-energy components (ΔVDWAALS, ΔEEL, ΔEGB, ΔESURF, ΔGGAS, ΔGSOLV) and the corresponding total binding free energy (ΔTOTAL) for the CPD2-6UD2 and Paclitaxel-6UD2 complexes, with mean values and standard deviations reported.

Both complexes show negative mean ΔTOTAL values, supporting a favorable association under the MM/GBSA decomposition used here. Paclitaxel-6UD2 yields ΔTOTAL = -35.77 ± 3.51 kcal/mol, whereas CPD2-6UD2 gives ΔTOTAL = -31.12 ± 4.00 kcal/mol. The mean difference is 4.65 kcal/mol in favor of Paclitaxel, indicating stronger predicted binding under the same computational protocol and sampling. A stronger gas-phase contribution primarily drives the more favorable

Table 2. Free energy of binding obtained using MM/GBSA calculations.

Energy Component	Average (kcal/mol)		Standard Deviation	
	CPD2-6UD2	Paclitaxel-6UD2	CPD2-6UD2	Paclitaxel-6UD2
ΔVDWAΔALS	-38.49	-50.29	4.17	3.71
ΔEEL	-10.55	-6.07	7.96	5.74
ΔEGB	22.72	27.42	7.46	6.20
ΔESURF	-4.79	-6.83	0.55	0.45
ΔGGAS	-49.05	-56.36	9.89	6.82
ΔGSOLV	17.93	20.59	7.08	6.10
ΔTOTAL	**-31.12**	**-35.77**	**4.00**	**3.51**

ΔTOTAL of Paclitaxel. ΔGGAS equals -56.36 ± 6.82 kcal/mol for Paclitaxel-6UD2 versus -49.05 ± 9.89 kcal/mol for CPD2-6UD2, a 7.31 kcal/mol advantage for Paclitaxel. Decomposition indicates that this advantage is dominated by dispersion/packing: ΔVDWAALS = -50.29 ± 3.71 kcal/mol (Paclitaxel) compared with -38.49 ± 4.17 kcal/mol (CPD2), i.e., 11.80 kcal/mol of van der Waals stabilization in favor of Paclitaxel. Such behavior is consistent with MM/GBSA practice, in which van der Waals terms often capture cavity complementarity and hydrophobic packing. Electrostatics partially compensates for the van der Waals difference. The Coulombic term ΔEEL is more favorable for CPD2-6UD2 (-10.55 ± 7.96 kcal/mol) than for Paclitaxel-6UD2 (-6.07 ± 5.74 kcal/mol), producing a 4.48 kcal/mol electrostatic advantage for CPD2. The net ΔGGAS ranking nevertheless remains Paclitaxel-favored because the magnitude of the van der Waals difference exceeds the opposing electrostatic shift [40].

Implicit-solvent contributions oppose binding for both ligands (positive ΔGSOLV), consistent with desolvation penalties in GBSA-type models. ΔGSOLV equals 20.59 ± 6.10 kcal/mol for Paclitaxel-6UD2 and 17.93 ± 7.08 kcal/mol for CPD2-6UD2, giving CPD2 a 2.66 kcal/mol lower solvation penalty. This difference arises mainly from the polar GB term: ΔEGB = 27.42 ± 6.20 kcal/mol (Paclitaxel) versus 22.72 ± 7.46 kcal/mol (CPD2), i.e., 4.70 kcal/mol lower polar desolvation for CPD2. The nonpolar surface term favored both complexes, with a modest advantage observed for paclitaxel. ΔESURF was calculated as -6.83 ± 0.45 kcal/mol for the paclitaxel-6UD2 complex and -4.79 ± 0.55 kcal/mol for CPD2-6UD2, corresponding to a 2.04 kcal/mol difference in favor of paclitaxel for the nonpolar solvation component. The solvation profile therefore reflected a differentiated energetic balance: CPD2 showed a lower penalty from the polar contribution, whereas paclitaxel displayed more favorable nonpolar surface energetics. The associated standard deviations indicated moderate variation across the sampled conformational ensemble, a pattern commonly observed in end-point free-energy approaches. Variability for ΔTOTAL remained relatively restricted, with standard deviations of 4.00 kcal/mol for CPD2-6UD2 and 3.51 kcal/mol for paclitaxel-6UD2. Greater fluctuation was evident for ΔGGAS (9.89 and 6.82 kcal/mol, respectively) and for the polar solvation term ΔEGB (7.46 and 6.20 kcal/mol, respectively), in agreement with the recognized sensitivity of MM/GBSA energy components to conformational microstates and dielectric representation.

Within the present MM/GBSA framework, the paclitaxel-6UD2 complex yielded the more favorable average binding free-energy estimate (-35.77 ± 3.51 kcal/mol) relative to CPD2-6UD2 (-31.12 ± 4.00 kcal/mol). This difference was driven primarily by a stronger van der Waals contribution for paclitaxel (-50.29 versus -38.49 kcal/mol), although part of that advantage was counterbalanced by more favorable electrostatic interaction energy and a lower polar solvation penalty in the CPD2 complex (ΔEEL, -10.55 versus -6.07 kcal/mol; ΔEGB, 22.72 versus 27.42 kcal/mol). Such a component distribution is consistent with the general behavior of MM/GBSA analyses, in which packing-related terms frequently dominate ΔGGAS, whereas implicit-solvent contributions influence the final rank ordering. Accordingly, interpretation remains most reliable in a comparative

sense within a uniform computational protocol. Although paclitaxel showed a more favorable MM/GBSA value, CPD2 was still prioritized because its selection was based on the integrated docking-MD-DFT assessment rather than MM/GBSA alone. In particular, CPD2 exhibited the best docking score among the diterpenoids, stable binding-site occupancy during MD simulation, and more persistent hydrogen-bond interactions, supporting its relevance as the lead *E. fordii* diterpenoid scaffold for further investigation.

3.4. Quantum Chemistry Computation Using the DFT Method

Density functional theory (DFT) represents an efficient and powerful computational tool for analyzing the electronic properties of isolated molecules and drug delivery systems, offering superior accuracy compared to molecular mechanics (MM) for studying reaction mechanisms, binding interactions, and enzyme inhibition [41]. Within conceptual DFT frameworks, the highest occupied molecular orbital (EHOMO) is linked to electron donation tendencies, while the lowest unoccupied molecular orbital (ELUMO) relates to electron acceptance. The HOMO-LUMO gap (ΔE) is commonly associated with electronic reactivity, where a smaller gap suggests increased polarizability and more favorable charge redistribution. Table 3 presents DFT-derived quantum descriptors for CPD2 and paclitaxel, including frontier orbital energies (EHOMO and ELUMO), the HOMO-LUMO gap (ΔE), and global reactivity indices (μ, χ, η, σ, and ω).

CPD2 exhibited an EHOMO of -9.6064 eV, while paclitaxel showed -8.6942 eV, indicating a higher electron donation propensity for paclitaxel. Regarding electron acceptance, CPD2 presented ELUMO = 3.3664 eV, and paclitaxel exhibited ELUMO = 2.1568 eV, with paclitaxel's lower LUMO suggesting a more accessible acceptor orbital [42]. The HOMO-LUMO gap for CPD2 was larger (ΔE = 12.9728 eV) compared to paclitaxel (ΔE = 10.8510 eV), reflecting a more rigid electronic structure for CPD2 and greater electronic flexibility for paclitaxel (Figure 5) [43].

The chemical potential (μ) for CPD2 was -3.1200 eV, while for paclitaxel, it was -3.2687 eV, implying a stronger thermodynamic tendency for electron stabilization in paclitaxel. Electronegativity (χ), treated as the negative of μ, also reflected this trend, with paclitaxel exhibiting a higher value (3.2687 eV vs. 3.1200 eV for CPD2) [44]. Chemical hardness (η) was 6.4864 eV for CPD2 and 5.4255 eV for paclitaxel, indicating that CPD2 is electronically stiffer, while paclitaxel is more electronically adaptable. The inverse parameter, softness (σ), was 0.1542 eV^{-1} for CPD2 and 0.1843 eV^{-1} for paclitaxel, with paclitaxel showing higher softness, suggesting more flexibility in response to external perturbation. The electrophilicity index (ω) was higher for paclitaxel (0.9846 eV) compared to CPD2 (0.7504 eV), indicating a stronger electrophilic character for paclitaxel under this conceptual framework [45]. These results highlight CPD2's more stable electronic profile, marked by a deeper HOMO, a higher LUMO, and a larger ΔE, compared to paclitaxel, which is characterized by a smaller ΔE, a higher HOMO energy, and greater electronic responsiveness.

Taken together, the integrated computational approach positions CPD2 as a promising Mcl-1-binding scaffold, offering stable binding and consistent interaction persistence. Although paclitaxel showed a more favorable MM/GBSA binding free energy, CPD2 remains the lead diterpenoid candidate because it exhibited the strongest docking score among the screened compounds, stable binding-site occupancy during MD simulation, and greater hydrogen-bond

Table 3. Quantum descriptors of CPD2 and Paclitaxel.

Molecule	EHOMO (eV)	ELUMO (eV)	ΔE (eV)	μ (eV)	χ (eV)	η (eV)	σ (eV^{-1})	ω (eV)
CPD2	-9.6064	3.3664	12.9728	-3.1200	3.1200	6.4864	0.1542	0.7504
Paclitaxel	-8.6942	2.1568	10.8510	-3.2687	3.2687	5.4255	0.1843	0.9846

EHOMO (eV): highest occupied molecular orbitals; ELUMO (eV): lowest unoccupied molecular orbitals; ΔE (eV): energy gap; μ (eV): chemical potential; χ (eV): electronegativity; η (eV): hardness; σ (eV^{-1}): softness; ω (eV): electrophilicity index.

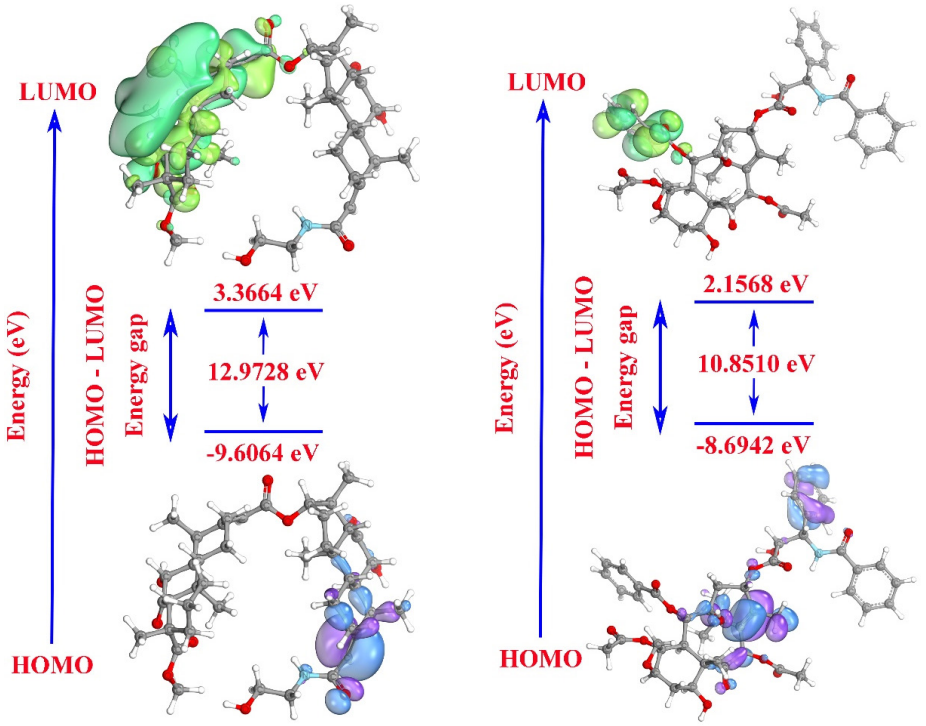

(A) (B)

Fig. 5. HOMO and LUMO surface diagrams of CPD2 (A) and Paclitaxel (B).

persistence within the Mcl-1 groove. In the context of ovarian cancer, these findings suggest that CPD2 may provide a useful starting scaffold for exploring apoptosis-related therapeutic strategies, particularly because the compounds were selected from *E. fordii* with reported activity against A2780 ovarian cancer cells. However, experimental validation is necessary to confirm Mcl-1 inhibition and establish biological relevance in ovarian cancer models. The lack of in vitro and in vivo validation remains a significant limitation, and future work should focus on biochemical binding assays, apoptosis assays in ovarian cancer cell lines, and early-stage ADMET profiling. Additionally, further optimization of the structure to enhance packing interactions while maintaining polar anchoring, along with an assessment of off-target interactions within the BCL-2 family, would be crucial for evaluating the potential therapeutic development of CPD2.

4. CONCLUSIONS

This investigation presents a comprehensive computational analysis of diterpenoids derived from *E. fordii* as potential inhibitors of Mcl-1 (PDB ID: 6UD2), a protein associated with apoptosis resistance in ovarian cancer. Molecular docking simulations indicated favorable accommodation of the diterpenoid series within the canonical binding groove of Mcl-1, with CPD2 emerging as the most promising candidate. CPD2 exhibited a more favorable docking score than paclitaxel (-9.63 kcal/mol vs. -7.39 kcal/mol) and demonstrated a balanced interaction profile, characterized by directional polar anchors (Asn223, Arg263, Thr266) and nonpolar packing (Val249, Met250, Val253, Leu267, Phe270). Molecular dynamics simulations over 100 ns supported the stability of CPD2's binding mode, with both complexes remaining in low-deviation regimes (mean RMSD 0.192 ± 0.053 nm for CPD2-6UD2 and 0.172 ± 0.038 nm for paclitaxel-6UD2), showing similar compactness (Rg of 1.51 nm). CPD2 maintained a more persistent hydrogen-bond network compared to paclitaxel, which further supports its strong interaction stability. MM/GBSA analysis confirmed the energetic favorability of both compounds, with paclitaxel displaying stronger van der Waals stabilization (-50.29 kcal/mol vs. -38.49 kcal/mol), while CPD2 showed stronger electrostatic contributions and reduced polar solvation penalties. DFT calculations highlighted paclitaxel's greater electronic adaptability (smaller ΔE and higher ω), whereas CPD2 exhibited a more rigid electronic

structure (larger ΔE and lower ω), indicating distinct electronic profiles for each compound.

5. ETHICAL STATEMENT

Ethical approval is not required, as this work does not include any studies involving human or animal subjects.

6. CONFLICT OF INTEREST

The author declares that there is no conflict of interest.

7. FUNDING

No funding was received to conduct this research.

8. AUTHORSHIP CONTRIBUTION

Hung Duc Nguyen: the sole responsibility for the conception of the study, presented results, and manuscript preparation. All data were generated in-house and that no paper mill was used. All results were interpreted solely by the author; Grammarly and Google Translate were used for English language refinement.

9. REFERENCES

1. M. Arcieri, V. Tius, S. Filippin, G. Aletti, D. Lorusso, A. Fagotti, J. Sehouli, I. Zapardiel, P. De Iaco, P. Scollo, and *et al*. Management of patients with epithelial ovarian cancer: A systematic comparison of international guidelines from scientific societies (AIOM-BGCS-ESGO-ESMO-JGSO-NCCN-NICE). *Cancers* 17(24): 3915 (2025). https://doi.org/10.3390/cancers17243915
2. M. Nunes, C. Bartosch, M.H. Abreu, A. Richardson, R. Almeida, and S. Ricardo. Deciphering the molecular mechanisms behind drug resistance in ovarian cancer to unlock efficient treatment options. *Cells* 13(9): 786 (2024). https://doi.org/10.3390/cells13090786
3. R. Goel, P. Upadhyay, R. Garg, D. Gulwani, and T.D. Singh. Overcoming paclitaxel resistance in ovarian cancer cells using DN200434, an inverse agonist of estrogen-related receptor gamma (ERRγ). *Biochemical and Biophysical Research Communications* 778: 152351 (2025). https://doi.org/10.1016/j.bbrc.2025.152351
4. J. Kale, E.J. Osterlund, and D.W. Andrews. BCL-2 family proteins: Changing partners in the dance towards death. *Cell Death & Differentiation* 25(1): 65-80 (2018). https://doi.org/10.1038/cdd.2017.186
5. I. Jaya, F. Safriadi, I. Wijaya, P. Pitaloka, E. Afifah, F.S. Medina, and M.H. Bashari. Role of Bcl-2 family anti-apoptosis inhibition in overcoming therapeutic resistance in prostate cancer: A systematic review. *Critical Reviews in Oncology/Hematology* 215: 104895 (2025). https://doi.org/10.1016/j.critrevonc.2025.104895
6. M. Mohiuddin. Targeting MCL-1 to overcome therapeutic resistance and improve cancer mortality. *Health Science Reports* 8(10): e71390 (2025). https://doi.org/10.1002/hsr2.71390
7. W. Xiang, C.Y. Yang, and L. Bai. MCL-1 inhibition in cancer treatment. *OncoTargets and therapy* 11: 7301-7314 (2018). https://doi.org/10.2147/OTT.S146228
8. S.T. Asma, U. Acaroz, K. Imre, A. Morar, S.R. Shah, S.Z. Hussain, D. Arslan-Acaroz, H. Demirbas, Z. Hajrulai-Musliu, F.R. Istanbullugil, A. Soleimanzadeh, D. Morozov, K. Zhu, V. Herman, A. Ayad, C. Athanassiou, and S. Ince. Natural products/bioactive compounds as a source of anticancer drugs. *Cancers* 14(24): 6203 (2022). https://doi.org/10.3390/cancers14246203
9. A. Naeem, P. Hu, M. Yang, J. Zhang, Y. Liu, W. Zhu, and Q. Zheng. Natural Products as Anticancer Agents: Current Status and Future Perspectives. *Molecules* 27(23): 8367 (2022). https://doi.org/10.3390/molecules27238367
10. Z. Deng, I. Bakunina, H. Yu, J. Han, A. Dömling, M.J.U. Ferreira, and J. Zhang. Research progress on natural diterpenoids in reversing multidrug resistance. *Frontiers in Pharmacology* 13: 815603 (2022). https://doi.org/10.3389/fphar.2022.815603
11. A. Sharmila, P. Bhadra, C. Kishore, C.I. Selvaraj, J. Kavalakatt, and A. Bishayee. Nanoformulated Terpenoids in cancer: A review of therapeutic applications, mechanisms, and challenges. *Cancers* 17(18): 3013 (2025). https://doi.org/10.3390/cancers17183013
12. D. Du, J. Qu, J.M. Wang, S.S. Yu, X.G. Chen, S. Xu, S.G. Ma, Y. Li, G.Z. Ding, and L. Fang. Cytotoxic cassaine diterpenoid-diterpenoid amide dimers and diterpenoid amides from the leaves of *Erythrophleum fordii*. *Phytochemistry* 71(14): 1749-1755 (2010). https://doi.org/10.1016/j.phytochem.2010.07.004
13. A. Vidal-Limon, J.E. Aguilar-Toalá, and A.M. Liceaga, Integration of molecular docking analysis and molecular dynamics simulations for studying food proteins and bioactive peptides. *Journal of Agricultural and Food Chemistry* 70(4): 934-943 (2022). https://doi.org/10.1021/acs.jafc.1c06110
14. S. Liu. The evolving quest for chemical understanding

in the quantum age. *Journal of Chemical Theory and Computation* 21(20): 10068-10079 (2025). https://doi.org/10.1021/acs.jctc.5c01299

15. G. Rescourio, A.Z. Gonzalez, S. Jabri, B. Belmontes, G. Moody, D. Whittington, X. Huang, S. Caenepeel, M. Cardozo, A.C. Cheng, D. Chow, and *et al*. Discovery and in vivo evaluation of macrocyclic Mcl-1 inhibitors featuring an α-hydroxy phenylacetic acid pharmacophore or bioisostere. *Journal of Medicinal Chemistry* 62(22): 10258-10271 (2019). https://doi.org/10.1021/acs.jmedchem.9b01310
16. D.V.D. Spoel, E. Lindahl, B. Hess, G. Groenhof, A.E. Mark, and H.J.C. Berendsen. GROMACS: Fast, flexible, and free. *Journal of Computational Chemistry* 26(16): 1701-1718 (2005). https://doi.org/10.1002/jcc.20291
17. N. Guex and M.C. Peitsch. SWISS-MODEL and the Swiss-Pdb Viewer: An environment for comparative protein modeling. *Electrophoresis* 18(15): 2714-2723 (1997). https://doi.org/10.1002/elps.1150181505
18. V. Zoete, M.A. Cuendet, A. Grosdidier, and O. Michielin. SwissParam: A fast force field generation tool for small organic molecules. *Journal of Computational Chemistry* 32(11): 2359-2368 (2011). https://doi.org/10.1002/jcc.21816
19. M.S. Valdés-Tresanco, M.E. Valdés-Tresanco, P.A. Valiente, and E. Moreno. gmx_MMPBSA: A new tool to perform end-state free energy calculations with GROMACS. *Journal of Chemical Theory and Computation* 17(10): 6281-6291 (2021). https://doi.org/10.1021/acs.jctc.1c00645
20. H.D. Nguyen. Unveiling the anti-apoptotic mechanism of magnolialide as a colorectal cancer inhibitor via molecular modeling, ADMET, and MMGBSA analysis. *Physical Chemistry Research* 13(4): 783-796 (2025). https://doi.org/10.22036/pcr.2025.535946.2708
21. F. Neese. Software update: The ORCA program system-version 6.0. *WIREs Computational Molecular Science* 15(2): e70019 (2025). https://doi.org/10.1002/wcms.70019
22. G. Knizia and J.E. Klein. Electron flow in reaction mechanisms-revealed from first principles. *Angewandte Chemie International Edition* 54(18): 5518-5522 (2015). https://doi.org/10.1002/anie.201410637
23. G. Knizia. Intrinsic atomic orbitals: An unbiased bridge between quantum theory and chemical concepts. *Journal of Chemical Theory and Computation* 9(11): 4834-4843 (2013). https://doi.org/10.1021/ct400687b
24. M.D. Hanwell, D.E. Curtis, D.C. Lonie, T. Vandermeersch, E. Zurek, and G.R. Hutchison. Avogadro: an advanced semantic chemical editor, visualization, and analysis platform. *Journal of Cheminformatics* 4(1): 17 (2012). https://doi.org/10.1186/1758-2946-4-17
25. J. Luo, Z.Q. Xue, W.M. Liu, J.L. Wu, and Z.Q. Yang. Koopmans' Theorem for Large Molecular Systems within Density Functional Theory. *The Journal of Physical Chemistry A* 110(43): 12005-12009 (2006). https://doi.org/10.1021/jp063669m
26. R. Das, J.L. Vigneresse, and P.K. Chattaraj. Chemical reactivity through structure-stability landscape. *International Journal of Quantum Chemistry* 114(21): 1421-1429 (2014). https://doi.org/10.1002/qua.24706
27. Z. Ma, A. Ajibade, and X. Zou. Docking strategies for predicting protein-ligand interactions and their application to structure-based drug design. *Communications in Information and Systems* 24(3): 199 (2024). https://doi.org/10.4310/cis.241021221101
28. S.I. Tantawy, N. Timofeeva, A. Sarkar, and V. Gandhi. Targeting MCL-1 protein to treat cancer: opportunities and challenges. *Frontiers in Oncology* 13: 1226289 (2023). https://doi.org/10.3389/fonc.2023.1226289
29. D.A. Schaller, C.D. Christ, J.D. Chodera, and A. Volkamer. Benchmarking Cross-Docking Strategies in Kinase Drug Discovery. *Journal of Chemical Information and Modeling* 64(23): 8848-8858 (2024). https://doi.org/10.1021/acs.jcim.4c00905
30. A.O.H. Zayed. Optimizing protein-ligand docking through machine learning: algorithm selection with AutoDock Vina. *Discover Chemistry* 2(1): 164 (2025). https://doi.org/10.1007/s44371-025-00246-4
31. Q. Sun. The hydrophobic effects: Our current understanding. *Molecules* 27(20): 7009 (2022). https://doi.org/10.3390/molecules27207009
32. T.V. Szalai, D. Bajusz, R. Börzsei, B.Z. Zsidó, J. Ilaš, G.G. Ferenczy, C. Hetényi, and G.M. Keserű. Effect of water networks on ligand binding: Computational predictions vs experiments. *Journal of Chemical Information and Modeling* 64(23): 8980-8998 (2024). https://doi.org/10.1021/acs.jcim.4c01291
33. A. McGriff and W.J. Placzek. Phylogenetic analysis of the MCL1 BH3 binding groove and rBH3 sequence motifs in the p53 and INK4 protein families. *PLoS One* 18(1): e0277726 (2023). https://doi.org/10.1371/journal.pone.0277726

34. J. Sharifi-Rad, C. Quispe, J.K. Patra, Y.D. Singh, M.K. Panda, G. Das, C.O. Adetunji, O.S. Michael, O. Sytar, L. Polito, J. Živković, N. Cruz-Martins, M. Klimek-Szczykutowicz, H. Ekiert, M.I. Choudhary, S.A. Ayatollahi, B. Tynybekov, F. Kobarfard, A.C. Muntean, I. Grozea, S.D. Dastan, M. Butnariu, A. Szopa, and D. Calina. Paclitaxel: Application in modern oncology and nanomedicine-based cancer therapy. *Oxidative Medicine and Cellular Longevity* 2021(1): 3687700 (2021). https://doi.org/10.1155/2021/3687700
35. G.G. Ferenczy and M. Kellermayer. Contribution of hydrophobic interactions to protein mechanical stability. *Computational and Structural Biotechnology Journal* 20: 1946-1956 (2022). https://doi.org/10.1016/j.csbj.2022.04.025
36. V.A. Adhav and K. Saikrishnan. The realm of unconventional noncovalent interactions in proteins: Their significance in structure and function. *ACS Omega* 8(25): 22268-22284 (2023). https://doi.org/10.1021/acsomega.3c00205
37. O.M.H. Salo-Ahen, I. Alanko, R. Bhadane, A.M.J.J. Bonvin, R.V. Honorato, S. Hossain, A.H. Juffer, A. Kabedev, M. Lahtela-Kakkonen, A.S. Larsen, E. Lescrinier, P. Marimuthu, M.U. Mirza, G. Mustafa, A. Nunes-Alves, T. Pantsar, A. Saadabadi, K. Singaravelu, and M. Vanmeert. Molecular dynamics simulations in drug discovery and pharmaceutical development. *Processes* 9(1): 71 (2021). https://doi.org/10.3390/pr9010071
38. R.F. de Freitas and M. Schapira. A systematic analysis of atomic protein-ligand interactions in the PDB. *MedChemComm* 8(10): 1970-1981 (2017). https://doi.org/10.1039/C7MD00381A
39. E. Wang, H. Sun, J. Wang, Z. Wang, H. Liu, J.Z.H. Zhang, and T. Hou. End-point binding free energy calculation with MM/PBSA and MM/GBSA: Strategies and applications in drug design. *Chemical Reviews* 119(16): 9478-9508 (2019). https://doi.org/10.1021/acs.chemrev.9b00055
40. L. Dong, P. Li, and B. Wang. Enhancing MM/P(G)BSA methods: Integration of formulaic entropy for improved binding free energy calculations. *Journal of Computational Chemistry* 46(10): e70093 (2025). https://doi.org/10.1002/jcc.70093
41. I. Ahmad, V. Jagatap, and H. Patel. Application of density functional theory (DFT) and response surface methodology (RSM) in drug discovery. In: Phytochemistry, computational tools and databases in drug discovery. C. Egbuna, M. Rudrapal, and H. Tijjani (Eds.). *Elsevier, Amsterdam, Netherlands* pp. 371-392 (2023). https://doi.org/10.1016/B978-0-323-90593-0.00004-6
42. V. Hadigheh Rezvan, Molecular structure. HOMO-LUMO, and NLO studies of some quinoxaline 1,4-dioxide derivatives: Computational (HF and DFT) analysis. *Results in Chemistry* 7: 101437 (2024). https://doi.org/10.1016/j.rechem.2024.101437
43. Y. Xu, Q. Chu, D. Chen, and A. Fuentes. HOMO-LUMO Gaps and Molecular Structures of Polycyclic Aromatic Hydrocarbons in Soot Formation. *Frontiers in Mechanical Engineering* 7: 744001 (2021). https://doi.org/10.3389/fmech.2021.744001
44. P. Geerlings. From density functional theory to conceptual density functional theory and biosystems. *Pharmaceuticals* 15(9): 1112 (2022). https://doi.org/10.3390/ph15091112
45. R. Pal and P.K. Chattaraj. Electrophilicity index revisited. *Journal of Computational Chemistry* 44(3): 278-297 (2023). https://doi.org/10.1002/jcc.26886

Proceedings of the Pakistan Academy of Sciences: A Physical and Computational Sciences 63(2): 115-122 (2026)

ISSN (Print): 2518-4245; ISSN (Online): 2518-4253
http://doi.org/10.53560/PPASA(63-2)715

Pakistan Academy of Sciences

Research Article

Temperature-Dependent Optical Properties of Spray-Pyrolyzed Cadmium Oxide Thin Films

Helen J. Abdalhussain[1*], Rasool O. Saleem[2], and Aws A. Mahdi[1]

[1]Department of Radiology, Institute of Medical Technology - Baghdad, Middle Technical University, Baghdad, Iraq
[2]Department of Anaesthesia, Institute of Medical Technology - Baghdad, Middle Technical University, Baghdad, Iraq

Abstract: In present study, Cadmium Oxide (CdO) films have been prepared using spray pyrolysis deposition (SPD) at different substrate temperatures (350, 450, and 550 °C) with glass substrate. Thickness of these films prepared was approximately 400 ± 10 nm. XRD diffraction analysis revealed the CdO were polycrystalline and cubic, exhibiting grain sizes ranging from 198.5 to 229.8 nm. The effect of varying substrate temperatures on the optical properties of CdO was analyzed by examining transmittance and absorbance spectra within the 300 to 900 nm range. The transmittance of CdO increases with increasing the substrate temperature. The energy gap for direct transitions was determined to range between 2.4 and 2.5 electron volts. It was found that varying the substrate temperature affects CdO films, increasing its transmittance and energy gap, and decreasing its reflectivity, absorbance coefficient, extinction coefficient, real parts and imaginary parts of the dielectric constant, and refractive index. Based on these observed properties, thin films fabricated in this way can be used in sensors and catalysts, or in solar cells.

Keywords: Cadmium Oxide (CdO), Optical Properties, Spray Pyrolysis Deposition (SPD), Energy Gap, X-ray Diffraction.

1. INTRODUCTION

Currently, cadmium oxide (CdO) films have become increasingly important in the photovoltaic cell industry, mainly due to their exceptional optical transparency and excellent electrical conductivity across visible and ultra-visible light spectra, and having excellent gas sensing properties [1]. CdO is classified as a transparent conductive oxide due to its remarkable physical properties, including its high optical transmittance within the visible spectrum and excellent charge carrier mobility [2]. Conductive CdO films are gaining increasing recognition for their significant importance due to their diverse industrial and technological applications, these applications include is diodes, solar cells, phototransistors, and gas sensors [3].

CdO is classified in groups II-VI of the periodic table; having a cubic crystal structure characterized by XRD [4]. It is an n-type semiconductor characterized by direct energy band gap ranging from 2.2 - 2.5 electron volts [5]. Researchers have sought to discover new deposition techniques to improve upon existing methods, and it is observed that the physical properties of the films vary depending on the deposition method [6]. In this context, CdO has garnered significant attention due to its electrical, optical, and chemical properties, leading to its uses in advanced applications [7]. Various methods have been used to synthesize CdO thin films, such as chemical vapor deposition (CVD) [8, 9], chemical spray deposition [10], magnetic spray deposition [5], sol-gel deposition [11], and chemical spray decomposition (CSP) [12].

In the present study we have synthesized thin films of CdO using spray pyrolysis deposition technique and their optical properties are measured at different substrate temperatures (350, 450, and

Received: February 2026; Revised: May 2026; Accepted: June 2026
* Corresponding Author: Helen J. Abdalhussain <h.helenjabbar@mtu.edu.iq>

550 °C). The structural and optical properties of the as prepared films were thoroughly investigated by X-ray diffraction (XRD) and UV-Vis spectroscopy. In future, we can explore the potentials of this material as a gas sensor, catalyst, use in solar cells, and assess the feasibility of applying these findings in industrial applications.

2. MATERIALS AND METHODS

Cadmium acetate $Cd(CH_3COO)_2.2H_2O$ with molecular weight (266.52 g/mol), supplied by the British company (BHD) with a purity of 99%, was used to prepare the solution used to produce the CdO thin film. The solution was prepared at a molar concentration of (0.1 mol/L) by adding (2.6652 g) of it to (100 ml) of distilled water and gradually dissolving it by a magnetic stirrer for (15-20) minutes according to the Equation (1) [13]. This resulted in a clear, homogeneous, and colorless solution.

$$M = \left(\frac{W_t}{M_{wt}}\right)\left(\frac{1000}{V}\right) \quad (1)$$

where M is the molar concentration, W is the weight of the solute, M_{Wt} is the molecular weight of the substance, and V is the volume of distilled water in which the solute was dissolved.

After preparation of the solution Spray Pyrolysis Deposition (SPD) method was used to deposit CdO thin films at different substrate temperatures. Table 1 shows the detailed conditions used for the synthesis of the CdO thin films.

After spraying process is complete, the gases evaporate due to heat, leaving a cadmium oxide on the substrate according to the Equation of reaction [4]:

$$(CH_3COO)_2Cd.2H_2O + H_2O \rightarrow CdO + 2H_2O\uparrow + 2CH_3COOH\uparrow$$

The thin film thickness (t) was calculated using helium-neon (He-Ne) laser interferometry method, it was calculated from the following Equation (2) [14]:

$$t = \frac{\Delta L}{L} * \frac{\lambda}{2} \quad (2)$$

where λ is the wavelength of the laser light used and its value (632.8 nm), L is the width of the bright fringe (nm), and ΔL is the width of the dark fringe (nm).

Figure 1 depicts the diagram of workflow and measurements adopted during the preparation and analysis of the CdO thin films.

Table 1. Standard conditions used for the synthesis of the CdO thin films.

Parameters of spray	
Distance between substrate and atomizer	25 cm
Liquid flow rate	1 ml min^{-1}
Utilized air compressor	1 bar
Time for spraying	20 min
Interval between sprays	5 min

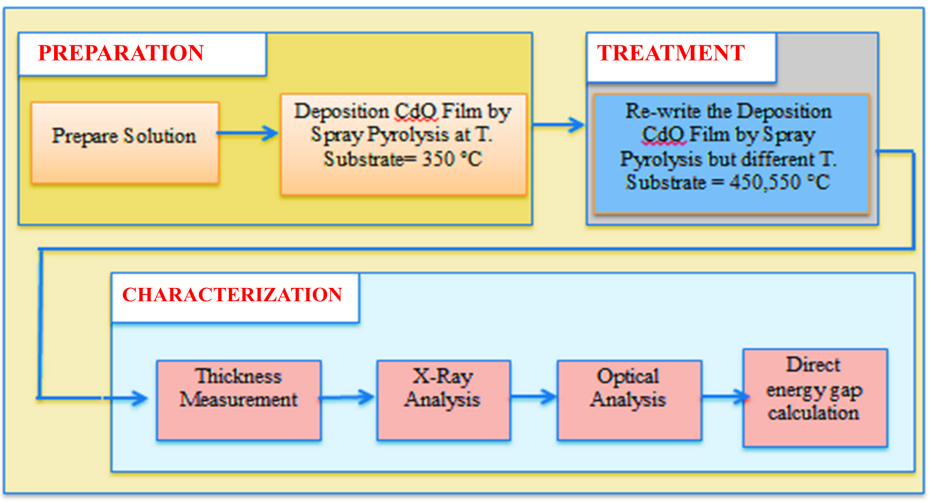

Fig. 1. Diagram the workflow and measurements used in the preparation and analysis of CdO thin films.

3. RESULTS AND DISCUSSION

The structural analysis and crystallinity of CdO thin films were investigated by X-ray diffraction which is crucial for understanding the relation between the optical properties and structural variations of these films. The XRD diffraction spectra shown in Figure 2, confirm that the CdO thin films are polycrystalline and have a cubic symmetry [9]; which is consistent with standard diffraction data (JCPDS card 05-0640). Figure 2 also represents that the main peaks (111), (200), and (220), which are the dominant diffraction peaks, indicate characteristic reflections of CdO. The highest intensity was recorded for (111) peak, which is the preferred direction for crystal growth [9].

The average grain size (G) was calculated from (111) plane by applying Scherrer Equation (3) [9]:

$$G = \frac{0.9\lambda}{\beta \cos\theta} \quad (3)$$

where λ represents the wavelength of the X-rays, β is the full width at half maximum (FWHM) of the diffraction peak and θ is the angle of the diffraction peak.

Table 2 shows that the average grain size increases with increasing substrate temperature, ranging from 198.5 to 229.8 nm. This increase in average crystal size is attributed to increased crystal disorder resulting from the higher substrate temperature.

The optical properties of the CdO thin films play a vital role in their evaluation and the determination of their potential applications. This includes examining key optical properties and determining the optical band gap of the CdO thin films at different substrate temperatures.

3.1. Transmittance (*T*)

Figure 3 illustrates the change in transmittance values with wavelength for CdO films prepared at different substrate temperatures. These results show that transmittance is increased with increasing wavelength; however, with increase in the substrate temperature, we observe that the behavior of the transmittance spectrum curve does not change. It is evident that the value of transmittance increases with increasing the substrate temperature; this can be attributed that by increasing the substrate temperature structural defects are reduced, which are attenuating regions for the incident radiation, and thus changes values of absorbance coefficient with increase in crystallinity of thin films. This is consistent with what was stated in the published research [15].

3.2. Absorbance (*A*)

Figure 4 demonstrates the change in absorbance values with wavelength for CdO films prepared at different substrate temperature. The maximum absorbance value is at short wavelengths, after

Table 2. Average grain size of the CdO thin films at different substrate temperature.

Temperature °C	350 °C	450 °C	550 °C
G(nm) (111)	198.5	226.1	229.8

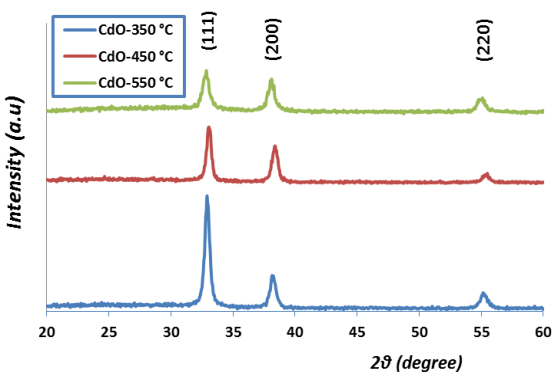

Fig. 2. XRD diffraction of CdO thin film with different substrate temperatures.

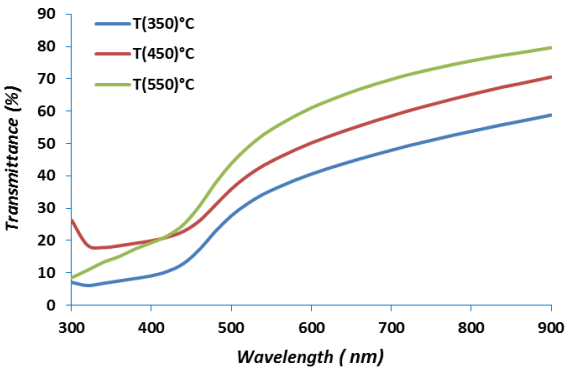

Fig. 3. Relationship between Transmittance (T) with wavelength (λ) for different substrate temperatures.

which it rapidly decreases in the (300-500) nm range, and then gradually decreases in the (500-900) nm range, reaching its lowest value at (900) nm. This decrease in the absorbance can be ascribed that the energy of the photons is less than energy gap value, making them unable to excite electrons and transfer them from the valence band to the conduction band [16]. In addition, from Figure 4 it observed that by increasing the substrate temperature does not affect the behavior of the absorbance spectrum curve; however, it is found that to have a decreasing trend in the absorbance value as the different substrate temperature is increased, and this can be due a change in energy gap values.

3.3. Reflectivity (*R*)

The reflectivity was calculated from the fallowing Equation (4) [17]:

$$R + T + A = 1 \tag{4}$$

Figure 5 shows the reflectivity decreases with increasing wavelength, as well as with increase in the substrate temperature. Because due to change in surface roughness with increasing temperature, it is known that roughness is inversely proportional to grain size. This behavior is consistent with the transmittance results and absorbance according to Equation (4).

3.4. Absorbance Coefficient (α)

The absorbance coefficient (α) is calculated from Equation (5) by employing Beer-Lambert Law [18]:

$$\alpha = \frac{2.303 \times A}{t} \tag{5}$$

where A is the absorbance of the material and t is the thickness of the film.

Figure 6 demonstrates that absorbance coefficient of the CdO films decreases with both increasing wavelength and increasing substrate temperature. The temperature-induced decrease can be attributed to the thermal remediation of structural defects. Deviations from the ideal stoichiometric and crystalline structure of a semiconductor typically generate localized energy levels within the band gap (above the valence band and below the conduction band), which supply free charge carriers (electrons or holes). Higher substrate temperatures reduce these structural deviations, thereby eliminating some of these localized states and decreasing the carrier concentration. Consequently, both free-carrier absorbance and defect-mediated transitions are suppressed, leading to a lower absorbance coefficient [19]. These results show that CdO the films have high absorbance coefficient ($\alpha > 10^4\ cm^{-1}$), this suggests the existence of direct electronic transitions [20].

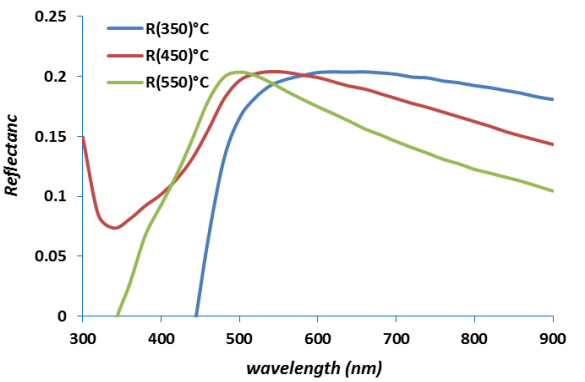

Fig. 5. Relationship between Reflectance (R) with wavelength (λ) for different substrate temperatures.

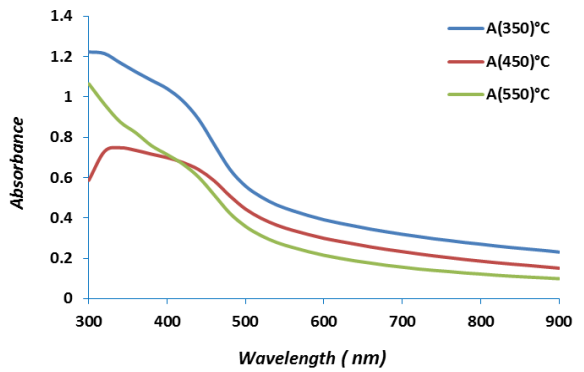

Fig. 4. Relationship between Absorbance (*A*) with wavelength (λ) for different substrate temperatures.

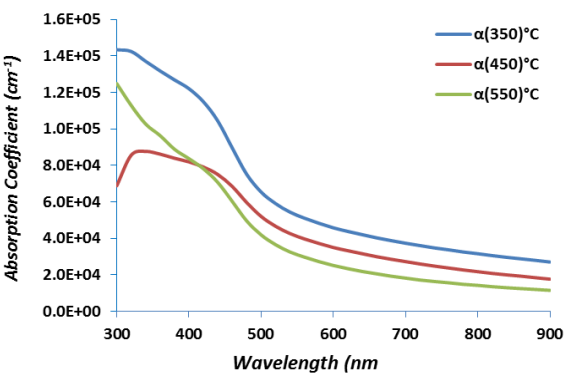

Fig. 6. Relationship between Absorbance Coefficients (α) with wavelength (λ) for different substrate temperatures.

3.5. Optical Energy Gap (E_g)

Figure 7 displays the variations in the optical energy gap (E_g) of the CdO films prepared at different substrate temperatures. The data reveals that the energy gap increases with rising substrate temperature. This broadening of the band gap can be attributed to the thermal reduction of structural defects and the subsequent elimination of localized states lying within the forbidden region between the valence and conduction bands. As these mid-gap defect states are minimized at higher temperatures, the fundamental absorbance edge sharpens and shifts to higher energies, resulting in an increased effective energy gap.

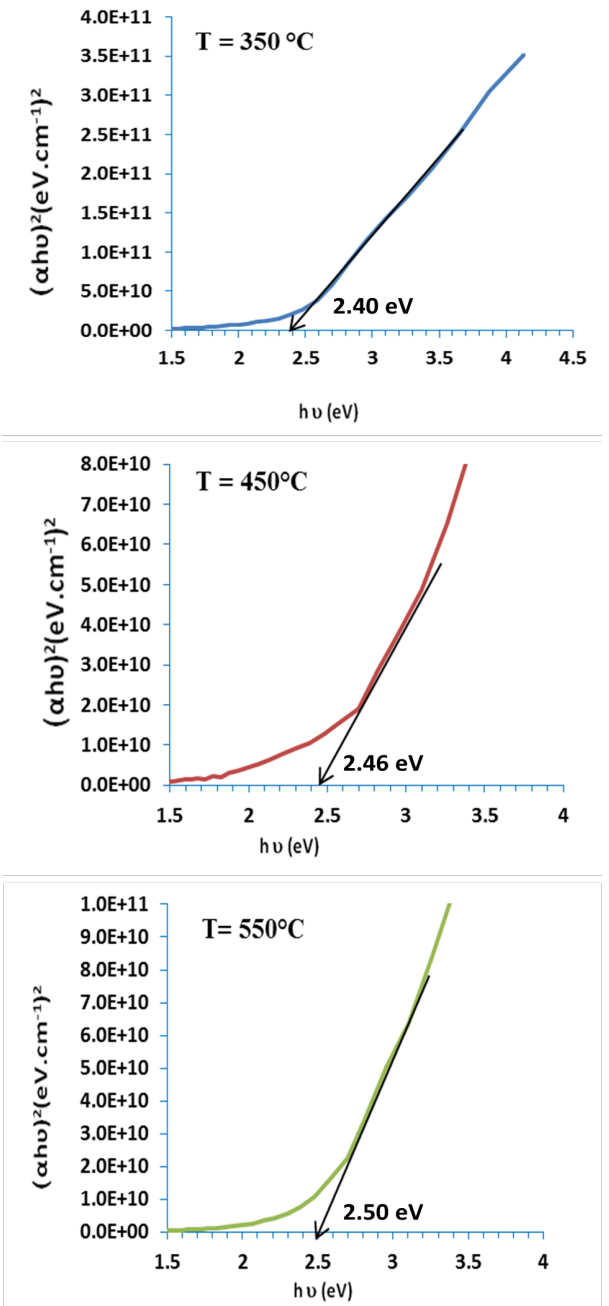

Fig. 7. Relationship between $(\alpha h\nu)^2$ and photon energy $(h\nu)$ for different substrate temperatures.

3.6. Extinction Coefficient (K_o)

Extinction Coefficient (K_o) is derived from Equation (6) [21]:

$$K_o = \frac{\alpha \lambda}{4\pi} \tag{6}$$

where λ is the wavelength of the incident beam.

Figure 8 shows the variation in extinction coefficient with changing wavelength for CdO films prepared at different substrate temperatures. The extinction coefficient decreases as the wavelength increases, exhibiting a sharp decline near λ = 500 nm. This trend is attributed to decreased absorbance at longer wavelengths, which occurs when the incident photon energy drops below the optical bandgap energy. Furthermore, by changing the substrate temperature does not alter the overall profile of the extinction coefficient curve; however, the magnitude of the extinction coefficient decreases as the substrate temperature rises.

3.7. Refractive Index (n)

Refractive Index (n) is derived from Equation (7) [22]:

$$n = \left(\frac{1+R}{1-R}\right) \pm \sqrt{\frac{4R}{(1-R)^2} - K^2} \tag{7}$$

where K is extinction coefficient.

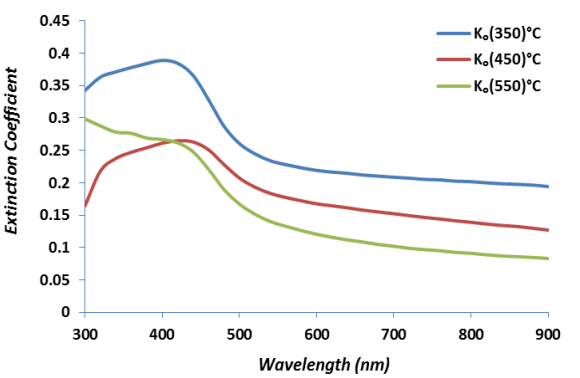

Fig. 8. Relationship between the Extinction Coefficient (K_o) with wavelength (λ) for different substrate temperatures.

Figure 9 depicts the change in refractive index values with varying wavelength for CdO films having substrate temperatures. The refractive index reaches its highest peak value in the blue/violet spectral region (450 nm), then begins to decrease with increase in the wavelength. This decrease in refractive index can be attributed to two interpretations: the effect of voids causing a reduction in density [23], and the effect of abnormal scattering, where the film shows abnormal scattering in the range of 450-900 nm, where *n* decreases with decreasing photon energy with increasing wavelength [24]. We find that the behavior of the refractive index curve does not change, but the refractive index value decreases with increasing the substrate temperature.

3.8. Dielectric Constant

The dielectric constant with real (ε_r) and imaginary (ε_i) parts has been calculated from Equations (8) and (9) [25].

$$\varepsilon_{r} = n^2 - K^2 \quad (8)$$

$$\varepsilon_i = 2n\,K \quad (9)$$

where ε_r is the real part and ε_i is the imaginary part of dielectric constants.

Figure 10 and Figure 11 present the wavelength dependence of the real (ε_r) and imaginary (ε_i) parts of the dielectric constant for the CdO films with varying substrate temperatures. For all films the dielectric constants increase with increasing the wavelength up to ($\lambda \approx 500nm$), and then begin to decrease.

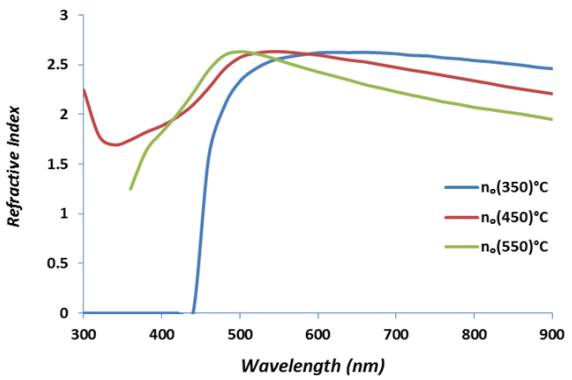

Fig. 9. Relationship between refractive index (*n*) with wavelength (λ) for different substrate temperatures.

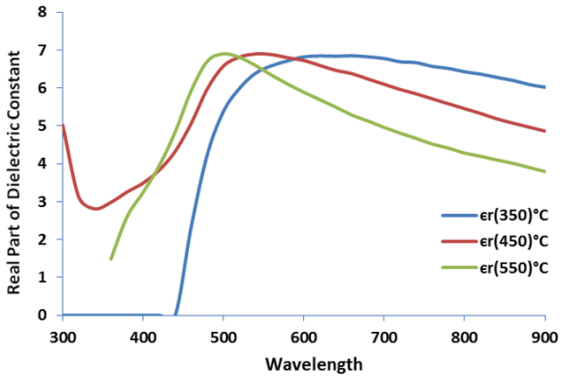

Fig. 10. Variation of real part of dielectric constant (ε_r) with wavelength (λ) for different sabstrate temperatures.

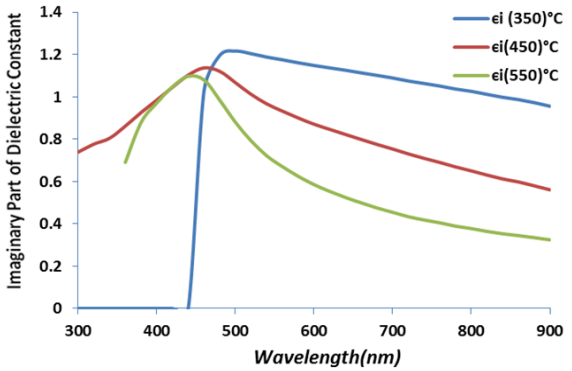

Fig. 11. Variation of imaginary part of dielectric constant (ε_i) with wavelength (λ) for different sabstrate temperatures.

4. CONCLUSIONS

The present study demonstrates that structural properties investigated by X-ray diffraction analysis confirmed the CdO films were polycrystalline and have a cubic structure, exhibiting grain sizes ranging from 198.5 to 229.8 nm. The optical properties of CdO thin films are significantly optimized by thermal treatment, achieving a high optical transmittance more than 80% for film synthesized at a substrate temperature of 550 °C. A systematic increase in the transmittance is observed at rising substrate temperatures. Furthermore, the CdO thin films exhibited a high absorbance coefficient ($\alpha > 10^4\ cm^{-1}$) within the 300-900 nm spectral range, which strongly indicates direct electronic transitions and confirms a direct optical band gap, consistent with this structural improvement, the optical energy gap (E_g) shifts toward higher energies with increasing substrate temperatures. This thermal enhancement corresponds directly to a uniform decrease in the values of the extinction

coefficient, refractive index, and both the real part (ε_r) and imaginary part (ε_i) of the dielectric constants across the investigated 300-900 nm wavelength range.

5. ACKNOWLEDGMENTS

The authors acknowledge with gratitude the institutional support and resources that enabled the successful execution of this study.

6. ETHICAL STATEMENT

This study did not involve any human participants or live animal testing. Therefore, ethical approval was not required for this research.

7. CONFLICT OF INTEREST

The authors declare no conflict of interest.

8. FUNDING

The authors received no financial support for the research authorship and or publication of this article.

9. AUTHORSHIP CONTRIBTION STATEMENT

All authors contributed to this work. Helen J. Abdalhussain, Rasool O. Saleem and Aws A. Mahdi produced the idea and method of work. Helen J. Abdalhussain, Rasool O. Saleem conducted the practical application, calculations, and data analysis. Rasool O. Saleem, Aws A. Mahdi worked on writing the theoretical part. All authors contributed to writing the summary and conclusion.

10. DECLARATION

All authors of this study, declare that the results of this study are original. The same material is neither published nor under consideration for publication elsewhere. In case the article is accepted for publication, its copyright will be assigned to the Pakistan Academy of Sciences. All results were interpreted solely by the authors; Grammarly and Google Translate were used for English language refinement.

11. REFERENCES

1. R.H. Bari and S.B. Patil. Nanostructured CdO Thin Films for LPG and CO_2 Gas Sensor Prepared by Spray Pyrolisis Technique. *International Letters of Chemistry, Physics and Astronomy* 37: 31-46 (2014). https://doi.org/10.56431/p-lfu9x5
2. B. Sahin and R. Aydin. SILAR derived CdO films: Effect of triethanolamine on the surface morphology and optical band gap energy. *Physica B: Condensed Matter* 541: 95-102 (2018). https://doi.org/10.1016/j.physb.2018.04.043
3. M.M. Rahman, M.M. Alam, and K.A. Alamry. Sensitive and selective m-tolyl hydrazine chemical sensor development based on CdO nanomaterial decorated multi-walled carbon nanotubes. *Journal of Industrial and Engineering Chemistry* 77: 309-316 (2019). https://doi.org/10.1016/j.jiec.2019.04.053
4. R. Ahmad, H. Qays, J. Hussein, G. Hameed, and I. Razzaq. Study of physical properties of CdO Thin film prepared by Chemical spray pyrolysis Technique. *Diyala Journal for Pure Sciences* 13(4): 91-105 (2017). http://repo.uodiyala.edu.iq/bitstream/xmlui/5143/1/7-P1%28318%29.pdf
5. V. Revath and K. Karthik. Microwave assisted CdO–ZnO–MgO nanocomposite and its photocatalytic and antibacterial studies. *Journal of Materials Science: Materials in Electronics* 29(21): 18519-18530 (2018). https://doi.org/10.1007/s10854-018-9968-1
6. T. Prakash, G. Neri, and E.R. Kumar. A comparative study of the synthesis of CdO nanoplatelets by an albumen-assisted isothermal evaporation method. *Journal of Alloys and Compounds* 624: 258-265 (2015). https://doi.org/10.1016/j.jallcom.2014.10.204
7. Z. Ganjian, F.J. Sheini, and R. Yousefi. Electrochemical synthesis and physical properties of Sn-doped CdO nanostructures. *Superlattices and Microstruct*ures 100: 988-996 (2016). https://doi.org/10.1016/j.spmi.2016.10.064
8. X. Li, D.L. Young, H. Moutinho, Y. Yan, C. Narayanswamy, T.A. Gessert, and T.J. Coutts. Properties of CdO Thin Films Produced by Chemical Vapor Deposition. *Electrochemical and Solid-State Letters* 4(6): C43-C46 (2001). https://doi.org/10.1149/1.1369216
9. G.P. Gadkar. Chemical Vapour Deposited CdO thin film for ethanol sensing. *International Journal of Advanced Engineering, Management and Science* 9(4): 20-23 (2023). https://dx.doi.org/10.22161/ijaems.94.3
10. G.N. Alaa, B.Y. Hakam, F.Z. Narmeen, M.T. Ahmed, H.M. Wand, H.A. Layla, and S.A. Hazem. Effect the Distance on the Optical Properties of CdO Thin Films Prepared by Thermochemical Spray Method

at Moving Substrate Mode. *Journal of Materials and Environmental Science* 16(5): 827-835 (2025). https://www.jmaterenvironsci.com/Document/vol16/vol16_N5/JMES-2025-1605057-Alaa.pdf

11. S. Singh, V. Sharma, and K. Sachdev. Investigation of effect of doping concentration in Nb-doped TiO_2 thin films for TCO applications. *Journal of Materials Science* 52(19): 11580-11591 (2017). https://doi.org/10.1007/s10853-017-1328-7
12. D.S. Jbaier. Physical Properties of CdO Thin Films Prepared by Spray Pyrolysis Technique. *Engineering and Technology Journal* 31(2): 185-194 (2013). https://uotechnology.edu.iq/tec_magaz/2013/volum312013/No.02.B.2013/Text%20(6).pdf
13. M.S. Sinjar, M.A. Al-Jubbori, and H.H. Algdirree. Study of the Effect of Irradiation on Some Optical Properties of Cadmium Oxide Films Prepared by the Thermal Chemical Spraying Method. *Journal of Education and Science* 34(2): 1-12 (2025). https://doi.org/10.33899/edusj.2024.154469.1511
14. R.A. Al-Ansari, H.Q. Khaleel, J.H. Awadh, G.H. Mohammed, and I.R. Swadi. Study of Physical Properties of CdO Thin Film Prepared by Chemical Spray Pyrolysis Technique. *Diyala Journal for Pure Sciences* 13(4): 91-105 (2017). http://dx.doi.org/10.24237/djps.1304.318E
15. R.K. Gupta, K. Ghosh, R. Patel, and P.K. Kahol. Highly Conducting and Transparent Ti-doped CdO Films by Pulsed Laser Deposition. *Journal of Applied Surface Science* 255(12): 6252-6255 (2009). https://doi.org/10.1016/j.apsusc.2009.01.091
16. O. Ayed, M.A. Al-Jubbori, and H.H. Algdirree. Study of the optical properties of copper oxide thin films prepared by chemical spray pyrolysis technique. *Journal of Education and Science* 33(2): 47-57 (2024). https://doi.org/10.33899/edusj.2024.146903.1426
17. D.M. Latif, I.H. Shallal, and A.A. Shuihab. Synthesis and study of some physical properties of cadmium oxide CdO thin films. *Energy Procedia* 157: 611-618 (2019). https://doi.org/10.1016/j.egypro.2018.11.226
18. I.S. Yahia, G.F. Salem, M.S.A. El-Sadek, and F. Yakuphanoglu. Optical properties of Al-CdO nano-clusters thin films. *Superlattices and Microstructures* 64: 178-184 (2013). https://doi.org/10.1016/j.spmi.2013.09.024
19. J.I. Pankove (Ed.). Optical processes in semiconductors. *Prentice – Hall* (1971).
20. S.K. Kalli. Optical properties of CdO thin films. *Baghdad Science Journal* 7(1): 10-13 (2010). https://doi.org/10.21123/bsj.2010.7.1.10-13
21. K. Siraj, M. Khaleeq-ur-Rahman, S.I. Hussain, M.S. Rafique, and S. Anjum. Effect of deposition temperature on structural, surface, optical and magnetic properties of pulsed laser deposited Al-doped CdO thin films. *Journal of Alloys and Compounds.* 509(24): 6756-6762 (2011). https://doi.org/10.1016/j.jallcom.2011.03.183
22. N. Manjula and A.R. Balu. Double doping (Mn +Cl) effects on the structural, morphological, photoluminescence, optoelectronic properties and antibacterial activity of CdO thin films. *Optik* 130: 464-472 (2017). https://doi.org/10.1016/j.ijleo.2016.10.074
23. M.A. Rahman and M.K.R. Khan. Effect of annealing temperature on structural, electrical and optical properties of spray pyrolytic nanocrystalline CdO thin films. *Materials Science in Semiconductor Processing* 24: 26-33 (2014). https://doi.org/10.1016/j.mssp.2014.03.002
24. A.M. Abdulwahab, T.S. Aldeen, and S.N. Aziz. Synthesis and characterization of multifunctional CdO-CuO-ZnO-Co_3O_4 nanocomposite. *Results in Physics* 75: 108335 (2025). https://doi.org/10.1016/j.rinp.2025.108335
25. F.S. Ahmed, N.Y. Ahmed, R.S. Ali, N.F. Habubi, K.H. Abass, and S.S. Chiad. Effects of Substrate Type on Some Optical and Dispersion Properties of Sprayed CdO Thin Films. *NeuroQuantology* 18(3): 56-65 (2020). https://uomustansiriyah.edu.iq/media/attachments/221/221_2020_06_04!05_35_27_AM.pdf

Proceedings of the Pakistan Academy of Sciences: A Physical and Computational Sciences 63(2): 123-132 (2026)

ISSN (Print): 2518-4245; ISSN (Online): 2518-4253
http://doi.org/10.53560/PPASA(63-2)708

Pakistan Academy of Sciences

Research Article

A Robust Stacked Ensemble Approach for House Price Prediction

Muhammad Khateeb Khan[1]*, Asad Ullah Khan[2], Salman Ahmed[3], and Wajid Ali[4]

[1]Faculty of Engineering & Computing, Software Engineering, NUML, Islamabad, Pakistan
[2]Faculty of Computing & Technology, Computer Science, IQRA, Islamabad, Pakistan
[3]Faculty of Engineering & Computing, Computer Science, NUML, Islamabad, Pakistan
[4]School of Computer Science & Artificial Intelligence, Computer Science,
Duy Tan University, Danang, Vietnam

Abstract: Real estate price prediction plays a fundamental role in decision-making and ensuring market stability for buyers, sellers, and property owners. Since the real estate sector has a significant impact on the global economy, accurate prediction models are crucial. In this study, we used the Ames Housing dataset and performed thorough preprocessing to handle missing values, reduce multicollinearity, and enhance feature quality. We introduced three new features, total square footage, total porch area and the age of the house to capture the better property characteristics. After these steps, we evaluated a range of machine learning (ML) models, including Linear Regression, Ridge, Lasso, Decision Trees, Random Forest, Gradient Boosting, XGBoost, LightGBM, and CatBoost and explored hybrid combinations with weighed ensemble and stacked ensemble strategies. We proposed CXL Stacked Ensemble (CatBoost + XGBoost + LightGBM) model with ridge regression as meta-learner and the model outperformed with R^2 of 0.9333 and a normalized RMSLE of 0.1132, demonstrating the superior model predictive capability. To validate its robustness fold-wise RMSE comparisons and significance tests (paired t-test and Wilcoxon signed-rank test) were conducted. Additionally, cross-validation and residual error analysis validated model reliability. This work depicts the effectiveness of stacked ensemble methods for real state price predication and provides practical insights for stakeholders to make informed decision.

Keywords: Real Estate, Stacked Ensemble Methods, Price Prediction, Residuals Analysis, Multimodal.

1. INTRODUCTION

Real estate is vital to the world economy and overall economic growth. In fact, real estate prices are intricately linked to the dynamics of the real estate market and play an important role in the development of nations, both domestically and internationally. Some of the factors that affect property pricing are geographic, size of the property, economic, and demographic changes. It is, therefore, essential that real estate buyers, sellers, investors, and realtors be able to predict the price of a house accurately when dealing in real estate investment. In the past few years, machine learning has proven to be an invaluable asset in extracting insightful patterns from intricate datasets, whether they are large or small, in various regions and industries of real estate. The Boston Housing dataset from the UCI ML Repository has been used in many studies and has several features related to the property and real estate market. Data mining algorithms were applied by Buyrukoglu and Uzut [1] in the field of real estate price prediction and they identified great potential of such methods in the market. A recent research study by Ding [2] has used three classifiers to test a bunch of features on the Boston housing dataset and XGBoost outperformed while comparing with others. Crime rates, property tax rates, and other local amenities are among the potential variables that could impact property value and are often tested and refined to develop a predictive model. For instance, Harrison and Rubinfeld [3] conducted a

Received: September 2025; Revised: May 2026; Accepted: June 2026
* Corresponding Author: Muhammad Khateeb Khan <m.khateeb231@gmail.com>

basic study on the Boston Housing Dataset and used multiple regression analysis to explore the effect of air pollution and other variables on housing prices. Other research used supervised ML algorithms including the Decision Trees and Support Vector Machines (SVM) to improve accuracy in prediction, Xibin *et al*. [4]. In addition, the use of robust and powerful ensemble models such as Random Forests (RF) has been highlighted as useful for high data variability contexts Lundberg *et al*. [5]. While the feature engineering and ensemble modeling techniques have led to significant improvements, there are still several issues that need to be addressed, including further fine-tuning the performance of the models and gaining insight into the conditions and limitations of each model. Aniobi *et al*. [6] made a comparison between six regression models LR, LASSO, Ridge, KNN-R, DTR, and ETR. Linear Regression, and had achieved an R^2 of 0.57 with moderate predictive capability.

Researchers have concentrated mainly on making improvements to prediction accuracy, rather than considering the deployment of models for real estate stakeholders. Further, the implementation of user-friendly interfaces for non-technical professionals is still a challenge and is a factor that is still constraining the actual use of these models, Tekouabou *et al*. [7]. In the study of prediction of house prices in Boston, Chen [8] used LR, RF, XGBoost and SVM. Random Forest had the highest R^2 value of 0.8641 while SVM had the lowest R^2 value of 0.5900. With the economy's current state, discussing property values has grown in importance over the years. Muralidharan *et al*. [9] employed Decision Trees and Artificial Neural Networks to forecast the price of houses in residential areas based on the housing and crime statistics. The study emphasizes the significance of housing markets in the U.S. economy, and companies such as Zillow use massive amounts of data to forecast the market and understand consumer behavior.

The recent studies were carried out on the Ames Housing dataset to show the effectiveness of machine learning techniques to predict house prices. Han [10] explored advanced regression models and emphasized the importance of validation and model selection in ensuring good performance. Kumar *et al*. [11] proposed an improved XGBoost model, which has high predictive accuracy with an R^2 of around 0.923 and low RMSE, which is better than the traditional approaches. Likewise, Zhao [12] tested a variety of models and found that ensemble methods, especially Random Forest, exhibit very good performance, with an R^2 of 0.85 and an RMSE of 3536. Though these are exciting developments, there are still open research questions concerning feature redundancy, model interpretability and optimal integration of heterogeneous learners.

This research aims of the present study are: (1) implement and test different algorithms of ML models to select the most accurate model for predicting property prices, and (2) use a stacked ensemble model to improve prediction accuracy, so that the stakeholders can determine the optimal value of properties by selecting the relevant features.

2. MATERIALS AND METHODS

In our methodology, we utilized the Ames Housing dataset and applied pre-processing techniques to remove noise and handle missing values. Feature engineering techniques were applied to construct additional informative variables. After pre-processing the dataset, we applied various ML and neural network models to achieve the desired predictions. A comprehensive evaluation was conducted using 10-fold cross-validation across multiple ML models, including linear, tree-based, and ensemble methods. The models were assessed using performance metrics such as R^2, RMSE, MAE, MAPE, and RMSLE. Furthermore, weighted averaging and stacking ensemble techniques were applied to improve predictive accuracy, and the best-performing model was identified based on comparative results, as illustrated in Figure1.

2.1. Dataset Description

The Ames Housing Database consists of a detailed information of housing properties in Ames, Iowa, recorded between 2006 and 2010. This particular housing dataset is comprised of 2,930 records, each containing 69 variables that cover a variety of aspects of each property. The features can be organized into various categories, which include information related to general housing attributes such as the type of structure, year of construction, and the overall condition of the house; information about the lot on which the house stands, including the lot size and neighborhood location; size of the

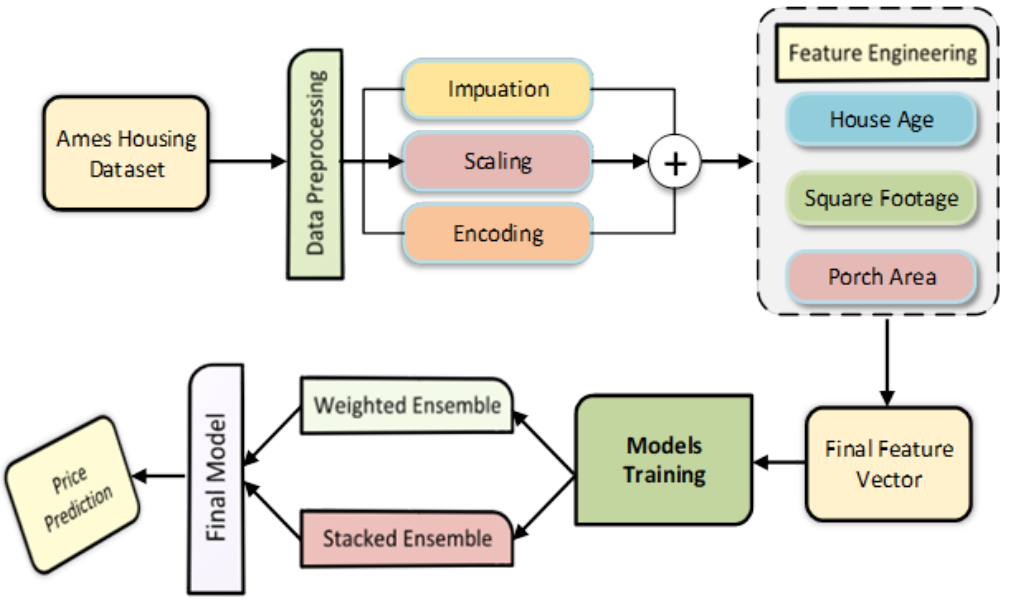

Fig. 1. Proposed Research Methodology.

house and room information; information about structural and exterior material composition of the house; information regarding the garage and basement attributes; amenity information including heating, central air, fireplace, and pool attributes; and time-related information including the month and year of sale.

2.2. Pre-processing

In pre-processing stage, first we examined the missing values and used the Simple Imputer module for handling the missing values by replacing them by median and removed the features like Alley, fence with large proration of missing values. One hot encoding techniques was used to cope the nominal categories such as (Neighborhood, MSZoning) and ordinal encoding technique was used to handle the ordinal variables like (ExterQual, OverallQual) to preserve their rank. Numerical features were standardized to have zero mean and unit variance, and outliers in key features, such as GrLivArea and LotArea, were detected and handled to reduce skewness. The preprocessed data were used for feature engineering to finalize the feature vector which was fed into the ML models for house price prediction.

2.3. Feature Engineering

The feature engineering stage was used to construct composite variables that maintain the overall information regarding property size, usability, and age-related characteristics. In this work, three key features are derived. First, the total square footage is computed by aggregating basement, first-floor, and second-floor areas, from existing feature space and then the total porch area is calculated by aggregating all porch-related spaces, reflecting outdoor living area, which has significant role in property value. A temporal feature is introduced representing age of the house and is being calculated by the difference between the year of sale and the year of construction, which helps model depreciation or appreciation effects over time. These engineered features significantly enhance the model's ability to capture structural and temporal variations in housing prices.

2.4. Final Feature Vector Space

The features were preprocessed, and then the engineered features were added to the feature vector space. This high dimensional feature space is drawn in Figure 2, where housing samples are distributed according to their corresponding price levels, ranging from low to high. To facilitate interpretation, the entire feature space was projected into a two-dimensional embedding using t-SNE, represented by Dimension 1 and Dimension 2. Furthermore, the top 10% high-priced houses were identified and highlighted based on the dataset features, particularly housing size and related structural attributes.

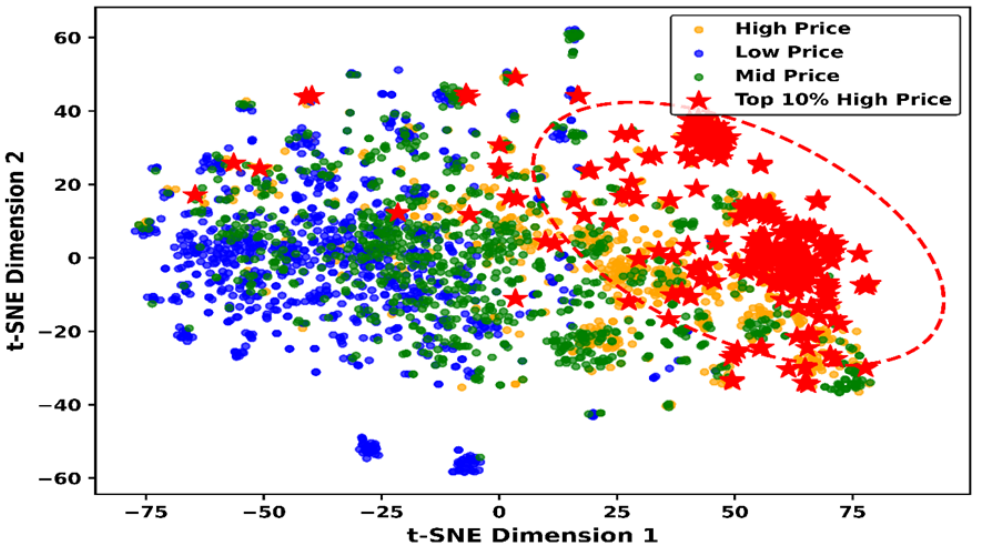

Fig. 2. Final Feature Vector Space Visualization.

2.5. Model Training and Testing

In the model selection phase, we conducted extensive experiments with a variety of classifiers, including Linear Regression, James *et al*. [13] and Shbool *et al*. [14]; Ridge, Lasso, Decision Tree, Random Forest, Breiman [15]; hybrid model porcupine and BP neural network, Hong and Li [16], Gradient Boosting and XGBoost, Hong and LightGBM, Himanshu [17], and neural network, Wijaya [18]. Additionally, we investigated the various fusion approaches such as weighted and stacked ensemble methods, to find and select the suitable model for real estate price prediction.

Model evaluation is conducted using a 10-fold cross-validation strategy to ensure generalization and avoid overfitting. Out-of-fold predictions are generated using cross_val_predict, allowing unbiased performance estimation on unseen data without requiring a separate hold-out test set. Multiple evaluation metrics are employed, including R^2, adjusted R^2, RMSE, normalized RMSE, MAE, MAPE, and RMSLE, providing a holistic assessment of model performance both in original and log-transformed scales.

2.6. Proposed Stacking Ensemble

The three gradient boosting algorithms of XGBoost, CatBoost and LightGBM are used as our base learners. The two-level stacking ensemble of a Ridge regression with meta-learner (with $\alpha = 1.0$) to enhance the stability of the predictions. The target variable is log-transformed ( ) to reduce the skewness. Preprocessing: Median imputation for numeric features, most frequent imputation for categorical, and feature engineering (TotalSF, TotalPorchSF, and HouseAge). To avoid data leakage, out-of-fold predictions from stratified 10-fold cross validation are used as meta-features. Base models are then retrained using the complete training set, and predictions are then inverse-transformed. The entire process is summarized in Algorithm 1.

3. RESULTS AND DISCUSSION

This section presents the detailed experimental results obtained from various ML models on Ames housing datasets. The model's performance was evaluated based on 10-fold cross validation strategy and assessed through various performance parameters including coefficient of determination (R^2), root mean squared error (RMSE), root mean squared logarithmic error (RMSLE), mean absolute error (MAE), mean absolute percentage error (MAPE). We also performed various statistical test including paired t-test and Wilcoxon signed-rank test were conducted on cross-validated predictions to validate the top model's performance.

3.1. Individual Model Performance with Base Dataset

To determine the contribution of individual models for real state price predication, all nine models were trained and tested with same cross validation

Algorithm 1. Pseudocode for Stacking Ensemble with Ridge Meta-Learner.

```
Input: X, y = log1p(SalePrice), K = 10
Output: y_pred
Xp ← preprocess(X)
base_models ← [XGBoost, CatBoost, LightGBM]
Z_train ← hstack([cross_val_predict(m, Xp, y, K) for m in base_models])
ridge_model ← Ridge.fit(Z_train, y, alpha=1.0)
fitted_models ← [fit(m, Xp, y) for m in base_models]
Xp_new ← preprocess(X_new)
Z_test ← hstack([m.predict(Xp_new) for m in fitted_models])
y_pred ← expm1(ridge_model.predict(Z_test))
return y_pred
```

technique and the results are presented in Table 1. In this experiment we only used preprocessed dataset without including engineering features as total square footage, total porch area and the age of the house.

We compared the performance of basic ML and ensemble models as illustrated in Table 1 for house price predication and evaluated based on R^2, adjusted R^2, RMSE, NRMSE, and MAPE. A significant variation was observed between traditional ML models and ensemble models. When comparing the R^2 values, XGBoost showed the best performance with a value of 0.9298, followed closely by CatBoost with 0.9293, LightGBM of 0.9225 and Gradient Boosting at 0.9188. On the other hand, random forest outperformed with R^2 of 0.8897 from traditional ML models and the linear regression achieved minimum R^2 of 0.3331. The same behavior was observed for all models from other evaluating parameters including NRMSE, adjusted R^2 and MAPE. The results demonstrate that ensemble-based machine learning models consistently outperform traditional machine learning methods for real estate price prediction tasks.

3.2. Individual Models Performance Based on Engineered Features

To investigate the impact of feature engineering on real state price prediction, we introduced three new features including total square footage area, porch area and the age of the house and append these features with our base dataset. We trained our base models again with the updated dataset with same data spilt strategy and used same evaluation parameters. The performance of each model both

Table 1. Models Comparison based R^2, Ajd.R^2, RMSE ($), NRMSE and MAPE (%) with Base Dataset.

Model	R^2	Adj. R^2	RMSE ($)	NRMSE	MAPE (%)
XGBoost	0.9298	0.9211	21164.54	0.1171	7.78
CatBoost	0.9293	0.9206	21244.21	0.1175	7.66
LightGBM	0.9225	0.9130	22233.90	0.1230	8.10
Gradient Boosting	0.9188	0.9088	22755.76	0.1259	8.16
Random Forest	0.8897	0.8761	26524.85	0.1467	9.63
Decision Tree	0.8175	0.7951	34119.27	0.1887	13.12
Ridge	0.7086	0.6728	43113.93	0.2385	8.93
Lasso	0.6296	0.5840	48613.34	0.2689	9.16
Linear Regression	0.3331	0.2511	65225.98	0.3608	9.51

from traditional ML models and ensemble models is improved and the CatBoost achieved the maximum R^2 of 0.9312 as shown in Table 2 which was improved from base dataset as presented in Table 1. Similar pattern was observed from others models and again the ensemble models performed better while comparing with the traditional ML models.

3.3. Hybrid Models Performance Based on Final Feature Vector

We employed hybrid modeling strategies to assess global predictive performance using two distinct ensemble approaches. In the first approach, the top three high-performing models CatBoost, XGBoost, and LightGBM were combined, as they share similar boosting-based architectures and demonstrated superior individual performance. In the second approach, we introduced architectural diversity by integrating a traditional ensemble model, Random Forest, with CatBoost. This combination was designed to balance bias variance, where Random Forest contributes to variance reduction while CatBoost enhances predictive accuracy through gradient boosting.

The results from the experiments presented in Figure 3 indicate that the stacking ensemble method with a Ridge meta-learner outperforms while comparing with other approaches. The best predictive performance comes from a weighted averaging ensemble (R^2 = 0.9334) followed by the best average (R^2 = 0.9330). The Random Forest and CatBoost hybrid combination has a comparative score of 0.9313, which is lower than the other models. The advantages of stacking can be explained by the fact that this system can learn optimal combinations. Uses a meta-learner to adjust base model predictions instead of a fixed or manually assigned weights. This enables stacking to be very effective at capturing complementary strengths and minimizing individual model biases with better generalization ability. In contrast, weighted averaging assumes a static contribution from each model, while the Random Forest–CatBoost combination may suffer from reduced diversity due to overlapping boosting-based learning behavior, limiting its overall variance reduction effectiveness.

The results based on RMSLE as illustrated in Figure 4, indicate that the stacking ensemble with a Ridge meta-learner achieves the lowest prediction error 0.1132, followed closely by the weighted averaging ensemble 0.1138, while the Random Forest with CatBoost hybrid combination shows comparatively higher error 0.1211. This demonstrates that stacking provides better generalization by effectively learning an optimal combination of base model predictions, whereas

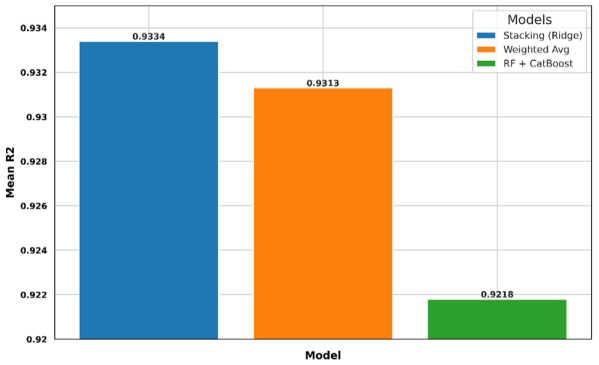

Fig. 3. R^2 performance comparison for hybrid (stacking and weighted averaging) ensemble methods.

Table 2. Models Comparison based R^2, Ajd.R^2, RMSE ($), NRMSE and MAPE (%) with new Features.

Model	R^2	Adj. R^2	RMSE ($)	NRMSE	MAPE (%)	RMSLE
CatBoost	0.931209	0.922653	20,949.09	0.11587	7.6383	0.11393
XGBoost	0.929067	0.920244	21,272.86	0.11766	7.7443	0.11519
LightGBM	0.922117	0.912430	22,290.61	0.12329	8.0257	0.11951
Gradient Boosting	0.921036	0.911215	22,444.73	0.12414	8.1217	0.11992
Random Forest	0.898268	0.885615	25,475.89	0.14091	9.5320	0.13735
Decision Tree	0.804418	0.780092	35,323.62	0.19538	13.0818	0.18681
Ridge	0.707936	0.671611	43,165.72	0.23875	8.9255	0.13566
Lasso	0.625607	0.579041	48,872.49	0.27032	9.1611	0.13831
Linear Regression	0.334176	0.251364	65,174.83	0.36049	9.5098	0.15828

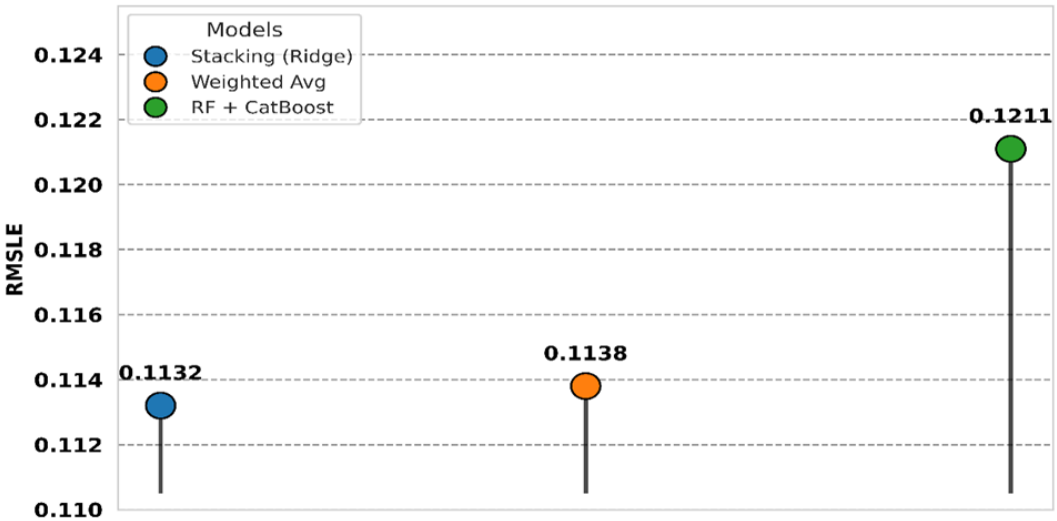

Fig. 4. RMSLE performance comparison for hybrid (stacking and weighted averaging) ensemble methods.

weighted averaging applies fixed contributions and may not capture model complementarities. The relatively higher error in the Random Forest and CatBoost ensemble suggests limited diversity in data.

3.4. Statistical Evaluation of Best Performing Models

To evaluate the robustness and stability of the best performing models (CatBoost, XGBoost, and LightGBM) we performed the statistical evaluation and used two strategies paired t-test and Wilcoxon signed ranked test. To investigate the statistical significance of best performing model, paired test was employed on their predictive results. As presented in Figure 5, the predictive results are comparable for the models XGBoost and CatBoost (0.9470); and XGBoost and LightGBM (0.0970), as these models are not statistically significant with minimum margin of difference in their predication. However, the comparison between CatBoost and LightGBM ($p = 0.0363$) reveals a statistically significant difference, suggesting a measurable performance gap between these two models as presented in Figure 5.

Similarly, the Wilcoxon signed-rank test was applied to the best-performing models to assess the median differences in their predictive results without assuming normality. The statistical comparison as shown in Figure 6, varying levels of difference among the evaluated models. The highest p-value corresponds to the comparison between XGBoost

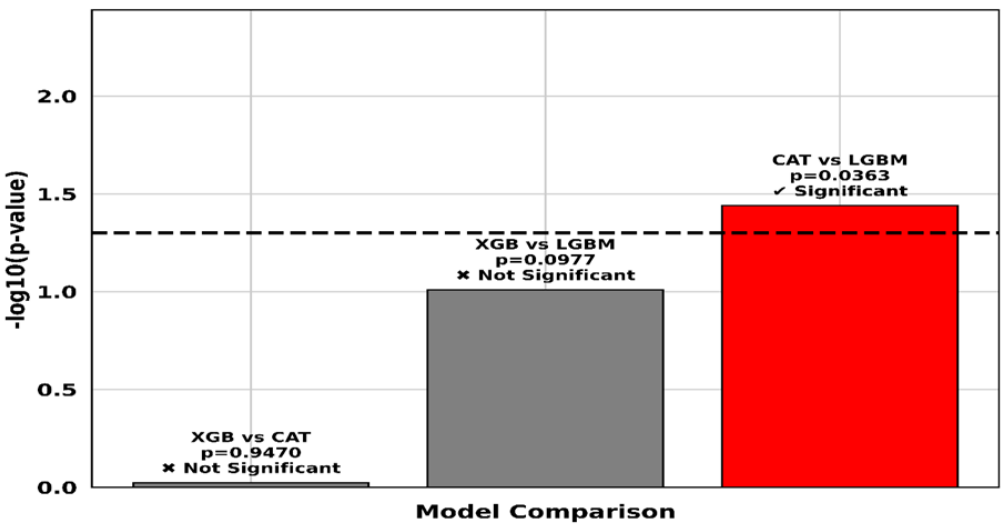

Fig. 5. Paired T-Test analysis of best performing ensemble models.

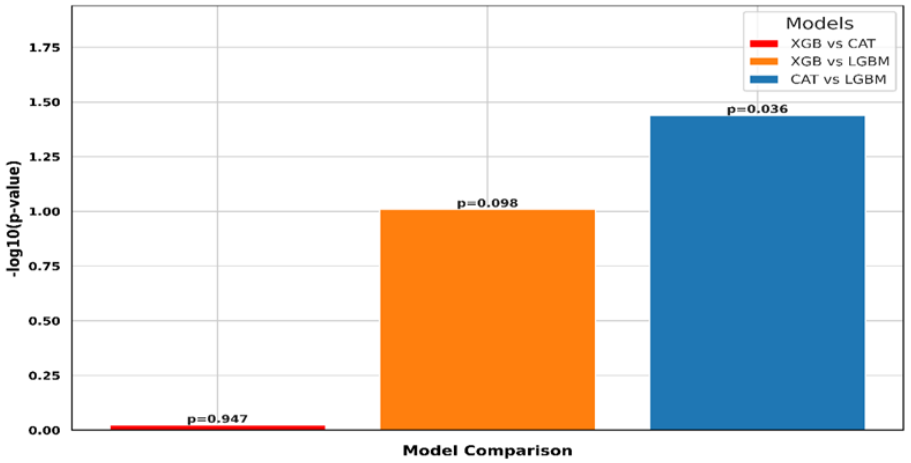

Fig. 6. Wilcoxon singed ranked analysis of best performing ensemble models.

and CatBoost, indicating minimal difference and highly similar performance between the two models.

In contrast, the comparison between CatBoost and LightGBM shows a statistically significant difference, suggesting a consistent performance gap. The intermediate comparison between XGBoost and LightGBM reflects a moderate difference that is not statistically significant. Overall, these findings indicate that while most models exhibit comparable predictive behavior, certain model pairs demonstrate meaningful variations that are supported by statistical evidence.

Based on our extensive experiments, we investigated that tree-based ensemble models perform better as compared to traditional machine learning models. Moreover, it was also observed that model performance is enhanced by adding suitable features in the base dataset. The predictive results improved further through model fusion, and by using stacking techniques, the proposed model outperformed and achieved the best results. Furthermore, the statistical analysis confirms that most ensemble model comparisons are not significantly different, indicating minimal variation in predictive performance, with only specific model pairs showing statistically significant differences.

3.5. Discussion

The results indicate that proposed stacked ensemble model achieved the maximum accuracy on the Ames Housing dataset, with an R^2 score of 0.9334, RMSLE of 0.1132, NRMSE: 0.1140 and MAPE: 7.58% and RMSE (20606.16 $). The performance of our stacking model was improved by introducing new features in the base dataset. This performance significantly outperforms several existing models reported in the literature. The XGBoost model proposed by Kumar *et al*. [11] and model achieved the R^2 of approximately 0.923 RMSE of (24630.91 $) and our model outperformed while comparing it as shown in Table 3.

Similarly, the Random Forest model was employed by Zhao [12] on Ames dataset and the model achieved the performance with an R^2 of 0.85and RMSE of 24630.91$. The performance of the model is comparably low as our proposed model. Another research study proposed by

Table 3. Proposed model comparison with other models.

Papers	DATASETS	Models	R^2	RMSLE	RMSE ($)
Proposed Method	Ames Housing	CXL Stacked	0.9334	0.1132	20606.16
Kumar *et al*. [11]	Ames Housing	XGBoost	0.923	----	24630.91
Zhao [12]	Ames Housing	Random Forest	0.85	-----	3536
Han [10]	Ames Housing	Stacked Model	-----	0.1189	-----
Ye [19]	Ames Housing	XGBoost	0.88	0.1249	30718.06

Han [10] utilized a stacked ensemble model and achieved an RMSLE of 0.1249, demonstrating a competitive performance compared to our model as illustrated in Table 3. The research based on XGBoost proposed by Ye [19] on the Ames dataset achieved an R^2 of 0.88, an RMSLE of 0.1249, and an RMSE of 30718.06 $. Based on this comparison, our model outperformed the existing approach, as we introduced enhanced feature engineering along with a stacking strategy for effective model fusion. The proposed CXL ensemble method, which combines the predication of CatBoost, XGBoost, and LightGBM and used ridge regression as meta-learner and model achieved the best an RMSLE of 0.1132 and an R^2 score of 0.9334. This improvement highlights the effectiveness of advanced feature engineering combined with a stacked ensemble approach in enhancing model performance. By transforming and enriching the original features, and leveraging multiple models through stacking, the proposed method captures complex patterns more effectively while reducing over fitting.

4. CONCLUSIONS

The proposed study demonstrates the integration of new features with CXL ensemble model significantly improve the performance of house price prediction The CXL ensemble model combing the (CatBoost, XGBoost, and LightGBM) with ridge regression as meta-learner improved the performance and the model achieved the best RMSLE of 0.1132 and an R^2 score of 0.9334 as compared to existing approaches. The robustness and reliability of our model were ensured through Wilcoxon singed ranked and T-paired test and it the ensemble based model shown minimum variation for the predication performance, demonstrating its stability and consistency in house price prediction. For future work, the framework can be extended to larger and more diverse datasets while integrating explainable AI (XAI) techniques to enhance interpretability and provide actionable insights.

5. CONFLICT OF INTEREST

Authors declare no conflict of interest.

6. FUNDING

No funding was received to conduct this research.

7. AUTHORSHIP CONTRIBUTION STATEMENT

Muhammad Khateeb Khan was responsible for the conception of the methodology, model development, experimental analysis, and presentation of results; Asad Ullah Khan originated the initial study idea and performed data collection; Salman Ahmed and Wajid Ali jointly conducted the literature review and led the manuscript writing, review, and proofreading. All results, analyses, and interpretations were conducted by the authors; Grammarly and Google Translate were used for English language refinement.

8. ETHICAL STATEMENT

In the present study no human or animal subjects are involved; therefore, ethical approval is not required.

9. REFERENCES

1. S. Buyrukoglu and O.G. Uzut. Prediction of real estate prices with data mining algorithms. *Euroasia Journal of Mathematics, Engineering, Natural & Medical Sciences* 7(9): 77-84 (2020). https://www.researchgate.net/publication/342782159_Prediction_of_real_estate_prices_with_data_mining_algorithms
2. H. Ding. Predicting Boston housing prices using machine learning models. *Proceedings of the 2024 2nd International Conference on Management Innovation and Economy Development (MIED 2024)*, *Advances in Economics, Business and Management Research*. *Atlantis Press* (2024). https://doi.org/10.2991/978-94-6463-542-3_51
3. D. Harrison and D.L. Rubinfeld. Hedonic housing prices and the demand for clean air. *Journal of Environmental Economics and Management* 5(1): 81-102 (1978). https://doi.org/10.1016/0095-0696(78)90006-2
4. W. Xibin, J. Wen, Y. Zhang, and Y. Wang. Real estate price forecasting based on SVM optimized by PSO. *Optik* 125(3): 1439-1443(2014). https://doi.org/10.1016/j.ijleo.2013.09.017
5. S.M. Lundberg, G.G. Erion, and S.I. Lee. Consistent individualized feature attribution for tree ensembles. *Proceedings of the 22nd International Conference on Artificial Intelligence and Statistics* 2018: 13-27 (2018). https://arxiv.org/abs/1802.03888
6. D.E. Aniobi, C.O. Ochuba, and S.B. Nguideen. House price prediction: *Comparative analysis of regression-based machine learning algorithms.*

International Journal for Research in Applied Science & Engineering Technology 11(X): 1550 (2023). https://doi.org/10.22214/ijraset.2023.56232

7. S.C.K. Tekouabou, Ş.C. Gherghina, E.D. Kameni, Y. Filali, and K.I. Gartoumi. AI-Based on Machine Learning Methods for Urban Real Estate Prediction: A Systematic Survey. *Archives of Computational Methods in Engineering* 31(2): 1079-1095 (2024). 10.1007/s11831-023-10010-5
8. Y. Chen. Research on the prediction of Boston house price using various models. *Highlights in Business, Economics and Management* 21: 27-37 (2023). https://doi.org/10.54097/hbem.v21i.13600
9. S. Muralidharan, K. Phiri, S.K. Sinha, and B. Kim. Analysis and prediction of real estate prices: A case of the Boston housing market. *Issues in Information Systems* 19(2): 109-118(2018). https://doi.org/10.48009/2_iis_2018_109-118
10. Y. Han. Price Prediction of Ames Housing Through Advanced Regression Techniques. *BCP Business & Management* 38: 1965-1974 (2023). https://doi.org/10.54691/bcpbm.v38i.4014
11. M.S. Kumar, M. Saraswathi, B.Y. Singh, D. Divya, and J.S. Shanker. An Efficient and Interpretable XGBoost Framework for Housing Price Prediction: Enhancements in Accuracy and Computational Performance. *International Journal of Computer Engineering Research and Trends* 11(1s): 23-30 (2024). https://www.ijcert.org/index.php/ijcert/article/view/1041/900
12. T. Zhao. Predicting House Prices Using Machine Learning Models. *Transactions on Computer Science and Intelligent Systems Research* 9: 629-633 (2025). https://doi.org/10.62051/e9x5cc73
13. G. James, D. Witten, T. Hastie, and R. Tibshirani (Eds.). An introduction to statistical learning: With applications in R. *Springer* (2013). https://static1.squarespace.com/static/5ff2adbe3fe4fe33db902812/t/6009dd9fa7bc363aa822d2c7/1611259312432/ISLR+Seventh+Printing.pdf
14. M.A. Shbool, R. Al-Dmour, B.A. Al-Shboul, N.T. Albashabsheh, and N. Almasarwah. Real estate decision-making: precision in price prediction through advanced machine learning algorithms. *International Journal of Housing Markets and Analysis* 19(3): 771-795 (2026). https://doi.org/10.1108/IJHMA-01-2025-0004
15. L. Breiman. Random forests. *Machine Learning* 45(1): 5-32 (2001). https://doi.org/10.1023/A:1010933404324
16. Q. Hong and H. Li. Prediction of house price in Boston based on the fusion of crested porcupine optimizer algorithm and BP neural network. In: *Proceedings of the 2025 International Conference on Digital Economy and Information Systems (DEIS '25), Association for Computing Machinery, New York, NY, USA* pp. 247-252 (2025). https://doi.org/10.1145/3745133.3745175
17. S. Himanshu. Benchmarking Predictive Performance of Machine Learning Approaches for Accurate Prediction of Boston House Prices: An In-Depth Analysis. *International Journal of Advanced Research and Interdisciplinary Scientific Endeavours* 1(2): 78-91 (2024). DOI: 10.5281/zenodo.13841369
18. R. Wijaya. Multi-level dense layer neural network model for housing price prediction. *arXiv preprint arXiv:*2310.08133v1 (2023). https://arxiv.org/pdf/2310.08133
19. Q. Ye. House price prediction using machine learning for Ames, Iowa. *Applied and Computational Engineering* 55: 44-54 (2024). https://doi.org/10.54254/2755-2721/55/20241483

Proceedings of the Pakistan Academy of Sciences: A Physical and Computational Sciences 63(2): 133-146 (2026)

ISSN (Print): 2518-4245; ISSN (Online): 2518-4253
http://doi.org/10.53560/PPASA(63-2)717

Pakistan Academy of Sciences

Research Article

Homo- and Heteroleptic Cd(II) 4-Phenylbutyrates, Synthesis, Exploration of Chemistry, DNA Binding Study and Antileishmanial Activity

Aneeqa Sharif[1], Saba Naz[1], Saqib Ali[1*], Ali Haider[1], Sammar Yousuf[2,3], and Mahboob-ur-Rehman[4]

[1]Department of Chemistry, Quaid-i-Azam University, Islamabad, 45320, Pakistan
[2]H.E.J. Research Institute of Chemistry (International Center for Chemical and Biological Sciences) University of Karachi, Karachi-75270, Pakistan
[3]Institute of Molecular Biology and Biotechnology, University of Lahore, Lahore, Pakistan
[4]Department of Cardiology, Pakistan Institute of Medical Sciences (PIMS), Islamabad, Pakistan

Abstract: By using 4-phenylbutyric acid (4-PBA) and aromatic nitrogen heterocycles, i.e., 2,2′-bipyridine (BIPY), 1,10-phenanthroline (PHEN), and 2,9-dimethyl-1,10-phenanthroline (Me_2PHEN) as ancillary ligands, four cadmium carboxylates were synthesized. The chemistry and biological applications of the homoleptic complex are discussed for the 4-PB1, whereas the heteroleptic complexes containing BIPY, PHEN, and Me_2PHEN are designated as 4-PBB, 4-PBP, and 4-PBD, respectively. Their synthesis and chemistry were explored fully through FT-IR and NMR (^{1}H and ^{13}C) spectroscopy. The FT-IR data in the solid state show the metal coordination with the ligand moieties, where the carboxylate group adopted multi-mode coordination. The absence and presence of resonance signals, along with characteristic multiplicity in the solution ^{1}H as well as ^{13}C NMR data, confirm targeted synthesis. The assessment of the synthesized complexes for their binding ability with DNA was executed through multiple techniques, including UV-Vis absorption spectroscopy, viscometry, and cyclic voltammetry. The findings from all techniques support that the complexes interact with DNA through a dual mode of binding following a smooth process. The complex having an attached phenanthroline was found to be active in all attributed to its increased planar area and availability of bonding interactions. The antileishmanial study reveals that the synthesized complexes exhibit good to moderate activity against the amastigotes of *L. tropica* as compared to the standard drug used in the study.

Keywords: Homo- and Heteroleptic Carboxylates, Chelating Bidentate, Salmon Sperm DNA, Cyclic Voltammetry, *Leishmaniasis Tropica Promastigotes*, Gelardin's Strain.

1. INTRODUCTION

The burden of disease in terms of tropical and major non-communicable diseases is a big cause of hurdles for humans all over the world. The people belonging to the less developed countries are severely suffering from the neglected tropical disease, i.e., Leishmaniasis, also known as the disease of the poor. It is a parasitic infection caused by the bite of infected sandflies [1, 2]. On the other hand, cancer, the exact cause of which is still unknown, remains a big reason for mortality worldwide, affecting both developed and less developed countries alike. A prediction indicates that 16.3 million cases, which would be related to cancer and 29.5 million cases would be new by the time 2040 [3]. Despite global efforts by the healthcare sector to address this issue, the combined socioeconomic burden and adverse effects of currently in use drugs for cancer and leishmaniasis remain challenging. The fact

Received: April 2026; Revised: May 2026; Accepted: June 2026
* Corresponding Author: Saqib Ali <saqibali@qau.edu.pk>

that the well-known anti-cancer metallodrug cis-platin is active on account of its ability to interact with DNA motivates researchers in this direction [4]. The literature study reveals that DNA is the common target of the drugs used against cancer and many other communicable or non-communicable diseases [5].

There is a growing trend to modify the already in-use drug for the targeted response. The well-known example is the structural modification of the NSAIDs. This trend encourages the use of carboxylic acid as a ligand in the manufacture of metal-based therapeutics. The reason behind this is that the carboxylic acid is found to be an essential structural component of the majority of drugs. Besides this, the other structural and electronic characteristics of the carboxylic acids are well-suited for the biological system. Their ability to adopt a multi-coordination mode is considered important for getting interesting geometries that are well-matched to the biomacromolecules [6, 7]. The 4-phenylbutyric acid is an expectedly good choice in this regard, which already plays a significant biological role in plants by acting as a chemical binder [8]. It is prescribed to children to treat urea cycle disorder by scavenging ammonia, to cure inflammation, and mental disorders.

Being inspired by the biomacromolecule, the use of nitrogen heterocycles as auxiliary ligands alongside the carboxylic acid is a current research focus of scientists in the field of bioinorganic chemistry. The aromatic ring results in extended π systems, which could develop various non-covalent interactions [9]. This strategy results in a structure that could mimic the biomacromolecules and hence can compete and survive in the biological systems. The incorporation of the nitrogen heterocycle into the in-use drugs like furosemide and coumarin derivatives results in enhanced targeted results. Here, both the carboxylic acid and nitrogen heterocycles work together as primary and auxiliary ligands and result in fascinating topological and biological characteristics [10, 11]. Alongside this, the smart selection of the metal center matters a lot. Cadmium, a delicate, silvery-white metal with the atomic number 48 symbol Cd from Group 12, shares chemical similarities with zinc. It possesses fascinating chemistry and is capable of adopting various coordination geometries [12]. Cadmium can produce reactive oxygen species (ROS), alter mitochondrial potential and activate caspase enzymes, all of which combine to kill cancerous cells with minimal impact on healthy cells [13]. Additionally, recent research is investigating the use of quantum dots, targeted drug delivery, and nanoparticles based on cadmium [14]. Besides all this, the related toxicity is its weak point, which, however, could be compensated by complexation with suitable donor ligands, especially oxygen and nitrogen [15]. The Lewis acidity of the Cd(II) makes it quite useful in a number of catalytic processes. The coordination versatility makes it applicable in sensors. Its ability to adopt fascinating topological features results in the generation of structural frameworks when combined with suitable ligands and is used for the storage of gaseous or solid materials [16].

The study reveals that this kind of ligand and metal combination produces fascinating results in term of structure and application. The mixed ligand Cd(II) carboxylates derived from the substituted phenylacetic and nitrogen heterocycles show enhance binding with DNA as compare to relevant ligand and homoleptic carboxylates [15]. The coordination flexibility of the cadmium(II) and carboxylate group together with the nitrogen heterocycles leads to interesting and stable topological arrangements known “Chinese lantern” [17]. Similarly, 1D and 2D polymeric structural framework was observed for Cd(II) complexes as a consequence of coordination of nitrogen donor ancillary ligands and show interesting application as sensors [18]. The Cd(II) based mixed ligand carboxylates derived from the cyclic carboxylic acids show efficient ability to bind with DNA [19]. Taking into consideration the significant role of carboxylic acid and nitrogen heterocycles as ancillary ligands to modify the structure and hence applications, herein, homo- and heteroleptic carboxylates were synthesized. Their synthesis in pure form, followed by complete spectroscopic characterization, was carried out. Their DNA-binding ability was assessed through multiple techniques. They were also tested for their ability to act as an antileishmanial agent.

2. MATERIALS AND METHODS

The chemicals used during synthesis are 4-phenylbutyric acid, sodium bicarbonate, cadmium(II) nitrate, 2,2′-bipyridine,

1,10-phenanthroline, and 2,9-dimethyl-1,10-phenanthroline shown in Scheme 1. These chemicals were acquired from Aldrich, Fluka and Alfa-Aesar (Johnson Matthey); They were analytical grade and utilized as supplied without further purification. The solvents, i.e., methanol, ethanol, chloroform, acetone, and dimethyl sulphoxide (DMSO), were of analytical grade and obtained from Germany's Merck. The Gallenkamp electrothermal apparatus was used to determine melting points, which is manufactured in the UK. For the samples in solid state, the FT-IR data were recorded using a Bruker TENSOR II (Germany) spectrophotometer in the 4000–400 cm^{-1} range. The NMR (^{1}H and ^{13}C) behavior was investigated using a 300 MHz Bruker Advanced Digital NMR instrument. The electronic spectra were recorded using the Shimadzu 1800 UV-Visible spectrophotometer. A Corrtest CS 300 (Potentiostat/Galvanostat) Electrochemical Workstation, manufactured in China, was used to collect the record of the voltammograms.

2.1. Synthesis

2.1.1. Synthesis of sodium salt of ligand acid

The sodium bicarbonate aqueous solution (3 mmol, 0.252 g) was added gradually to the methanolic solution of 4-phenylbutyric acid (3 mmol, 0.498 g). The solution was continuously agitated at room temperature to prepare sodium salts of the respective acid. Stirring was continuous until neutralization. The solid product was obtained by evaporating the solvents under low pressure. The synthesis route is shown in Scheme 2.

2.1.2. Synthesis of homoleptic complex (4-PB1)

The synthesis route for 4-PB1 is shown in Scheme 3. Methanolic solutions of ligand sodium salt, 4-PBNa (3 mmol, 0.558 g), were added to an aqueous solution of Cd(II) nitrate (1.5 mmol, 0.355 g) and stirred continuously for seven to eight hours at 50 °C. The reaction mixtures were filtered off, and the solvent was evaporated using a rotary evaporator to obtain the solid products.

[Cd(4-PBA)$_2$] (4-PB1)
Yield = 67%; Physical state: white powder solid; M.P. = 250-253 °C; FT-IR (4000–400 cm^{-1}): 1546 (COO^{-}_{asymm}); 1398 (COO^{-}_{symm}), 148 (Δν), 462 (Cd-O); ^{1}H NMR (in DMSO): 2.10-2.15 (t, 4H, H2, J = 7.5 Hz), 1.73-1.83 (quint, 4H, H3, J = 7.2 Hz), 2.49-2.61 (m, 4H, H4), 7.13-7.29 m (m, 10H, H6, 6′, H7,7′, H8); ^{13}C NMR (in DMSO): 180.3 (C1), 35.3 (C2), 28.4 (C3), 34.6 (C4), 142.6 (C5), 128.8 (C6, 6′), 128.6 (C7, 7′), 126.0 (C8).

2.1.3. Synthesis of heteroleptic complexes (4-PBB, 4-PBP, and 4-PBD)

Heteroleptic carboxylates synthesis was done using the same method as 4-PB1. The only exception was that 1.5 mmol ethanolic solutions of 2,2'-bipyridine, 1,10-phenanthroline, and 2,9-dimethyl-1,10-phenanthroline were added during continuous stirring at 50 °C along with cadmium (II) nitrate to synthesize 4-PBB, 4-PBP, and 4-PBD, respectively. After filtering the resultant solutions and using rotary evaporation to eliminate excess solvents, the solid products were repeatedly cleaned with water

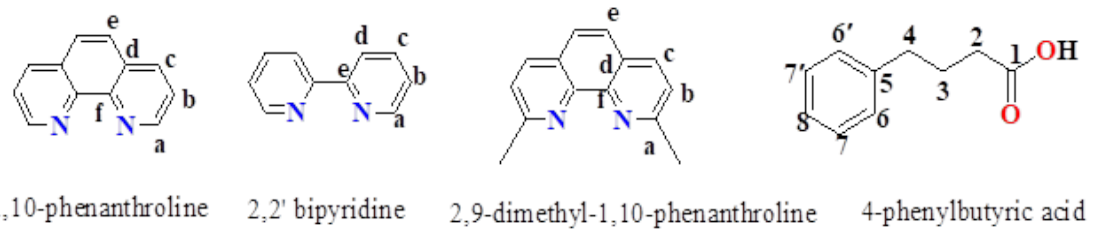

Scheme 1: Ligands structures used in synthesis, numbered for NMR analysis.

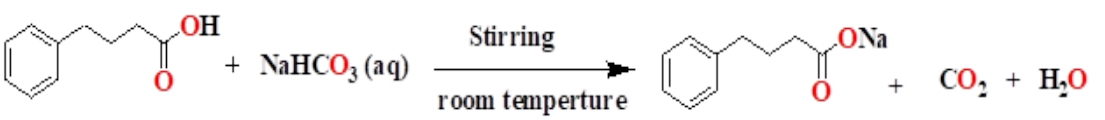

Scheme 2: Synthetic route for the sodium salt of 4-phenylbutyric acid (4-PBNa).

and allowed to air dry. The resulting compounds were recrystallized using a mixture of suitable solvents. All of the synthesized complexes' melting points were noted. Scheme 3 shows the synthesis pathway for complexes.

[Cd(4-PBA)$_2$(BIPY)] (4-PBB)

Yield = 73%; Physical state: white crystalline solid; M.P. = 123-125 °C; FT-IR (4000–400 cm^{-1}): 1550 (COO^-_{asymm}); 1407 (COO^-_{symm}), 143 (Δν), 420 (Cd-O), 533 (Cd-N), 763 $(C\text{-}H)_{out\ of\ plane}$; ^{1}H NMR (in $CDCl_3$): 2.31-2.36 (t, 2H, H2, J = 7.2 Hz), 1.85-1.95 (quint, 2H, H3, J = 8.1 Hz), 2.53-2.58 (t, 2H, H4, J = 7.5 Hz), 7.19-7.28 (m, 2H, H6, 6′), 7.09-7.16 (m, 3H, H7,7′, H8) ,8.92-8.94 (m, 1H,Ha), 7.48-7.53 (m, 1H, Hb), 7.94-7.99 (td, 1H, Hc, J = 1.8, 7.8 Hz), 8.12-8.14 (d, 1H, Hd, J=8.1); ^{13}C NMR (in $CDCl_3$): 182.6 (C1), 35.6 (C2), 28.1 (C3), 35.0 (C4), 128.5 (C5), 128.1 (C6, 6′), 126.1 (C7, 7′), 121.4 (C8), 149.6 (Ca), 125.5 (Cb), 139.6 (Cc), 142.3 (Cd), 150.5 (Ce).

[Cd(4-PBA)$_2$(PHEN)] (4-PBP)

Yield = 85%; Physical state: white crystalline solid; M.P. = 179-180 °C; FT-IR (4000–400 cm^{-1}): 1554 (COO^-_{asymm}); 1409 (COO^-_{symm}), 145 (Δν), 427 (Cd-O), 566 (Cd-N), 849, 728 $(C\text{-}H)_{out\ of\ plane}$; ^{1}H NMR (in $CDCl_3$): 2.49-2.57 (m, 6H, H2, H8), 1.85-1.93 (quintet, 4H, H3, J = 8.1 Hz), 2.30-2.36 (t, 4H, H4, J = 7.2 Hz), 7.07-7.21 (m, 10H, H6,6′, H7,7′), 9.11-9.14 (dd, 2H, Ha, J = 7.8, 1.8), 7.71-7.75 (m, 2H, Hb), 8.39-8.42 (dd, 2H, Hc, J = 1.5, 8.1Hz), 7.90 (s, 2H, He′); ^{13}C NMR (in $CDCl_3$): 182.4 (C1), 35.6 (C2), 28.2 (C3), 35.2 (C4), 128.4 (C5), 128.1 (C6, 6′), 125.5 (C7, 7′), 124.8 (C8), 150.4 (Ca), 126.9 (Cb), 141.2 (Cc), 138.6 (Cd), 129.0 (Ce), 142.3 (Cf).

[Cd(4-PBA)$_2$(Me$_2$PHEN)] (4-PBD)

Yield = 83%; Physical state: brown crystalline solid; M.P. = 156-158 °C; FT-IR (4000–400 cm^{-1}): 1548 (COO^-_{asymm}), 1410 (COO^-_{symm}), 138 (Δν), 418 (Cd-O); 550 (Cd-N), 859, 731 $(C\text{-}H)_{out\ of\ plane}$; ^{1}H NMR (in $CDCl_3$): 2.37-2.42 (t, 4H, H2, J = 7.2 Hz), 1.93-2.03 (quint, 4H, H3, J = 8.1 Hz), 2.60-2.66 (t, 4H, H4, J = 7.5 Hz), 7.10-7.28 (m, 10H, H6,6′, H7,7′, H8), 7.70-7.72 (d, 1H, Hb, J = 8.4 Hz), 8.33-8.36 (d, 2H, Hc, J = 8.1 Hz), 7.84 (s, 2H, He), 3.19 (s, 6H, H_{Methyl}); ^{13}C NMR (in $CDCl_3$): 182.7 (C1), 35.7 (C2), 28.3 (C3), 34.6 (C4), 128.1 (C5), 127.3 (C6, 6′), 126.1 (C7, 7′), 125.5 (C8), 161.2 (Ca), 125.9 (Cb), 140.6 (Cc,), 139.0 (Cd), 128.5 (Ce), 142.3 (Cf), 25.5 (C_{Methyl}).

2.2. DNA Binding Behavior through UV-Visible Spectroscopy

In 100 milliliters of deionized water, 20 milligrams of lyophilized powder of sodium salt of salmon

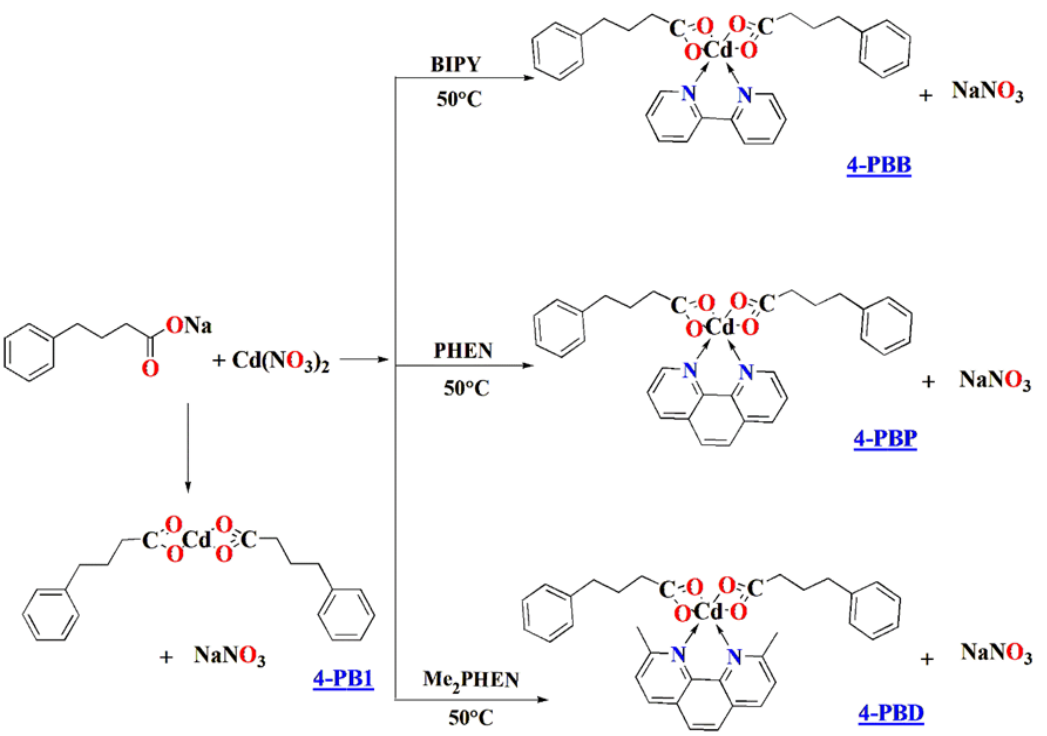

Scheme 3: Synthetic routes for complexes 4-PB1, 4-PBB, 4-PBP, and 4-PBD.

sperm were dissolved for roughly 24 hours while being continuously stirred. The DNA sample was found to be pure, with an absorption ratio (260/280) of 1.68, corresponding to a DNA concentration of 166 μM. Ethanol was used as a solvent for the ligand 4-PBA and relevant complexes 4-PB1, 4-PBB, 4-PBP, and 4-PBD. The absorption spectra were recorded at different DNA concentrations, with the ligand and complexes at a fixed concentration. To counteract the DNA absorption effect, the reference and sample cells were having same amount of DNA throughout the experiments. The compound-DNA solution was incubated for roughly ten minutes following each addition, then the spectra were recorded [20].

2.3. DNA Binding Behavior through Cyclic Voltammetry

Using 0.1M TBAP (tetrabutyl ammonium perchlorate) as the supporting electrolyte, the electrochemical process of the ligand acid 4-PBA and its corresponding complexes (4-PB1, 4-PBB, 4-PBP, and 4-PBD) in DMSO solutions was investigated. Measurement was taken on a Corrtest CS 300 (Potentiostat/Galvanostat) Electrochemical Workstation manufactured in China. The working electrode, counter electrode, and reference electrode in this three-electrode electrochemical workstation are glassy carbon having a surface area of 0.03 cm^2, platinum wire, and saturated silver/silver chloride (Ag/AgCl), respectively. The GC electrode was polished and cleaned by an aqueous slurry of alumina (Al_2O_3) using a nylon buffing pad. The experiments were conducted at room temperature in the presence of Ar gas, both with and without varying amounts of SS-DNA [21].

2.4. DNA Binding Behavior through Viscometry

Viscometry was also used to investigate the compound-DNA interaction by using an Oswald viscometer. The time required for the flow of the DNA solution was measured using a digital stopwatch both as the compounds were added gradually and on their own. The average flow time was determined after the experiment was run three times. η° was calculated by using the flow times of the pure solvent and the DNA solution. The η was computed as the difference among the flow times of pure standard DNA solution (t) and DNA solution with different complex concentrations (t°). The viscosities of the DNA solution alone and having varying concentrations of ligand and derived complexes were then plotted on the graph between $(\eta/\eta°)^{1/3}$ and [Compound]/[DNA] [22].

2.5. Antileishmanial Activity

Anti-leishmanial screening against two strains of *Leishmania,* i.e., *L. tropica* (promastigotes), of all synthesized co-crystals 2-7. RPMI 1640 media (Sigma, ST. Louis, USA) containing 10% fetal bovine serum (PAA Lab GmbH, Australia) was used to cultivate leishmanial parasites. The analysis was conducted using Leishmania culture at a density of 1×10^6 cells/mL. The experiment was carried out in a Costar 96-well plate with concentrations ranging from 1 mg/mL to six serial dilutions. Leishmanial cells at a concentration of 1×10^6 were utilized as the control and RPMI medium as the blank. A Cooled incubator was used to incubate the seeded 96-well plate with test dilutions for 72 hours. Using an inverted microscope, the culture was examined for cell viability. The MTT assay was performed the OD was measured at 540 nm. The program EZ-Fit 5.03 Perrella Scientific was used to get the IC_{50} values [23]; furthermore, similar values of IC_{50} were observed in a previous study by Ebrahimisadr *et al*. [24].

3. RESULTS AND DISCUSSION

The four targeted complexes were synthesized in good acceptable yield and pure condition, which is clear from their short-range melting points. They exhibit solubility in DMSO, chloroform, ethanol, and acetone, etc. The physical data is presented in Table S1, whereas the relevant spectroscopic characterization and the activities, which include DNA binding studies and antileishmanial ability, are discussed in the following sections.

3.1. FT-IR Spectroscopic Studies

The solid-state FT-IR data recorded in 400 to 4000 cm^{-1} are presented in Table S2, whereas the selected data are also present in the experimental section**.** The acid deprotonation is verified by the lack of a prominent band at 3500-3000 cm^{-1} as a result of the hydroxyl (-OH) group of the acid. The complexation is apparent by the formation of new bands between 400 to 550 cm^{-1} due to Cd-O/N bonds. The bands associated with C=O at

1685 cm^{-1} were replaced with two new vibrational bands. One indicated COO^- asymmetric (1554–1546 cm^{-1}) and the other COO^- symmetric (1410–1398 cm^{-1}) vibrations provided a clue for the complex formation. [25, 26]. Their difference., $\Delta\upsilon = COO_{asymm}$- COO_{symm} is of significant importance to get a clue about the possible coordination mode adopted by the carboxylate moiety [27, 28]. Deacon and Phillips, studied a large number of FT-IR data of acetates and concluded that $\Delta\upsilon < 200$ cm^{-1} indicated the presence of bidentate coordination, while a monodentate mode is indicated by $\Delta v > 200$ cm^{-1}. Another difference between bidentate (i.e., chelating) and bridging is that the former has a smaller $\Delta\upsilon$ [29]. According to this description, a chelating bidentate mode of coordination, with $\Delta\upsilon$ values of 178 cm^{-1}, 156, 145, and 134, is expected for complexes 4-PB1, 4-PBB, 4-PBP, and 4-PBD, respectively. Two new significant bands in the fingerprint region appear in the 400–600 cm^{-1} range, confirming the coordination of the N-donor moiety and acid ligand to the metal center [30]. Strong vibrational bands in the region 700–900 cm^{-1}, which correspond to C–H out-of-plane vibrations from the aromatic nitrogen heterocyclic ligands, were seen in all of the heteroleptic Cd complexes. These observed vibrational bands are similar to those reported previously [31]. The C-H (out of plane) vibrational bands for the heterocyclic aromatic rings at 774 cm^{-1} (BIPY in 4-PBB), 726 cm^{-1} (PHEN in 4-PBP), and 734 cm^{-1} (Me_2PHEN in 4-PBD) verified the binding of BIPY, PHEN, and Me_2PHEN in complexes. These are in accordance with the observed FT-IR data of the reported similar complexes [32, 33].

3.2. Multi-Nuclear NMR (^{1}H, ^{13}C) Spectroscopy

3.2.1. ^{1}H NMR spectral description

The loss of the hydroxyl proton signal in the synthesized carboxylates' NMR spectrum is a clear indication that the ligand acids were deprotonated. The other protons of the ligand moieties are only slightly shifted in their corresponding spectrum areas, suggesting that they are not directly involved in coordination with the metals [8, 34]. The existence of the N-donor heterocycle in the structure of the synthesized complexes is indicated by signals in the less shielded part of the spectra that indicates the downfield region of the spectra. Complex (4-PBB), containing 2,2'-bipyridine as a nitrogen-donor heterocycle, exhibits spectra with four extra signals arising from the four protons of the heterocycle in a distinctive multiplicity pattern. These protons' chemical shift values were given in the following sequence: Ha > Hd > Hg > Hb, which is in accordance with their free precursor and published data for analogous complexes Complexation of the 1,10-phenanthroline is indicated by the four extra signals seen in the spectra of 4-PBP, which were given chemical shift values in the following order: Ha > Hg > He > Hb. These values fall within the range reported for Phen-based complexes [35]. The presence of 2,9-dimethyl-1,10-phenanthroline is verified by the three new signals present in the deshielded part of 4-PBD spectra, which are resonating signals as well as the singlet at 3.19 ppm ascribed to the methyl group proton. They were given chemical shift values that correspond to the free Me_2Phen ligand in the following order: Hg > He > Hb. The magnetic anisotropic effect, along with the electric dipoles connected to the N-atom, causes these peaks to move to the lower field [36]. The ^{1}H NMR spectra of all complexes are presented in the supplementary file in Figures S1 to S4.

3.2.2. ^{13}C NMR spectral description

^{13}C NMR spectroscopy, which detected the resonance signals from each carbon of the ligand moiety and the nitrogen donor heterocycles, provided additional support for the findings of the ^{1}H NMR spectral analysis. The spectra of the related complexes show a considerable downfield shift at 178.3 ppm for the resonance signal attributed to the C=O group of the ligand 4-PBA. This downfield shift is explained by the deprotonated carboxylate group working in combination with the positively charged metal center to remove this group's electron density. Five extra signals arise in the spectra of complexes 4-PBB, showing attachment of the bipyridine. Its carbon exhibits resonance, and the order of its chemical shift values is Ce > Ca > Cd > Cg > Cb [3]. The emergence of six new signals indicates the coordination of 1,10-phenanthroline and 2,9-dimethyl-1,10-phenanthroline in the spectra of complexes 4-PBP and 4-PBD. These signals have been assigned chemical shift values in the following order: According to the free precursors and their related reported complexes, Ca > Cz > Cg > Cd > Ce > Cb [19]. The ^{13}C NMR spectra of all complexes are presented in the supplementary file in Figure S1 to S4.

3.3. DNA Binding Behavior using UV-Visible Spectroscopy

Using UV-Visible spectroscopy, the ability of the ligand 4-phenylbutyric acid (4-PBA) and its complexes to interact with DNA was examined. The absorption spectra of all the complexes with and without DNA addition are presented in Figure 1. Absorption values within 230 and 320 nm were ascribed to intra-ligand π–π* transitions in the absence of DNA [38]. The method of interaction is typically shown by the spectra obtained by following a consecutive addition of DNA. Ligand (4-PBA) exhibits a hypochromic effect without any accompanying shift in absorption maxima. Some authors in previous studies describe that such changes are associated with groove binding and others with the intercalation. This data has been presented previously, and an intercalative binding interaction is described for the said ligand in the cited data [8].

The absorption spectra of the complexes presented in Figure 1 clearly reveal that the incremental addition of DNA causes a decrease in the absorption intensity, i.e., a hypochromic effect. This hypochromism is the result of a decrease in the electronic transition. The orbital of the DNA and the respective interacting moieties overlap during interaction. The empty or partially filled orbital gets filled, leading to a hypochromic effect. This is accompanied by a red shift for the complex 4-PB1, indicating that the said complex interacts with DNA through intercalation [39]. The spectra of other complexes, as presented in Figure 1, reveal a red to no shift in their absorption maxima.

Loganathan *et al*. [40] favored groove binding above intercalation for such kinds of changes, while Mishra *et al*. [41] observed that the presence of hypochromic effect instead of any corresponding wavelength shift is considered the outcome of intercalation. This leads to the conclusion that they interact with DNA through a dual way of binding, i.e., groove and intercalation [42].

The binding constant (Kb) values were measured using the Benesi-Hildebrand equation,

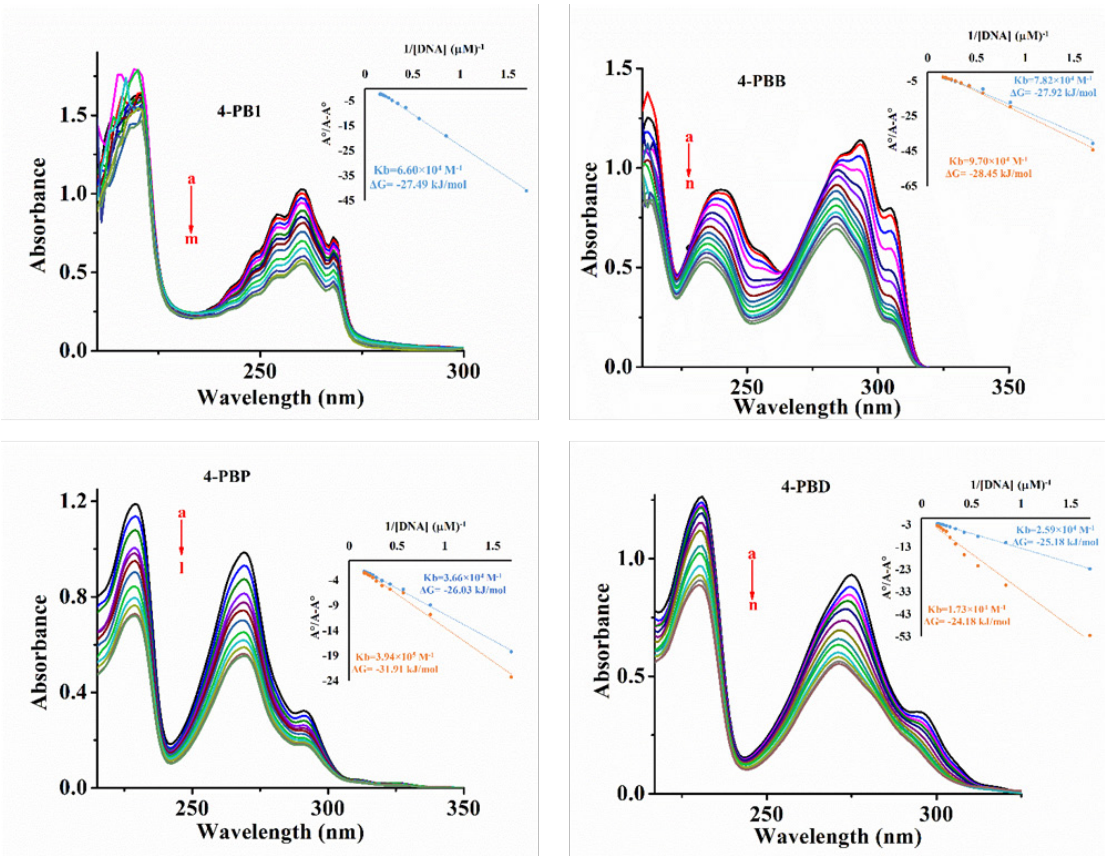

Fig. 1. Absorption spectra of the complexes recorded in the absence and in the presence of increasing DNA concentrations (0.74–7.11 μM for 4-PB1, 0.74–7.67 μM for 4-PBB, 0.74–5.77 μM for 4-PBP, and 0.74–7.67 μM for 4-PBD). In each spectrum, line (a) indicates the free complex, while the remaining lettered spectra represent progressively increasing DNA concentrations.

which is given in the cited data along with its figurative explanation. Using this, the plot was plotted between $A^{\circ}/A\text{-}A^{\circ}$ as ordinate and 1/[DNA] as abscissa. The ratio of intercept to slope (c/m) was calculated, which gives the value of Kb, i.e., the efficiency of binding (see Table 1) [43]. The complexes have higher Kb values than the ligands, attributed to the chelating action. This enhances the complexes' planner activity and functioning and enables effective stacking between DNA base pairs, resulting in increased binding [44]. The complex 4-PBP with phenanthroline attached as the heterocycle moiety exhibited the strongest binding. This is probably because of the expanded planar area of the strong intercalating 1,10-phenanthroline, chelation, and π-π* interaction. This kind of behaviour has been observed for the reported phenanthroline based complexes [45]. The Gibbs free energy was calculated to get an understanding of the process's viability, i.e., whether it was feasible or not:

$$\Delta G = -RT \ln Kb$$

As previously reported for comparable complexes, the data for this parameter show that the ligand acids and their complexes undergo a spontaneous binding process [39].

3.4. DNA Binding Behavior using Cyclic Voltammetry (CV)

The cyclic voltammetry-based DNA-interaction studies reinforced the results of the UV-visible absorption spectroscopy. The electrochemical data (CV) were recorded during a gradual increment in DNA concentration. The changes in the cyclic voltammograms were observed to decide about the manner in which DNA binding proceeds. Compounds with more than one redox center often show peaks or formal potentials that are both positive and negative at the same time, and increases or decreases in current intensity. Findings from the literature indicate that a positive shift is indicative of an intercalative mode of binding, whereas a positive shift mixed with a negative shift shows dual interaction [41]. The complexes' voltammograms are presented in Figure 2. The voltammogram of ligand 4-PBA is reported in the cited data [8]. The complex 4-PB1 experienced a positive shift in the relevant oxidation and reduction peaks, indicating its interaction with DNA through intercalation (see Figure 2). The oxidation and reduction potential peaks of aromatic heterocycles and redox couples linked to the structural motifs of synthesized complexes 4-PBB, 4-PBP, and 4-PBD exhibit a heterogeneous pattern of change (see Table S2). For complexes involving many oxidation-reduction potentials, the combination of these changes in the complexes' voltammograms is very typical [46]. It's crucial to remember that the complex 4-PBB's cyclic voltammogram showed one separate oxidation and reduction, which was linked to the emergence of new potential electroactive species. Because the concentration of the electroactive species decreases and the attached species diffuses slowly towards the electrode surface, the complex binding to the DNA causes a drop in current [47]. On the other hand, the species that become adsorbed on the electrode's surface could be the cause of the perceived rise in current intensity, offsetting the actual decrease in current [48].

3.5. DNA binding behaviour using Viscometry

DNA binding can also be studied through viscometry

Table 1. Binding constant (Kb) and Gibbs' free energy (ΔG) against the respective λmax.

Codes	Compound	λ_{max} (nm)		Kb (M^{-1})	ΔG (KJ/mol)
		Before DNA	After DNA		
4-PB1	$[Cd(4\text{-}PBA)_2]$	260	260	6.60×10^4	-27.49
4-PBB	$[Cd(4\text{-}PBA)_2BIPY]$	286	283	9.70×10^4	-28.45
		240	234	7.82×10^4	-27.92
4-PBP	$[Cd(4\text{-}PBA)_2PHEN]$	269	-	3.66×10^5	-31.73
		229	-	3.94×10^5	-31.91
4-PBD	$[Cd(4\text{-}PBA)_2(Me_2PHEN)]$	274	271	2.59×10^5	-30.88
		230	229	1.73×10^5	-29.88

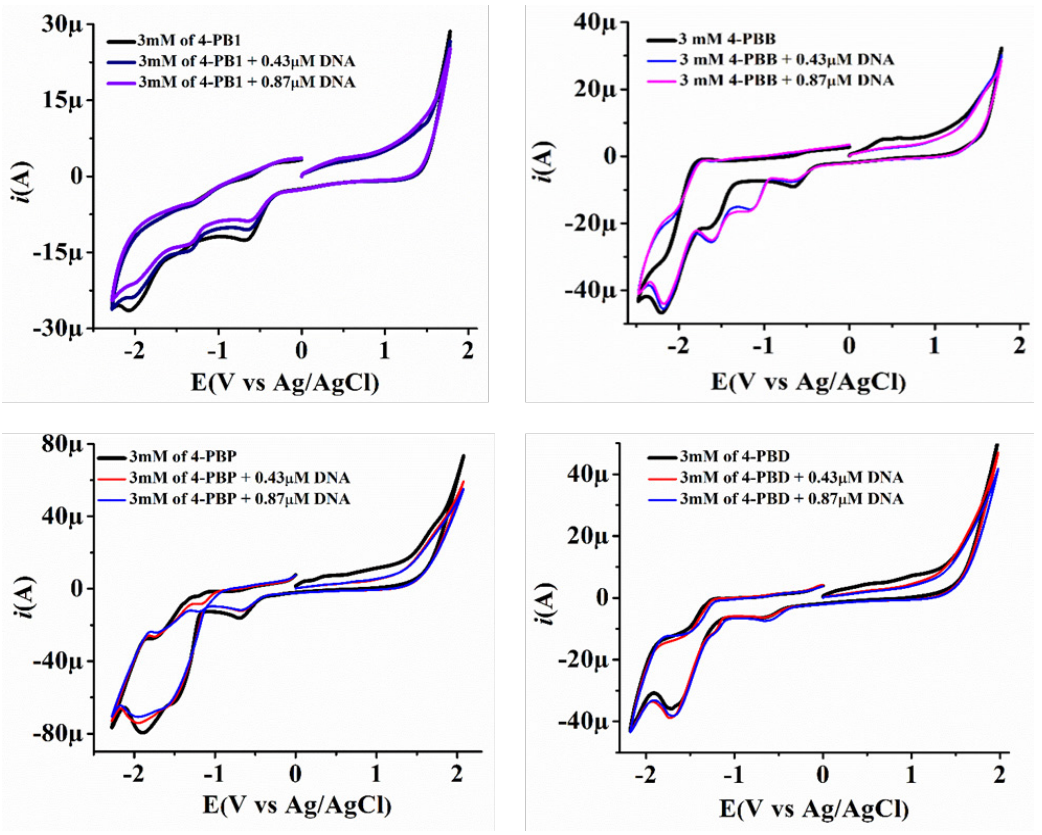

Fig. 2. Cyclic voltammograms of the complexes in the absence and during increasing concentration of DNA.

and the test which is significant to indicate this binding is the hydrodynamic measurements because they are sensitive to variations in length. A literature review shows that an increase in viscosity values is the outcome of DNA interaction via the intercalation mode. This is due to the DNA base pairs' lengthening to make room for the binding moieties. Conversely, non-intercalative interactions occur in the DNA helical structure folding or bending, which causes the viscosity to drop little or not at all [49]. Figure 3 makes it clear how the ligand acid 4-PBA interaction behaviour and its complexes affect the viscosity of DNA. In the case of ligand acid 4-PBA and complex 4-PB1, a consistent rise in viscosity was noted, which is suggestive of the intercalation method. On the other hand, all other complexes exhibit a moderate to gradual increase/ irregularity that enables the coexistence of surface binding modes and intercalation.

3.6. Antileishmanial Activity

The antileishmanial effectiveness of the ligand 4-PBA and its homo- and heteroleptic cadmium (II) carboxylates against *Leishmania tropica* promastigotes was evaluated using the ATCC strain. Promastigote vitality was evaluated in both treated and control samples after a 24-hour incubation period. Surprisingly, treated samples showed a significant decrease in viability when compared to control samples, as shown in Table 2. The ligand 4-PBA appeared to be inactive against tested standards with IC_{50} values of 3.39 ± 0.01,

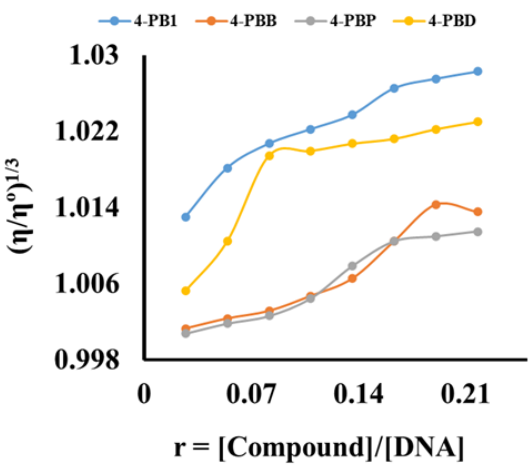

Fig. 3. Graph indicating the effect of a change in the viscosity of DNA.

Table 2. Antileishmanial activity (IC_{50} ± S.D.) of ligand and synthesized Cd(II) carboxylates.

Code	Sample	IC_{50} (μM) ± S.D.
4-PBA	4-Phenylbutyric acid	60.35 ± 0.02
4-PB1	$[Cd(L1)_2]$	40.35 ± 0.02
4-PBB	$[Cd(L1)_2bipy]$	24.54 ± 0.02
4-PBP	$[Cd(L1)_2Phen]$	15.63 ± 0.05
4-PBD	$[Cd(L1)_2(Me_2Phen]$	18.16 ± 0.02
Standard Drugs	Amphotericin	3.39 ± 0.01
	Miltefosine	31.8 ± 0.02
	Pentamidine	9.23 ± 0.01

31.8 ± 0.02, and 9.23 ± 0.01 μM for amphotericin, miltefosine, and pentamidine, respectively [50]. However, all synthesized cadmium metal complexes showed good to moderate anti-leishmanial potential against *L. tropica*. Among them, $[Cd(L1)_2Phen]$ (4-PBP, IC_{50} = 15.63 ± 0.05 μM) appeared to be the most potent antileishmanial agent, followed by $[Cd(L1)_2(Me_2Phen]$ (4-PBD, IC_{50} = 18.16 ± 0.02 μM) and $[Cd(L1)_2]$ (4-PBB, IC_{50} = 24.54 ± 0.02 μM). The two 4-Phenylbutyric acid-containing $[Cd(L1)_2]$ (4-PB1 = 40.35 ± 0.02 μM) appeared to be the least active member of the metal complexes. The increased planar surface afforded by the connected heterocyclic moieties for stacking contact with the pathogen's DNA, which results in DNA damage, may be the cause of these compounds' powerful nature, in addition to a variety of structural variables important for anti-pathogen activity. The suppression of the pathogen's active enzymes is another potential cause of activity. The active complexes may interact with the enzyme in different ways, changing its mechanism and ultimately deactivating it [51, 52]. The most effective synthesized complex, 4-PBD, killed the promastigotes even at low concentrations.

4. CONCLUSIONS

Here, Cd(II) complexes were synthesized using bioactive moieties such as nitrogen heterocycles and 4-phenylbutyric acid. The synthesis was carried out with consideration for their potential application as drugs that can target DNA. The 4-phenylbutyric acid in combination with the structural and electronic properties of 2,2′-bipyridine, 1,10-phenanthroline, and 2,9-dimethyl-1,10-phenanthroline successfully adjusted the geometric environment surrounding the Cd(II) core. The bidentate coordination of 4-phenylbutyric acid is evident by the FT-IR data. The proton and carbon of the compound under investigation are clearly responsible for the resonance signal seen in the ^{1}H and ^{13}C spectra. The compounds were found to interact with DNA by intercalation, groove binding, and mixed modes of interaction following a spontaneous process, as indicated by the -ve values of ΔG. The antileishmanial activity against *L. tropica* promastigote was assessed *in vitro* for the ligand and its derived complexes. The results imply that they could be explored further to be used as an effective drug candidate against leishmaniasis. According to the results, this type of structural design compound could be very helpful in the search and finding for new, effective treatments for DNA-related disorders.

5. ACKNOWLEDGEMENT

S.A. is grateful to the Pakistan Academy of Sciences and Quaid-i-Azam University, Islamabad for the financial assistance.

6. ETHICAL STATEMENT

In this work no human or animal subjects are involved; therefore, ethical approval was not required.

7. DECLARATION OF COMPETING INTEREST

The authors have no conflict of interest.

8. AUTHORSHIP CONTRIBUTION STATEMENT

Aneea Sharif**:** Investigation, writing original draft, review & editing. Saba Naz: Data interpretation, reviewing, editing, and overall refinement of the

manuscript**.** Saqib Ali: Conceptualization, Supervision, Project administration, Funding acquisition. Ali Haider: Methodology, Validation, Resources, review & editing. Sammar Yousuf: Antileishmanial study and its data interpretation. Mehboob ur Rehman: Software handling, formal analysis, and data curation.

9. REFERENCES

1. M. El-SayedAzab. Leishmaniasis. In: *Textbook of Parasitic Zoonoses*. S.C. Parija, and A. Chaudhury (Eds.). *Springer Nature Singapore, Singapore* pp. 107-124 (2022). https://doi.org/10.1007/978-981-16-7204-0_11
2. D. Dourado, T.S. Medeiros, É. do Nascimento Alencar, E.M. Sales, and F.R. Formiga. Curcumin-loaded nanostructured systems for treatment of leishmaniasis: a review. *Beilstein Journal of Nanotechnology* 15(1): 37-50 (2024). https://doi.org/10.3762/bjnano.15.4
3. M. Tufail and C. Wu. Retraction Note: Exploring the Burden of Cancer in Pakistan: an analysis of 2019 Data. *Journal of Epidemiology and Global Health* 15(1): 127 (2025). https://doi.org/10.1007/s44197-023-00104-5
4. K.J. Franz and N. Metzler-Nolte. Introduction: metals in medicine. *Chemical Reviews* 119(2): 727-729 (2019). https://doi.org/10.1021/acs.chemrev.8b00685
5. Z. Yin, Y. Wang, L.R. Whittell, S. Jergic, M. Liu, E. Harry, N.E. Dixon, M.J. Kelso, J.L. Beck, and A.J. Oakley. DNA replication is the target for the antibacterial effects of nonsteroidal anti-inflammatory drugs. *Chemistry & Biology* 21(4): 481-487 (2014). https://doi.org/10.1016/j.chembiol.2014.02.009
6. S. Bindu, S. Mazumder, and U. Bandyopadhyay. Non-steroidal anti-inflammatory drugs (NSAIDs) and organ damage: A current perspective. *Biochemical Pharmacology* 180: 114147 (2020). https://doi.org/10.1016/j.bcp.2020.114147
7. A.C. Santos, L.P. Monteiro, A.C. Gomes, F. Martel, T.M. Santos, and B.J.L. Ferreira. NSAID-based coordination compounds for biomedical applications: recent advances and developments. *International Journal of Molecular Sciences* 23(5): 2855 (2022). https://doi.org/10.3390/ijms23052855
8. S. Naz, N. Uddin, S. Rahim, N. Muhammad, M. Bibi, S. Yousuf, K.S. Munawar, K. Shahid, A. Haider, and S. Ali. 4-Phenylbutyric acid based homo-heteroleptic Zn (II) carboxylates: Synthesis, structural elucidation, DNA interaction through spectroscopic and computational methods as well as ALP inhibition study. *Journal of Molecular Liquids* 356: 119031 (2022). https://doi.org/10.1016/j.molliq.2022.119017
9. Z.M. Ziaie and M. Mokhtary. A Theoretical Investigation of Heterocycles with N–O Bonds Understanding the Biological Effects and Theoretical Studies: From Theory to Applicatio. *Journal of Chemical Reviews* 7(2): 166-190 (2025). https://doi.org/10.48309/jcr.2025.503047.1411
10. G. Raymoni and H.A. Ali. Synthesis, structures and various biological applications of new Zn (II) complexes having different coordination modes controlled by the drug furosemide in presence of bioactive nitrogen based ligands. *Applied Organometallic Chemistry* 33(1): e4680 (2019). https://doi.org/10.1002/aoc.4680
11. M.S. Islas, J.J.M. Medina, O.E. Piro, G.A. Echeverría, E.G. Ferrer, and P.A. Williams. Comparisons of the spectroscopic and microbiological activities among coumarin-3-carboxylate, o-phenanthroline and zinc (II) complexes. *Spectrochimica Acta Part A: Molecular and Biomolecular Spectroscopy* 198: 212-221 (2018). https://doi.org/10.1016/j.saa.2018.03.003
12. M. Borsari. Cadmium: Coordination Chemistry. In: Encyclopedia of Inorganic and Bioinorganic Chemistry. R.A. Scott (Ed.). *John Wiley & Sons* pp. 1-16 (2014). https://doi.org/10.1002/9781119951438.eibc2261
13. G. Gobe and D. Crane. Mitochondria, reactive oxygen species and cadmium toxicity in the kidney. T*oxicology Letters* 198(1): 49-55 (2010). https://doi.org/10.1016/j.toxlet.2010.04.013
14. B.A. Rzigalinski and J.S. Strobl. Cadmium-containing nanoparticles: perspectives on pharmacology and toxicology of quantum dots. *Toxicology and Applied Pharmacology* 238(3): 280-288 (2009). https://doi.org/10.1016/j.taap.2009.04.010
15. H. Bibi, A. Shamim, S. Naz, M.H. Bhatti, M. ur Rehman, A. Haider, and S. Ali. Cd (II) Derivatives of Substituted Phenylacetic Acids, Synthesis, Spectroscopic Characterization and Binding Studies with DNA. *Proceedings of the Pakistan Academy of Sciences: A. Physical and Computational Sciences* 62(4): 337-347 (2025). https://doi.org/10.53560/PPASA(62-4)704
16. G. V. Scaeteanu, C. Maxim, M. Badea and R. Olar. An overview of various applications of cadmium carboxylate coordination polymers, *Molecules* 29(16): 3874 (2024) 3874. https://doi.org/10.3390/molecules29163874

17. N. Gogoleva, M. Shmelev, M. Kiskin, A. Starikov, A. Sidorov, I. Eremenko, Isomerization of Binuclear Cadmium Carboxylate Complexes $[Cd_2L_2(O_2CR)_4]$. *Russian Journal of Coordination Chemistry* 47(4): 261-271 (2021). https://doi.org/10.1134/S1070328421040035
18. Y. Lin, X. Zhang, W. Chen, W. Shi, P. Cheng, Three cadmium coordination polymers with carboxylate and pyridine mixed ligands: luminescent sensors for FeIII and CrVI ions in an aqueous medium. *Inorganic Chemistry* 56(19): 11768-11778 (2017) . https://doi.org/10.1021/acs.inorgchem.7b01790
19. L. Qadeer, S. Ali, A. Haider, N. Uddin, K.S. Munawar, M. Ashfaq, M.N. Tahir, and M.U. Rehman. Synthesis, spectral elucidation and DNA binding studies of cadmium(II) carboxylates with nitrogen donor heteroligands. *Inorganic Chemistry Communications* 168: 112894 (2024). https://doi.org/10.1016/j.inoche.2024.112894
20. S. Naz, M. Sirajuddin, I. Hussain, A. Haider, A. Nadhman, A. Gul, S. Faisal, S. Ullah, S. Yousuf, and S. Ali. 2-Phenylbutyric acid based organotin (IV) carboxylates: synthesis, spectroscopic characterization, antibacterial action against plant pathogens and in vitro hemolysis. *Journal of Molecular Structure* 1203: 127378 (2020). https://doi.org/10.1016/j.molstruc.2019.127378
21. S. Naz, S. Ullah, U. Iqbal, S. Yousuf, S. Rahim, N. Muhammad, R. Fatima, I.U. Haq, A. Haider, and S. Ali. Homo-and heteroleptic 3-methylbenzoates of zinc (II) ion based on N-donor heterocycles: structure, DNA binding and pharmacological evaluation. *Journal of Molecular Liquids* 368: 120792 (2022). https://doi.org/10.1016/j.molliq.2022.120792
22. M. Zubair, M. Sirajuddin, K. Ullah, A. Haider, F. Perveen, I. Hussain, S. Ali, and M.N. Tahir. Synthesis, structural peculiarities, theoretical study and biological evaluation of newly designed O-Vanillin based azomethines. *Journal of Molecular Structure* 1205: 127574 (2020). https://doi.org/10.1016/j.molstruc.2019.127574
23. M.I. Choudhary, S. Yousuf, S.A.A. Shah, and S. Ahmed. Biotransformation of physalin H and leishmanicidal activity of its transformed products. *Chemical and Pharmaceutical Bulletin* 54(7): 927-930 (2006). https://doi.org/10.1248/cpb.54.927
24. P. Ebrahimisadr, F. Ghaffarifar, and Z.M. Hassan. In-vitro evaluation of antileishmanial activity and toxicity of artemether with focus on its apoptotic effect. *Iranian Journal of Pharmaceutical Research* 12(4): 903 (2013). https://doi.org/10.22037/ijpr.2013.1406
25. A. Sarfraz, S. Naz, A. Haider, K.S. Munawar, R. Fatima, S. Yousuf, M.N. Tahir, Y. Wasti, I.U. Haq, and S. Ali. Synthesis, Characterization, and in vitro pharmacological evaluation of Zinc (II) complexes of cycloalkanes and bioactive nitrogen donor heterocycles. *Journal of Molecular Liquids* 418: 126713 (2025). https://doi.org/10.1016/j.molliq.2024.126713
26. K.I. Hadjiivanov, D.A. Panayotov, M.Y. Mihaylov, E.Z. Ivanova, K.K. Chakarova, S.M. Andonova, and N.L. Drenchev. Power of infrared and Raman spectroscopies to characterize metal-organic frameworks and investigate their interaction with guest molecules. *Chemical Reviews* 121(3): 1286-1424 (2020). https://doi.org/10.1021/acs.chemrev.0c00487
27. P.N. Nelson and R.A. Taylor. Theories and experimental investigations of the structural and thermotropic mesomorphic phase behaviors of metal carboxylates. *Applied Petrochemical Research* 4(3): 253-285 (2014). https://doi.org/10.1007/s13203-014-0044-3
28. J. Kalembkiewicz, M. Kosińska, and L. Zapała. Complexes of aminobenzoic acids: a comprehensive review concerning synthesis, physical chemistry, structure and application. *Coordination Chemistry Reviews* 348: 25-53 (2017). https://doi.org/10.1016/j.ccr.2017.07.004
29. G. Deacon and R. Phillips. Relationships between the carbon-oxygen stretching frequencies of carboxylato complexes and the type of carboxylate coordination. *Coordination Chemistry Reviews* 33(3): 227-250 (1980). https://doi.org/10.1016/S0010-8545(00)80455-5
30. V.P. Singh, S. Singh, D.P. Singh, K. Tiwari, and M. Mishra. Synthesis, spectroscopic (electronic, IR, NMR and ESR) and theoretical studies of transition metal complexes with some unsymmetrical Schiff bases. *Journal of Molecular Structure* 1058: 71-78 (2014). https://doi.org/10.1016/j.molstruc.2013.10.046
31. K. Ullah, S. Ali, A. Haider, S. Naz, S. Yousuf, K.S. Munawar, M.S. Jan, R. Zafar, and R. Kumar. Investigation of pivalic acid-derived organotin (IV) carboxylates: Synthesis, structural insights, interaction with biomolecules, and computational studies. *Journal of Molecular Structure* 1322: 140444 (2025). https://doi.org/10.1016/j.molstruc.2024.140444
32. N. Muhammad, M. Ikram, S. Rehman, M. Ibrahim, Viola, and C. Schulzke. Structural, thermal kinetics and thermodynamics study of new mixed ligand

zinc complexes. *Journal of Thermal Analysis and Calorimetry* 128(1): 627-637 (2017). https://doi.org/10.1007/s10973-016-5842-7

33. L.Q. Chai, Q. Hu, K.Y. Zhang, L. Zhou, and J.J. Huang. Synthesis, structural characterization, spectroscopic, and DFT studies of two penta-coordinated zinc (II) complexes containing quinazoline and 1, 10-phenanthroline as mixed ligands. *Journal of Luminescence* 203: 234-246 (2018). https://doi.org/10.1016/j.jlumin.2018.06.058
34. M. Tahir, M. Sirajuddin, M. Zubair, A. Haider, A. Nadman, S. Ali, F. Perveen, H.B. Tanveer, and M.N. Tahir. Designing, spectroscopic and structural characterization and evaluation of biological potential as well as molecular docking studies of Zn (II)-based metallo-pharmaceuticals. *Journal of the Iranian Chemical Society* 18(7): 1689-1702 (2021). https://doi.org/10.1007/s13738-020-02142-3
35. S. Aslam, A.A. Isab, M.A. Alotaibi, M. Saleem, M. Monim-ul-Mehboob, S. Ahmad, I. Georgieva, and N. Trendafilova. Synthesis, spectroscopic characterization, DFT calculations and antimicrobial properties of silver (I) complexes of 2, 2′-bipyridine and 1, 10-phenanthroline. *Polyhedron* 115: 212-218 (2016). https://doi.org/10.1016/j.poly.2016.04.047
36. A.S. Gaballa, C. Wagner, S.M. Teleb, E.-M. Nour, M. Elmosallamy, G.N. Kaluđerović, H. Schmidt, and D. Steinborn. Preparation, spectroscopic and structural studies on charge-transfer complexes of 2, 9-dimethyl-1, 10-phenanthroline with some electron acceptors. *Journal of Molecular Structure* 876(1-3): 301-307 (2008). https://doi.org/10.1016/j.molstruc.2007.07.003
37. R. Castro, J.A. Garcia-Vazquez, J. Romero, A. Sousa, C.A. McAuliffe, and R. Pritchard. Electrochemical synthesis of benzothiazole-2-thionato complexes of nickel (II), Zinc (II) and cadmium(II): the crystal structure of 2, 2′-bipyridine bis (benzothiazole-2-thionato) zinc (II). *Polyhedron* 12(18): 2241-2247 (1993). https://doi.org/10.1016/S0277-5387(00)88263-7
38. R. Kumar, P. Bhargava, and A. Dvivedi. Synthesis and characterization of a new cadmium complex, cadmium [(1, 10-phenanthroline) (8-hydroxyquinoline)] Cd (Phen). *Procedia Materials Science* 10: 37-43 (2015). https://doi.org/10.1016/j.mspro.2015.06.023
39. S. Ullah, M. Sirajuddin, Z. Ullah, A. Mushtaq, S. Naz, M. Zubair, A. Haider, S. Ali, M. Kubicki, and T.A. Wani. Synthesis, structural elucidation and pharmacological applications of Cu (II) heteroleptic carboxylates. *Pharmaceuticals* 16(5): 693 (2023). https://doi.org/10.3390/ph16050693
40. R. Loganathan, S. Ramakrishnan, M. Ganeshpandian, N.S. Bhuvanesh, M. Palaniandavar, A. Riyasdeen, and M.A. Akbarsha. Mixed ligand copper (II) dicarboxylate complexes: the role of co-ligand hydrophobicity in DNA binding, double-strand DNA cleavage, protein binding and cytotoxicity. *Dalton Transactions* 44(22): 10210-10227 (2015). https://doi.org/10.1039/C4DT03879G
41. M. Mishra, K. Tiwari, S. Shukla, R. Mishra, and V.P. Singh. Synthesis, structural investigation, DNA and protein binding study of some 3d-metal complexes with N′-(phenyl-pyridin-2-yl-methylene)-thiophene-2-carboxylic acid hydrazide. *Spectrochimica Acta Part A: Molecular and Biomolecular Spectroscopy* 132: 452-464 (2014). https://doi.org/10.1016/j.saa.2014.05.007
42. T. Yasmeen, S. Naz, F. Younas, S. Ali, Z. Rashid, A. Haider, M. Sirajuddin, B.S. Bassil, U. Kortz, and T.A. Wani. Heteroleptic tri-and di-organotin (IV) carboxylates: Synthesis, characterization and anticancer evaluation. *Journal of Molecular Structure* 1323: 140742 (2025). https://doi.org/10.1016/j.saa.2014.05.007
43. R. Hajian, P. Hossaini, Z. Mehrayin, P.M. Woi, and N. Shams. DNA-binding studies of valrubicin as a chemotherapy drug using spectroscopy and electrochemical techniques. *Journal of Pharmaceutical Analysis* 7(3): 176-180 (2017). https://doi.org/10.1016/j.jpha.2017.01.003
44. Y. Li, Z.-Y. Yang, and M.-F. Wang. Synthesis, characterization, DNA binding properties, fluorescence studies and antioxidant activity of transition metal complexes with hesperetin-2-hydroxy benzoyl hydrazone. *Journal of Fluorescence* 20(4): 891-905 (2010). https://doi.org/10.1007/s10895-010-0635-z
45. A. Tarushi, G. Psomas, C.P. Raptopoulou, and D.P. Kessissoglou. Zinc complexes of the antibacterial drug oxolinic acid: structure and DNA-binding properties. *Journal of Inorganic Biochemistry* 103(6): 898-905 (2009). https://doi.org/10.1016/j.jinorgbio.2009.03.007
46. G. Psomas. Mononuclear metal complexes with ciprofloxacin: Synthesis, characterization and DNA-binding properties. *Journal of Inorganic Biochemistry* 102(9): 1798-1811 (2008). https://doi.org/10.1016/j.jinorgbio.2008.05.012
47. S.U. Rehman, T. Sarwar, M.A. Husain, H.M. Ishqi, and M. Tabish. Studying non-covalent drug–DNA interactions. *Archives of Biochemistry and Biophysics* 576: 49-60 (2015). https://doi.

org/10.1016/j.abb.2015.03.024

48. B. Amritha and S. Vasudevan. Synthesis, characterisation, and DNA interaction studies of novel Cu (II), Ni (II), and Co (II) mono and bisligand complexes of N-(1, 10-phenanthrolin-5-yl) acridine-9-carboxamide. *Chemical Papers* 74(6): 1979-1996 (2020). https://doi.org/10.1007/s11696-019-01041-z
49. Y.J. Liu, X.Y. Guan, X.Y. Wei, L.X. He, W.J. Mei, and J.H. Yao. Ruthenium (II) complexes containing 2, 9-dimethyl-1, 10-phenanthroline and 4, 4′-dimethyl-2, 2′-bipyridine as ancillary ligands: synthesis, characterization and DNA-binding. *Transition Metal Chemistry* 33(3): 289-294 (2008). https://doi.org/10.1007/s11243-007-9042-y
50. S. Naz, N. Uddin, K. Ullah, A. Haider, A. Gul, S. Faisal, A. Nadhman, M. Bibi, S. Yousuf, and S. Ali. Homo-and heteroleptic Zinc (II) carboxylates: Synthesis, structural characterization, and assessment of their biological significance in in vitro models. *Inorganica Chimica Acta* 511: 119849 (2020). https://doi.org/10.1016/j.ica.2020.119849
51. G. Colotti, A. Ilari, A. Fiorillo, P. Baiocco, M.A. Cinellu, L. Maiore, F. Scaletti, C. Gabbiani, and L. Messori. Metal-based compounds as prospective antileishmanial agents: inhibition of trypanothione reductase by selected gold complexes. *ChemMedChem* 8(10): 1634-1637 (2013). https://doi.org/10.1002/cmdc.201300276
52. Y.C. Ong, L. Kedzierski, and P.C. Andrews. Do bismuth complexes hold promise as antileishmanial drugs? *Future Medicinal Chemistry* 10(14): 1721-1733 (2018). https://doi.org/10.4155/fmc-2017-0287

Proceedings of the Pakistan Academy of Sciences: A Physical and Computational Sciences 63(2): S1-S2 (2026)

ISSN (Print): 2518-4245; ISSN (Online): 2518-4253

Pakistan Academy of Sciences

Supplementary Data

Homo- and Heteroleptic Cd(II) 4-Phenylbutyrates, Synthesis, Exploration of Chemistry, DNA Binding Study and Antileishmanial Activity

Aneeqa Sharif[1], Saba Naz[1], Saqib Ali[1*], Ali Haider[1], Sammar Yousuf[2,3], and Mahboob-ur-Rehman[4]

[1]Department of Chemistry, Quaid-i-Azam University, Islamabad, 45320, Pakistan
[2]H.E.J. Research Institute of Chemistry (International Center for Chemical and Biological Sciences) University of Karachi, Karachi-75270, Pakistan
[3]Institute of Molecular Biology and Biotechnology, University of Lahore, Lahore, Pakistan
[4]Department of Cardiology, Pakistan Institute of Medical Sciences (PIMS), Islamabad, Pakistan

Table S1: Physical data of ligand and its synthesized complexes.

Code	Compound	Mol. Formula	Mol. Wt (g/mol)	M.P (°C)	Yield (%)
4-PBA	4-Phenylbutyric acid	$C_{10}H_{12}O_2$	164.08	49-51	-
4-PB1	[Cd(4-PBA)$_2$]	$C_{20}H_{22}CdO_4$	438.80	250-253	67
4-PBB	[Cd(4-PBA)$_2$BPY]	$C_{30}H_{30}CdN_2O_4$	596.12	123-125	73
4-PBP	[Cd(4-PBA)$_2$PHEN]	$C_{32}H_{30}CdN_2O_4$	620.12	179-180	85
4-PBD	[Cd(4-PBA)$_2$(Me$_2$PHEN)]	$C_{34}H_{34}CdN_2O_4$	647.07	156-158	83

Table S2: FT-IR data of ligand and its synthesized complexes.

Code	Compound	-OH	C=O/C-O		Δυ	Cd-O	Cd-N	C-H
4-PBA	4-Phenylbutyric acid	3340-2500	1685/1292		-	-	-	-
			COO^-_{asymm}	COO^-_{symm}				
4-PB1	[Cd(4-PBA)$_2$]	-	1546	1398	148	462	524	-
4-PBB	[Cd(4-PBA)$_2$BPY]	-	1550	1407	143	420	533	763, 722
4-PBP	[Cd(4-PBA)$_2$PHEN]	-	1554	1409	145	427	566	849, 728
4-PBD	[Cd(4-PBA)$_2$(Me$_2$PHEN)]	-	1548	1410	138	418	550	859,731

* Corresponding Author: Saqib Ali <saqibali@qau.edu.pk>

Table S3: CV Data indicating binding parameters with DNA.

Code	Before DNA		After DNA		Change in E		Remarks
	Ea	Ec	Ea´	Ec´	ΔEa	ΔEc	
4-PB1	-0.3803	-0.6696	-0.2219	-0.6041	0.1584	0.0655	Positive shift
	-0.9700	-1.4197	-1.0405	-1.3277	-0.0705	0.092	Positive shift
	-	-2.057	-	-1.9562	-	0.1008	Positive shift
4-PBB	0.4271	-	Disappear	-	Disappear	-	-
	-0.4812	-0.6473	Disappear	-0.5992	-	0.0481	Positive shift
	-	-1.661	-	-1.614	-	0.047	Positive shift
				-1.1548			New peak
	-1.778	-2.204	-1.693	-2.176	0.085	0.028	Positive and Negative shift
			-2.2522				New peak
4-PBP	-1.6036	-	Disappear	-	Disappear	-	-
	0.3985		Disappear				
	-0.5605	-0.6742	-	-0.6600	-	0.0142	Positive shift
	-1.095	-	disappear	-	Disappear	-	-
	-1.286	-1.488	-1.13040	-1.6031	0.1556	-0.1151	Positive and negative shift
	-1.855	-1.8905	-1.7984	-1.9592	0.0566	-0.0687	Positive and negative shift
4-PBD	-	-0.640	-	-0.614	-	0.026	Positive shift
	-1.859	-	-1.768	-	0.091	-	Positive shift
	-1.255	-1.732	-1.244	-1.671	0.011	0.061	Positive and Negative shift

Instructions For Authors

1. Manuscript Writing

The manuscript may contain a Title, Abstract, Keywords, INTRODUCTION, MATERIALS AND METHODS, RESULTS, DISCUSSION (or RESULTS AND DISCUSSION), CONCLUSIONS, ETHICAL STATEMENT (if applicable), ACKNOWLEDGEMENTS, CONFLICT OF INTEREST and REFERENCES, *and any other information that the author(s) may consider necessary*.

Title (Bold and font size 16): The title should be expressive, concise, and informative to the entire readership of the journal. It may include common terms, to make it more identifiable when people search online. Please avoid the use of long pervasive terms and non-standard or obscure abbreviations, acronyms, or symbols.

Abstract (font size 10, max 250 words)**:** Must be self-explanatory**,** stating the rationale, objective(s), methodology, main results, and conclusions of the study. Abbreviations, if used, must be defined on the first mention in the Abstract as well as in the main text. Abstracts of review articles may have a variable format.

Keywords (font size 10)**:** Provide five to eight keywords consisting of words and phrases that are closely associated with the topic depicting the article.

INTRODUCTION (font size 11)**:** Provide a clear and concise statement of the problem, citing relevant recent literature, and objectives of the investigation. Cite references in the text by number in square brackets**,** the reference must be cited in a proper English sentence [1]. or "... as previously described [3, 6-8]". For a single author: Bednorz [2] investigated the environmental pollution ... When there are only two authors: Bednorz and Allan [2] investigated the environmental pollution ... and for three or more authors: Bednorz *et al.* [2] investigated the environmental pollution ..; and list them in the REFERENCES section, in the order of citation in the text.

MATERIALS AND METHODS (font size 11)**:** Provide an adequate account of the procedures or experimental details, including statistical tests (if any), concisely but sufficiently enough to replicate the study. Relevant references to methodology must be cited.

RESULTS (font size 11)**:** Be clear and concise with the help of appropriate Tables, Figures, and other illustrations. Data should not be repeated in Tables and Figures but must be supported with statistics. The data presented in Tables and Figures must be elaborated in the main text.

DISCUSSION (font size 11)**:** Provide interpretation of the RESULTS in the light of previous relevant studies, citing published references.

CONCLUSIONS (font size 11)**:** Briefly state the implication of your study findings, and carefully address the study questions. Confine your conclusions according to the objectives of your study and the aspects covered in the abstract. Discuss both positive and negative findings.

ETHICAL STATEMENT (font size 10)**:** The statement of ethical approval by an appropriate ethics committee or review board must be included in the manuscript (if applicable), as per the Journal's policy.

ACKNOWLEDGEMENTS: (font size 10)**:** In a brief statement, acknowledge the financial support and other assistance, if any.

FUNDING (font size 10): Please state if any funding was received, otherwise state: No funding was received to conduct this research.

CONFLICT OF INTEREST (font size 10)**:** State if there is any conflict of interest.

AUTHORSHIP CONTRIBUTION STATEMENT (font size 10)**:** Give authors contributions statement.

DECLARATION: Provide a declaration that: (i) the results are original, (ii) the same material is neither published nor under consideration for publication elsewhere, (iii) approval of all authors has been obtained, and (iv) in case the article is accepted for publication, its copyright will be assigned to the *Pakistan Academy of Sciences*. Authors must obtain permission to reproduce, where needed, copyrighted material from other sources and ensure that no copyrights are infringed upon.

REFERENCES (font size 10)**:** All cited references must be related to the subject of the article and to the

context in which they are cited. References must be listed in numerical order as listed in the main text. Only published (and accepted for publication) journal articles, books and book chapters, conference proceedings, online reports, a degree thesis, and materials available on the website qualify for REFERENCES. **Cite only relevant references. The author(s) must ensure that the reference statement accurately reflects the cited work's content, context, and findings to maintain academic integrity**. Give online link/doi for published articles.

2. Manuscript Formatting

Manuscripts must be submitted in Microsoft Word (Latest Version .doc or .docx format); pdf files are not acceptable. Figures can be submitted separately in TIFF, GIF, JPEG, EPS, or PPT. Manuscripts, in *Times New Roman*, 1.15 spaced (but use single-space for Tables, long headings, and long captions of tables and figures). The Manuscript sections must be numbered, i.e., **1. INTRODUCTION, 2. MATERIALS AND METHODS,** and so on… (a) **Title** of the article **(**Capitalize the initial letter of each main word, font-size 16, **bold**), max 160 characters (no abbreviations or acronyms), depicting article's contents; (b) Author's complete name (font size 12, **bold**), and professional affiliation (i.e., each author's Department, Institution, Mailing address, and Email and Contact number, but no position titles) (font size 12); (c) Indicate the corresponding author with *; and (d) **Short running title**, max 50 characters (font size 10).
Headings and Subheadings (font size 11): All flush left
LEVEL-1: **ALL CAPITAL LETTERS; Bold**
Level-2: **Capitalize Each First Letter (**Except prepositions**); Bold**
Level-3: Capitalize the first letter only (Sentence case)***; Bold, Italic***
Level-4: *Run-in head*; *Italics*, *in the normal paragraph position. Capitalize the first letter only and end in a colon (i.e., **:**)*

A list of REFERENCES must be prepared as under:
a. Journal Articles *(Name of journals must be stated in full)*

1. J. Rashid, A. Ahsan, M. Xu, I. Savina, and F. Rehman. Synthesis of cerium oxide embedded perovskite type bismuth ferrite nanocomposites for sonophotocatalysis of aqueous micropollutant ibuprofen. *RSC Advances* 13(4): 2574-2586 (2023). https://doi.org/10.1039/d2ra07509a
2. A. Fayyaz, N. Ali, Z.A. Umar, H. Asghar, M. Waqas, R. Ahmed, R. Ali, and M.A. Baig. CF-LIBS based elemental analysis of Saussurea simpsoniana medicinal plant: a study on roots, seeds, and leaves. *Analytical Sciences* 40(3): 413-427 (2024). https://doi.org/10.1007/s44211-023-00480-9
3. W. Bialek and S. Setayeshgar. Cooperative sensitivity and noise in biochemical signaling. *Physical Review Letters* 100: 258-263 (2008). https://doi.org/10.1103/PhysRevLett.100.258101

b. Books

4. W.R. Luellen (Ed.). Fine-Tuning Your Writing. *Wise Owl Publishing Company, Madison, WI, USA* (2001).
5. U. Alon and D.N. Wegner (Eds.). An Introduction to Systems Biology: Design Principles of Biological Circuits. *Chapman & Hall/CRC, Boca Raton, FL, USA* (2006).

c. Book Chapters

6. M.S. Sarnthein, J.E. Smolen, and J.D. Stanford. Basal sauropodomorpha: historical and recent phylogenetic developments. In: The Northern North Atlantic: A Changing Environment. P.R. Schafer and W. Schluter (Eds.). *Springer, Berlin, Germany* pp. 365-410 (2000).
7. S. Brown and L.A. Boxer. Functions of Europhiles. In: Hematology, (4th Edition). W.J. Williams, E. Butler, and M.A. Litchman (Eds.). *McGraw Hill, New York, USA* pp. 103-110 (1991).

d. Reports

8. M.D. Sobsey and F.K. Pfaender. Evaluation of the H_2S method for Detection of Fecal Contamination of Drinking Water. Report No.-WHO/SDE/WSH/02.08. *Water Sanitation and Health Programme, WHO, Geneva, Switzerland* (2002).

e. Online References

These should specify the full URL for reference, please check again to confirm that the work you are

citing is still accessible:

9. UNESCO. Global Education Monitoring Report 2024/5: Leadership in education−Lead for learning. *United Nations Educational, Scientific and Cultural Organization, Paris, France* (2024). https://digitallibrary.un.org/record/4066661?ln=en&v=pdf

10. L.M. Highland and P. Bobrowsky. The landslide handbook−A guide to understanding landslides. Circular 1325. *US Geological Survey, Reston, Virginia* (2008). https://pubs.usgs.gov/circ/1325/pdf/C1325_508.pdf

f. Conference Proceedings

11. M. Khalid, A.B. Majid, F. Mansour, and C.R. Smith. Word Representations with Recursive Neural Networks for Morphology. *27th European Conference on Signal Processing, (2nd - 6th September 2021), Madrid, Spain* (2021).

g. A Degree Thesis

12. M. Afzal. Investigation of structural and magnetic properties of nanometallic Fe-Mn Alloys. Ph.D. Thesis. *Quaid-i-Azam University, Islamabad, Pakistan* (2023).

Tables: Insert all tables as editable text, not as images. Number tables consecutively following their appearance in the text. A concise but self-explanatory heading must be given. Tables should be numbered according to the order of citation (like **Table 1.**, **Table 2.** (font size 10)). *Do not* abbreviate the word "Table" to "Tab.". Round off data to the nearest three significant digits. Provide essential explanatory footnotes, with superscript letters or symbols keyed to the data. Do not use vertical or horizontal lines, except for separating column heads from the data and at the end of the Table.

Figures: In the main text write Figure, not Fig. Figures may be printed in two sizes: column width of 8.0 cm or page width of 16.5 cm; In the Figure caption, number them as **Fig. 1.**, **Fig. 2.** Captions to Figures must be concise but self-explanatory (font size 10). Laser-printed line drawings are acceptable. Do not use lettering smaller than 9 points or unnecessarily large. Photographs must be of high quality. A scale bar should be provided on all photomicrographs. All Figures should have sufficiently high resolution (minimum 300 dpi) to enhance the readability. Figures as separate files in JPG or TIFF format may be provided.

SUBMISSION CHECKLIST

The following list will be useful during the final checking of an article before submission to the journal.

1. Manuscript in MS Word format
2. Cover Letter
3. Novelty Statement
4. Copyright Form
5. Figures in JPG or TIFF format

In case of any difficulty while submitting your manuscript, please get in touch with:

Editor-in-Chief
Pakistan Academy of Sciences
3-Constitution Avenue,
G-5/2, Islamabad, Pakistan
Email: editor@paspk.org
Tel: +92-51-920 7140
Websites: http://www.paspk.org/proceedings/; http://ppaspk.org/

PROCEEDINGS OF THE
PAKISTAN ACADEMY OF SCIENCES: PART A
Physical and Computational Sciences

CONTENTS

Volume 63, No. 2, June 2026 **Page**

Research Articles

PAKISTAN ACADEMY OF SCIENCES, ISLAMABAD, PAKISTAN

HEC Recognized; Scopus Indexed

Websites: http://www.paspk.org/proceedings/; http://ppaspk.org